Patterned magnetic thin films for ultra high density recording

The research described in this thesis was carried out at the Information Storage Technology Group, MESA Research Institute, University of Twente, P.O. Box 217, 7500 AE Enschede, The Netherlands.

M.A.M. Haast
Patterned magnetic thin films for ultra high density recording
Thesis University of Twente, Enschede, The Netherlands.
ISBN 90-36513456

Acknowledgement
This thesis is the result of research carried out in the project 'Magneto-optical multilayer structures' (TEL.3463), financially supported by the Dutch Technology Foundation (STW).

PATTERNED MAGNETIC THIN FILMS FOR ULTRA HIGH DENSITY RECORDING

PROEFSCHRIFT

ter verkrijging van
de graad van doctor aan de Universiteit Twente,
op gezag van de rector magnificus,
prof.dr. F.A. van Vught,
volgens besluit van het College voor Promoties
in het openbaar te verdedigen
op donderdag 9 september 1999 te 16:45 uur.

door

Marc Antonius Maria Haast

geboren op 12 augustus 1971
te Rijsbergen

Dit proefschrift is goedgekeurd door

de promotor: prof.dr. Th.J.A. Popma
de assistent-promotor: dr. J.C. Lodder

Table of Contents

Chapter 1: Present and future data storage technologies 1

1.1 State-of-the-art disk-storage technologies 1
1.2 Outlook for disk-storage technologies 3
1.3 Future storage technologies 3
1.3.1 Probe recording 4
1.3.2 Patterned media 4
1.4 Outline of this thesis 5

Chapter 2: Relevant magnetic phenomena in patterned media 7

2.1 Requirements for patterned media 7
2.2 Uniaxial magnetic anisotropy 8
2.3 Demagnetized domain state 9
2.3.1 Analytical calculation of critical dot size 10
2.3.2 Micromagnetic calculation of critical dot size 12
2.4 Magnetization reversal 14
2.4.1 Analytical calculations of magnetization reversal 14
2.4.2 Micromagnetical calculations of magnetization reversal 16
2.5 Magnetostatic interactions 17
2.6 Thermal stability 18
2.7 Summary 19

Chapter 3: Submicron patterning by laser interference lithography ... 23

3.1 Introduction to submicron patterning techniques 23
3.1.1 Nano-patterning with a pre-patterned mask 23
3.1.2 Nano-patterning without a mask 24
3.1.3 Nano-patterning without resist layers 25
3.2 Different approaches to laser interference lithography 26
3.3 Designed patterning process 27
3.4 Interference pattern and resist structures 30
3.4.1 The role of substrate reflectivity 30
3.4.2 Antireflective coatings 34
3.5 Limits of laser interference lithography 37
3.6 Summary and outlook 42

Chapter 4: Preparation and characterization of $Co_{50}Ni_{50}$/Pt multilayers 47

4.1 Introduction 47
4.2 Deposition by magnetron sputtering 48
4.2.1 Technology 48
4.2.2 Thin film growth by sputtering 48
4.2.3 Deposition pressure and magnetic anisotropy 50
4.2.4 Experiments 50
4.3 Texture in sputtered $Co_{50}Ni_{50}$ and Pt thin films 51
4.3.1 XRD analysis of Pt thin films 52
4.3.2 XRD analysis of $Co_{50}Ni_{50}$ thin films 55
4.4 Texture in sputtered $Co_{50}Ni_{50}$/Pt multilayers 56
4.4.1 XRD analysis of $Co_{50}Ni_{50}$/Pt multilayers 56
4.4.2 Texture at different deposition conditions 59
4.5 Magnetic anisotropy and layer geometry 62
4.6 Magnetic anisotropy and deposition pressure 65
4.7 $Co_{50}Ni_{50}$/Pt multilayer for application as patterned medium 69
4.7.1 Selection of deposition conditions 69
4.7.2 Magnetization reversal in the optimized $Co_{50}Ni_{50}$/Pt multilayer 69
4.8 Conclusions 73

Chapter 5: Magnetization reversal in patterned $Co_{50}Ni_{50}$/Pt multilayers 77

5.1 Introduction 77
5.2 Patterning process and stability of $Co_{50}Ni_{50}$/Pt multilayer 78
5.2.1 Preparation of micron-sized dots 78
5.2.2 Stability and reproducibility of $Co_{50}Ni_{50}$/Pt multilayer 78
5.3 Magnetization reversal dominated by 'defects' 80
5.3.1 Hysteresis in micron-sized dots 80
5.3.2 Origin and density of the defects 83
5.3.3 Relation between defect and microstructure 86
5.3.4 Summary 88
5.4 Magnetization reversal in 'defect-free' multi and single domain dots 88
5.4.1 Prepared submicron sized dot samples 89
5.4.2 Hysteresis and initial magnetization 90
5.4.3 Rotational hysteresis loss of single and multi domain dots 93
5.4.4 Origin of observed switching field distribution for multidomain dots 94
5.4.5 Activation volume and thermal stability of single domain dots 97
5.5 Conclusions 98

Chapter 6: Discussion, conclusions and recommendations 101

6.1 $Co_{50}Ni_{50}$/Pt multilayer dots: experiments vs. theory 101
6.2 An outlook on patterned medium recording 103
6.2.1 Patterning technology 103
6.2.2 Magnetic material 104

Summary 107

Samenvatting 111

Acknowledgements 115

About the author 117

List of publications 119

Chapter 1

Present and future data storage technologies

The goal of this introductory chapter is to sketch the scope of this thesis by giving a short overview and outlook of the present high-density data storage technologies. Moreover some promising new concepts will be discussed. Finally, the outline of this thesis will be given.

The areal density of data storage devices keeps on increasing at an incredible pace. A few numbers make this very clear. While in 1980 a hard disk could store only a few megabytes, current state-of-the-art hard disks have room for 10-20 gigabytes. Moreover, at present the annual growth rate in bit density is 60-100%. Similar trends apply for low-cost removable-disk technologies. While the 3.5" floppy disk developed in the ´80s has a capacity of 1.44 megabytes, the newest magneto-optical (MO) and optical (DVD-RAM) disks contain up to 6 gigabytes of information. The principles and developments of these currently established storage technologies will now first be discussed.

1.1 State-of-the-art disk-storage technologies

Ever since the introduction of the (personal) computer, hard disk recording has been based on a spinning magnetic disk with a longitudinal medium and an inductive write head. Figure 1.1 shows the evolution of the areal bit density in hard disks developed by IBM, the technology leader of the hard disk industry. The realised progress has been achieved by improvements in system design and application of better magnetic materials for increased media and read/write-head performance. Two examples of the latter category are the introduction of thin film media in the ´80s and (giant-)magnetoresistive read sensors in the ´90s. In spring '99 the first lab demonstrations at 20 Gbits/in^2 have been announced [1.2,3].
Magneto-optic disk technology (MOD) has acquired a substantial share of the market for low-cost rewritable data storage. The big advantage of the MOD over (magnetic) floppy-disk technology is that data is stored magnetically, but is read and written optically via the polar Kerr effect and local heating of the magnetic layer respectively. Therefore, it is a non-contact technology and still provides a nearly unlimited rewritability. Figure 1.2 shows the evolution of storage capacity of Sony MO disks.

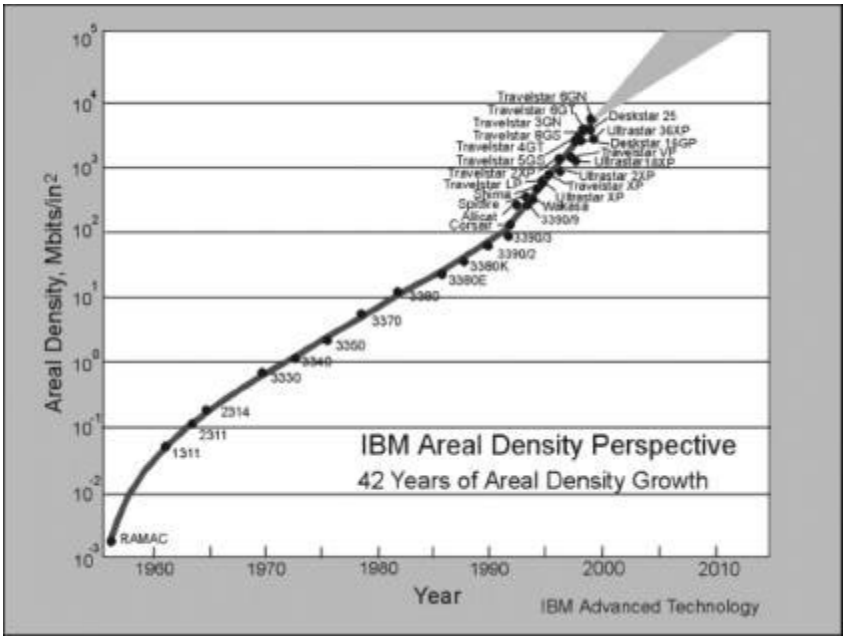

Figure 1.1: *Evolution of the areal density in IBM hard disks [1.1].*

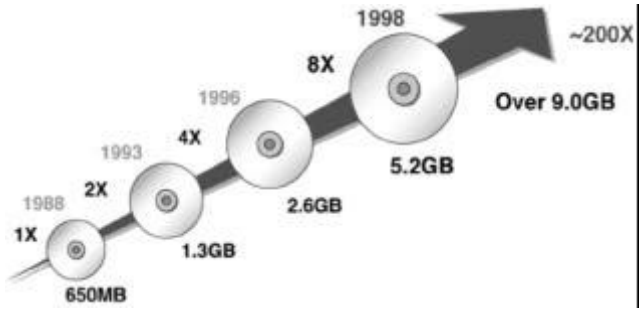

Figure 1.2: *Evolution of storage capacity in Sony magneto-optic disks [1.4].*

The first generation 5.25" MO disks, introduced in 1988, had a capacity of 650 Mbytes. Nowadays, the state-of-the-art commercialized (and standardized!) 5.25" MO disks have a capacity of 5.2 Gbytes. Enabling technologies for this progress are a.o. the reduction of laser wavelength from 830 nm to 680 nm and encoding with Partial-Response-Maximum-Likelyhood [1.5]. Morever, one of the former major drawbacks of MO technology, i.e. the lack of direct overwrite, has been overcome by the introduction of the Laser-Intensity-Modulation-Direct-Over-Write technique. At present 2.6 Gbytes 5.25" direct-overwrite-disks are available [1.6].

Competing with MO disk technology is the rewritable Digital Versatile Disk based on a phase change recording medium (DVD-RAM). This technology is a pure optical recording technique. Depending on the cooling rate of the laser beam crystalline or amorphous marks with a considerable difference in reflectivity are written in the medium. Recently, the first generation DVD-RAM was launched into the market with a 5.2 Gbyte 120 mm disk [1.6].

1.2 Outlook for disk-storage technologies

At present, the bit density in magnetic hard disks is approximately one order of magnitude larger than the bit density in the (removable) MO and DVD-RAM technology. However, with respect to areal bit density it is believed that MO recording has the potential to compete with (magnetic) hard disk recording [1.7]. Recently developed techniques as laser pumped magnetic field modulation and magnetic amplifying magneto-optic system (MAMMOS), together with the introduction of the blue laser diode and solid immersion lens, pave the path for bit densities of 100 Gbit/in^2. In fact, MO technology may be needed to allow (magnetic) hard disk recording to grow to and beyond 100 Gbit/in^2 [1.8]. The main issue in hard disk recording is the thermal instability of magnetic grains, which is expected to start playing a significant role at a bit density of 40 Gbit/in^2. High-anisotropy media and/or perpendicular recording may have to be introduced to allow a further increase. It is very likely that recording on such media should be thermally assisted. Therefore, in the end MO and hard disk technology may merge into the ultimate magnetic disk-storage device.
DVD-RAM is expected to develop at the same pace as MOD in the coming years [1.9]. However, the inferior switching speed of phase change media is presently recognized as a barrier for competitiveness of DVD-RAM at extremely high storage densities. Moreover, a technique as MAMMOS, which allows MO readout below the resolution of the laser spot, is not yet available for phase change recording.

1.3 Future storage technologies

As pointed out in the previous section, magnetic disk recording will carry the bit density of data storage at least over 100 Gbit/in^2. However, for a further progress towards several hundreds of Gbit/in^2 or even up to 1 Tbit/in^2 it has to be expected that new recording concepts are required. At present, the most promising candidate-technologies are probe recording [1.10-14] and/or recording based on patterned (magnetic) media [1.8,15,16].

1.3.1 Probe recording

Extremely high bit densities over 100 Gbit/in^2 will require extraordinary high data rates and tracking at dimensions below 100 nm. It may be doubted that this can be achieved with a spinning disk and flying recording head. Nanometer sized probes mounted on cantilevers, as used in scanning probe microscopy, may be much more suitable for this task. However, the data rate of one single probe is relatively low and therefore the feasibility of systems based on 2D arrays of hundreds or thousands of micromachined probes is under investigation [1.17]. In this concept the spinning disk would be replaced by a linearly scanning system. A schematic view of such a data storage device, or Scanning Probe Array Memory (μSPAM), is shown in Figure 1.3. It should be mentioned that the μSPAM not only is a candidate as a successor to the present hard disk but also may lead to miniaturized low cost and low power storage devices for hand-held computers [1.18].

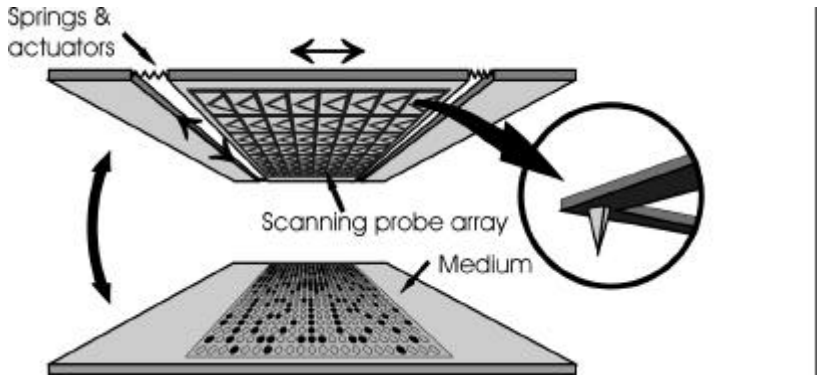

Figure 1.3: *Schematic view of a micro scanning probe array memory (μSPAM) [1.17].*

1.3.2 Patterned media

For magnetic recording the ultimate medium is a regular matrix of single domain dots with an uniaxial anisotropy [1.8,16]. In such a patterned medium a bit is represented by only one dot. With this configuration a storage density larger than 1 Tbit/in^2 can be achieved without suffering from thermal instabilities. On the other hand, perpendicular (magneto-optic) media dominated by domain wall motion have different limits for thermal stability than present hard disk media. Recently, the long term thermal stability of 20 nm domains in Co/Pt multilayers was claimed [1.19]. This would correspond to an areal density of 400 Gbit/in^2 and illustrates that the limits of continuous magnetic media still need to be explored. Therefore, the point where patterned media would be required from a point of view of thermal instabilities is unclear at this stage. Nevertheless, a patterned medium has additional

advantages. The discrete nature of the patterned medium facilitates tracking at extremely high bit density and the single domain state of all dots puts weaker requirements on the writing process itself [1.8,16]. On the other hand, the design of a proper scheme for synchronization of write pulses is a major challenge [1.15].

1.4 Outline of this thesis

During the period of the project resulting in this thesis, its scope evolved from studies on an alternative magneto-optic recording medium for increased sensitivity at the blue laser wavelength, i.e. $Co_{50}Ni_{50}$/Pt multilayers, towards an exploratory study on a patterned medium based on the same material. Therefore, this thesis encompasses a wide variety of subjects. Chapters are devoted to technology issues encountered in submicron patterning (chapter 3), the material science of $Co_{50}Ni_{50}$/Pt multilayers (chapter 4), and the analysis of the magnetic properties of patterned $Co_{50}Ni_{50}$/Pt multilayers (chapter 5). However, firstly, in chapter 2 the magnetic phenomena relevant for the design and analysis of a patterned medium will be discussed.

References

[1.1] E. Grochowski, IBM corporation, www.storage.ibm.com.

[1.2] IBM announcement at Intermag '99.

[1.3] Fujitsu announcement at Intermag '99.

[1.4] Sony corporation, www.sony.com.

[1.5] Optical Storage Technology Association, www2.osta.org.

[1.6] see for instance: Maxell corporation, www.maxell.com.

[1.7] H. Awano, and N. Ohta, *'Magnetooptical recording technology toward 100 Gb/in^2'*, IEEE J. Sel. Top. Quant. El. **4** (1998) 815-820.

[1.8] D.E. Speliotis, *'Magnetic recording beyond the first 100 years'*, J. Magn. Magn. Mat. **193** (1999) 29-35.

[1.9] H.J. Borg, and R. van Woudenberg, *'Trends in optical recording'*, J. Magn. Magn. Mat. **193** (1999) 519-525.

[1.10] E. Betzig, J.K. Trautman, R. Wolfe, E.M. Gyorgy, P.L. Finn, M.H. Kryder, and C.H. Chang, *'Near-field magneto-optics and high density data storage'*, Appl. Phys. Lett. **61** (1992) 142-144.

[1.11] S. Hosaka, H. Koyanagi, A. Kikukawa, M. Miyamoto, K. Nakamura, and K. Etoh, *'Force modulation atomic force microscopy recording for ultrahigh density recording'*, J. Vac. Sci. Technol. B **15** (1997) 788-792.

[1.12] Y. Martin, S. Rishton, and H.K. Wickramasinghe, *'Optical data storage read out at 256 Gbits/in^2'*, Appl. Phys. Lett. **71** (1997) 1-3.

[1.13] D. Saluel, J. Daval, B. Béchevet, C. Germain, and B. Valon, *'Ultra high density data storage on phase change materials with electrical micro-tips'*, J. Magn. Magn. Mat. **193** (1999) 488-491.

[1.14] G. Binnig, M. Despont, U. Drechsler, W. Häberle, M. Lutwyche, P. Vettiger, H.J. Mamin, B.W. Chui, and T.W. Kenny, *'Ultrahigh-density atomic force microscopy data storage with erase capability'*, Appl. Phys. Lett. **74** (1999) 1329-1331.

[1.15] R.L. White, R.M.H. New, and R.F.W. Pease, *'Patterned media: a vialbe route to 50 Gbit/in^2 and up for magnetic recording'*, IEEE. Trans. Magn. **33** (1997) 990-995.

[1.16] S.Y. Chou, *'Patterned magnetic nanostructures and quantized magnetic disks'*, Proc. IEEE **85** (1997) 652-671.

[1.17] M. Lutwyche, C. Andreoli, G. Binnig, J. Brugger, U. Drechsler, W. Häberle, H. Rohrer, H. Rothuizen, P. Vettiger, G. Yaralioglu, and C. Quate, *'5 x 5 2D AFM cantilever arrays a first step towards a Terabit storage device'*, Sens. Act. **73** (1999) 89-94.

[1.18] L. Abelmann, University of Twente, www.utwente.nl/tdm/istg.

[1.19] X. Chen, and M.H. Kryder, *'Thermal stability of Co/Pt multilayers'*, J. Appl. Phys. **85** (1999) 5006-5008.

Chapter 2

Relevant magnetic phenomena in patterned media

In this chapter the magnetic requirements for a patterned storage medium will be given. The relevant magnetic properties as magnetic anisotropy, equilibrium domain states, magnetization reversal and thermal stability will be discussed.

2.1 Requirements for patterned media

Present hard disk media consist of magnetic polycrystalline grains with nanodimensions [2.1]. The exchange coupling between these grains is considerably reduced and consequently they behave more-or-less as single domain particles. Due to effects of the demagnetization, grain size distribution, quasi-random orientation of anisotropy, thermal instabilities etc. a large number of grains is needed to build a bit with a sufficient signal to noise ratio. Optimisation of these effects is therefore the way to improve present media.
The principle of patterned media has already been proposed in the '60s to overcome problems associated with head positioning on the tracks [2.2]. The magnetic material for these media was thought not to be different from that of the continuous (thin film) media. Recently, it was proposed that patterned medium recording with a '1 dot = 1 bit' principle would give additional advantages if the dots would be single domain [2.3,4]. Then the constraints on the writing and reading process itself are greatly reduced. Due to the single domain nature of every dot, the writing of such a bit is an all-or-nothing event and the head does not have to be positioned exactly above the bit. Besides, the signal to noise ratio of the read-back signal is much better due to the absence of media and transition noise. Therefore, the superparamagnetic bit density limit of this type of medium is much higher than that of present thin film media.
For the design of a prototype patterned medium for '1 dot = 1 bit' recording several requirements can be given:

- The dots should be in a regular 2D matrix.
- A dot should behave as one entity, i.e. it should be single domain. In this context 'single domain' means that domain wall formation in a dot is impossible. Therefore the magnetic material should have a strong intergranular exchange coupling (quasi-single-crystalline) or, in the case of amorphous materials, have no structural inhomogeneities as (nanoscale) voids.

- The switching field should be sufficiently large and only two stable remanent states (up-or-down or left-or-right) can be allowed. This means that all dots should have a large uniaxial magnetic anisotropy with the same orientation.
- The number of 'bad bits' due to missing dots or inhomogeneities in the magnetic material should be small.
- The dots should have a low switching field distribution to avoid unwanted writing of neighbouring dots. This implies that both the intrinsic switching field distribution and the dipolar interaction should be minimized.
- The magnetization of the dots should be thermally stable.

Besides, the interest from the point of view of application, media with the above mentioned properties are exceptionally suitable for more fundamental studies. In particular, the mechanisms of magnetization reversal and the role of the activation volume are still not well understood for experimental single domain particles. The main problem is the availability of samples of particles with a low distribution of particle size, narrow distribution of anisotropy orientation and minimal magnetostatic interactions. All these problems are not present in an above described patterned medium.
In the following sections, several issues important for studies on single domain particles/dots will be discussed.

2.2 Uniaxial magnetic anisotropy

For the realisation of uniaxial magnetic anisotropy several different types of materials can be used. The origin of their magnetic anisotropy can be in their microstructure (crystal or structural anisotropy), induced by the geometry of the dot or particle (shape anisotropy) or due to a layered structure (interface anisotropy):

- *Crystal anisotropy*

Classical examples of materials with a (large) crystal anisotropy are hcp-oriented cobalt and bariumferrite. Both materials can be deposited as (ultra)thin films with a highly oriented structure and an anisotropy constant approaching the bulk values [2.5,6]. Materials with an extremely high crystal anisotropy are Fe or Co based alloys with $L1_0$ phase, such as FePt, CoPt and FePd. Thin films of these materials generally have a reduced, but still very high, anisotropy constant [2.7-9].

- *Structural anisotropy*

A rather special class of materials are the amorphous alloys of rare-earth and transition-metals, which are presently applied as magneto-optic recording media [2.10]. The origin of the perpendicular magnetic anisotropy in these materials still raises a lot of questions. Nevertheless, an extensive structural study exists which

shows that the magnetic anisotropy in these materials may be explained by a growth-induced structural anisotropy on the atomic scale [2.11].

- *Shape anisotropy*

Shape anisotropy is present when a magnetic particle has a non-spherical shape. This anisotropy will be uniaxial in the case of pilars or needles.

- *Interface anisotropy*

Interface anisotropy is assumed to be the cause of the large perpendicular anisotropy observed in Co-based multilayers with thin (< 10 Å) Co layers [2.12]. In these multilayers the total effective magnetic anisotropy, K_{eff}, is phenomenologically described by [2.13]:

$$K_{eff} \cdot t = 2 \cdot K_i + K_v \cdot t \tag{2.1}$$

where K_i and K_v are the interface resp. volume anisotropy and t is the magnetic layer thickness. The volume anisotropy can consist of crystal, shape and magnetoelastic contributions. The former two have been discussed above. The latter is caused by an inhomogeneous strain in the crystal lattice of the magnetic layer. Especially, in the case of multilayers of materials with a large difference in lattice spacing the magnetoelastic anisotropy may be considerable [2.14].

In Table 2.1 an overview is given of the saturation magnetization and uniaxial anisotropy constant of the materials mentioned above. The switching field that can be expected for single domain dots patterned from these materials is strongly determined by these properties. The upper limit of the switching field (corrected for demagnetization) is given by the nucleation field of a particle, which has a magnetization reversal by coherent rotation (Stoner-Wohlfarth particle). This value is called the anisotropy field and is given by:

$$H_{K,u} \equiv \frac{2K_u}{\mu_0 M_s} \tag{2.2}$$

For all materials the calculated value, also shown in Table 2.1, seems more than sufficient for storage purposes.

2.3 Demagnetized domain state

A magnetic particle is single domain if the energy of a two-domain state is larger than that of a single-domain state. For a cylindrical dot, as shown in Figure 2.1, this transition will occur at a critical diameter d_{crit}. In this section an expression is given for d_{crit}. Moreover, the absolute value will be calculated for the $Co_{50}Ni_{50}$/Pt multilayers.

Table 2.1: *Bulk and experimental values of saturation magnetization, uniaxial anisotropy constant and anisotropy field for some magnetic materials.*

Material	M_s (kA/m)	K_u (kJ/m^3)	$H_{K,u}$ (kA/m)
Co (hcp)	1420	450	500
Co (fcc)	1420	(640) [1]	(700) [1]
Ni	480	(75) [1]	(240) [1]
Fe	1700	(920) [1]	(860) [1]
$BaFe_{12}O_{19}$	350	300	1300
FePt ($L1_0$ phase) [2]	1100	4000	5700
TbFeCo [3]	100	100	1600
$Co_{50}Ni_{50}$/Pt (multilayer) [4]	500	480	1500

[1] For shape anisotropy of quasi-infinitely elongated pilars (aspect ratio >> 1).
[2] Value from [2.8]. For bulk CoPt and FePt, K_u = 2.8 resp. 7.0 MJ/m^3. Thin film CoPt and FePt with $L1_0$ phase usually have a considerably lower anisotropy constant.
[3] Value from [2.10]. TbFeCo is a ferrimagnet. Its magnetization strongly depends on the compensation temperature.
[4] This work (see Chapter 4). Due to the modulation of magnetic and non-magnetic layers its shape anisotropy is proportional to $\overline{M_s^2}$ instead of $\overline{M_s}^2$ [2.15].

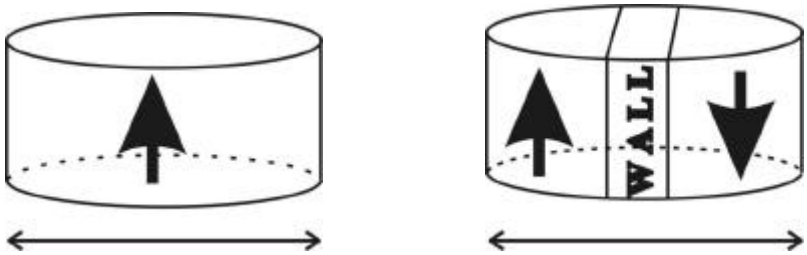

d < d crit **d > d crit**

Figure 2.1: *Schematic view of single and multi domain cylinders.*

2.3.1 Analytical calculation of critical dot size

In order to estimate the critical dot size, two magnetic energies are considered: the magnetostatic and the domain wall energy. For a uniformly magnetized ellipsoid, the magnetostatic energy density, in S.I. units, is given by:

$$e_{magnetostatic} = \frac{1}{2}\mu_0(N_x M_x^2 + N_y M_y^2 + N_z M_z^2) \qquad (2.3)$$

The energy density of a Bloch wall where magnetostatic contributions can be neglected, is given by [2.16]:

$$e_{wall} = 4\sqrt{AK_u} \qquad (2.4)$$

Assuming a uniform magnetization along the axis of the cylinder, i.e. z-direction, the total energy of the single domain state can be approximated by:

$$E_{single\,domain} \approx \varepsilon_{magnetostatic} \cdot V_{dot} = \pi/8\, \mu_0\, d^2 h\, N_z(h,d) M_s^2 \qquad (2.5)$$

where, N_z(h,d) is the (average) demagnetizing factor of the cylinder, which depends on the cylinder height h and diameter d. The most difficult quantity to estimate in this approximation is the magnetostatic energy of the two domain state. For simplicity, it is assumed to be halved compared to the single domain state. Then the total energy of the two domain state becomes:

$$E_{two\,domain} \approx 1/2\, \varepsilon_{magnetostatic} \cdot V_{dot} + \varepsilon_{wall} \cdot A_{wall}$$
$$= \pi/16\, \mu_0\, d^2 h\, N_z\,(h,d) M_s^2 + 4 d\, h \sqrt{A K_u} \qquad (2.6)$$

The critical dot diameter d_{crit} for the transition from a single to a two domain state can be found by equalizing Equations (2.5) and (2.6) and solving for d:

$$d_{crit} \approx 32/\pi \, \frac{Q \cdot \delta}{N_z(h, d_{crit})} \qquad (2.7)$$

with

$$Q \equiv \frac{K_u}{1/2\, \mu_0 M_s^2} \qquad (2.8)$$

and

$$\delta \equiv \sqrt{\frac{A}{K_u}} \qquad (2.9)$$

The latter is used in micromagnetics to represent the wall width and actually is the Landau and Lifschitz wall width [2.16].

The inhomogeneous nature of a $Co_{50}Ni_{50}$/Pt multilayer (e.g. {$Co_{50}Ni_{50}$ (6 Å) /Pt (6 Å)} x 26, as used in Chapter 5) highly complicates the application of Equation (2.7). As a first approach the multilayer dot can be modelled as homogeneous and consequently the measured magnetic properties averaged over the volume are used to estimate the single- to two-domain transition. K_u and A are averaged in such a way that the total wall energy and wall thickness are unchanged. The averaged magnetization is calculated from the average shape anisotropy, given by the difference in measured average total anisotropy – average uniaxial anisotropy. In this way also the total magnetostatic energy is unchanged.
With the averaged values given in Table 2.2, for $Co_{50}Ni_{50}$/Pt multilayers it is found that Q = 1.5 and δ = 2.5 nm. Then the critical dot diameter becomes:

$$d_{crit} \approx \frac{38.2}{N_z(h, d_{crit})} \qquad \text{[nm]} \qquad (2.10)$$

Table 2.2: *Magnetic properties of $Co_{50}Ni_{50}$ as measured in the {$Co_{50}Ni_{50}$ (6 Å) /Pt (6 Å)} x 26 multilayers and as averaged for the homogeneous dot.*

Magnetic property	**For $Co_{50}Ni_{50}$ in multilayer**	**For '$Co_{50}Ni_{50}$' in averaged dot**
Uniaxial anisotropy K_u (kJ/m^3)	960 [1]	480
Exchange constant A (J/m)	$6 \cdot 10^{-12}$ [2]	$3 \cdot 10^{-12}$
Magnetization M_s (kA/m)	1000 [1]	713

[1] As measured, see Chapter 4.
[2] Estimated from a comparison of the Curie temperature of $Co_{50}Ni_{50}$/Pt multilayers [2.17] and Co/Pt multilayers [2.18].

Unfortunately, no simple analytical expression for N_z of (flat) cylinders exists. In the limits of h « d and h ≈ d N_z is 1 respectively 1/3. Then d_{crit} is 38 respectively 108 nm. For intermediate values of h, d_{crit} should be calculated using tabulated values of N_z (see e.g. [2.19]). Then with an iterative procedure, it can be calculated that for $Co_{50}Ni_{50}$/Pt multilayer dots with h increasing from 6 to 12δ (i.e. from 15 to 30 nm) d_{crit} increases from 60 to 73 nm. The dependence of the critical dot diameter on the dot height seems not to be very strong in this height range.

2.3.2 Micromagnetic calculation of critical dot size

In the foregoing analytical treatment the magnetostatic energy of a uniformly magnetized state and the domain-wall energy of a Bloch wall have been used. In the cylindrical dots under study, the remanent state can never be uniformly magnetized and the domain wall will not be a true Bloch wall because also magnetostatic effects will play a role. Moreover, the estimation of the magnetostatic energy of a two-domain state seems rather arbitrary. In order to obtain a more precise value of the critical dot diameter, a numerical approach has been done. The 3D micromagnetic-simulation package used for this purpose can consider exchange, strayfield, anisotropy and external field contributions [2.20]. The non-uniform magnetization and wall geometry are found as equilibrium configurations by using energy minimization techniques. By comparing energies and investigating configuration stability as function of cell size, a set of possible equilibrium states can be found. Following this procedure, the energy of a single- and two-domain state of a $Co_{50}Ni_{50}$/Pt multilayer dot has been calculated as function of dot diameter. The result is shown in Figure 2.2. The critical dot diameter is approximately 71 nm. Surpisingly, this is very close to value found from the analytical approximations.

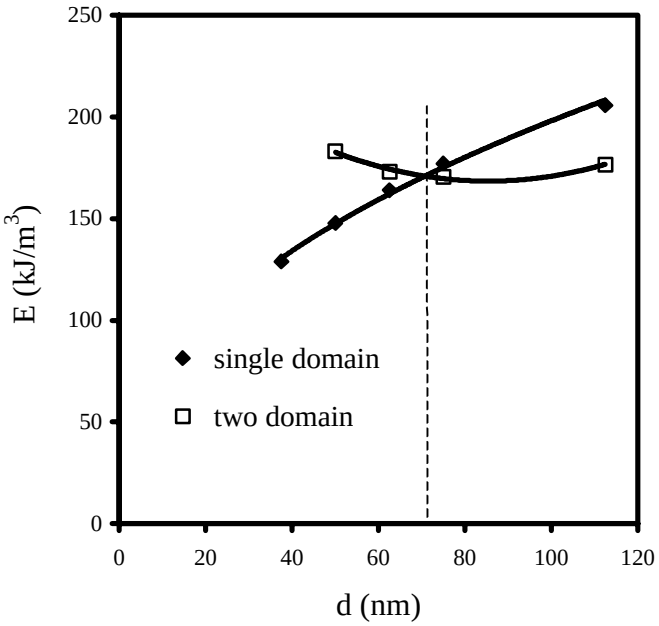

Figure 2.2: *Energy vs. dot diameter for single- and two-domain state of a $Co_{50}Ni_{50}$/Pt multilayer dot with h=30 nm (magnetic properties in Table 2.2).*

Concluding, both the analytical and the numerical calculations indicate that for $Co_{50}Ni_{50}$/Pt multilayer dots with a diameter larger than approximately 70 nm the two-domain state has lower energy than the single-domain state. Both states are stable in the whole range of diameters studied and are apparently 'separated' by an energy barrier. This means that still in dots with a diameter smaller than 70 nm a two-domain state can be found and that dots with a diameter much larger than 70 nm may appear as single domain. However, since this is the result of a numerical experiment, conclusions should be drawn with care. As the starting configuration of the numerical evaluation of the equilibrium state, a two domain state is simply generated as a dot with an up and down domain of the same size. In reality, once saturated, the dot has to reach the two domain state by nucleation of a domain wall. The question is whether this is possible, even when the final two domain state would have lower energy than the single domain state. For the experimentalist behind the magnetometer, the history of the magnetic field exposed to the dot will determine the state in which it will be found.
Finally, this section should be ended with a critical remark. In all calculations the highly inhomogeneous $Co_{50}Ni_{50}$/Pt multilayers have been modelled as homogeneous material with averaged properties. Though the averaging was done in a carefully chozen way, the resulting uncertainty in the evaluated critical dot diameter, associated with this approximation, is hard to estimate.

2.4 Magnetization reversal

In section 2.2 the anisotropy field was calculated for several materials. This was mentioned to be an upper limit of the switching field. To be more precise, this limit only applies in the absence of demagnetizing effects (or after correction for this). In this section the magnetization reversal of more practical shapes will be calculated and discussed.

2.4.1 Analytical calculations of magnetization reversal

In theoretical works the nucleation field H_N is defined as the (reverse) field where the magnetic state *starts* to deviate from uniform saturation (see e.g. [2.16]). Since only ellipsoids can exhibit a uniform magnetic state (and besides have a uniform demagnetizing field), the analytical calculations of the nucleation field are limited to this class of particles. Despite of this precondition, it is very instructive to use approximations by ellipsoids to calculate nucleation fields for other shapes. This provides insight in the relation between the nucleation field and the intrinsic material properties as saturation magnetization M_s, uniaxial anisotropy K_u and exchange constant A. It should be emphasized that in principle no estimation is made of the more relevant coercive field H_C, defined as the field where the average magnetization equals zero. Since H_C is by definition always larger (or more negative) than H_N, only a lower limit of H_C is calculated.
For the case of a configuration with the applied field parallel to the easy axis of magnetization, two relevant modes of magnetization reversal exist which are the two analytical solutions of Brown's magnetostatic equations (see the original work by Brown [2.21] or the recent book by Aharoni [2.16]). These have been named coherent rotation and magnetization curling. The former one is valid for any ellipsoid, while the latter one is only valid for an ellipsoid of revolution, either prolate or oblate. Now, the equations of the nucleation field of both modes will be given and used to estimate the nucleation field of cylindrical $Co_{50}Ni_{50}$/Pt multilayer dots.
Under the condition that the easy axis of shape and crystal anisotropy is in the same direction, the nucleation field for coherent rotation is given by [2.16]:

$$H_N = \frac{2K_u}{\mu_0 M_s} - (N_z - N_x)M_s \equiv H_{K,eff} \tag{2.11}$$

, where $H_{K,eff}$ is called the effective anisotropy field. In the case N_z=0 and N_x=0.5, i.e. a long and narrow cylinder, the theoretical upper limit of the nucleation field is found. With the proper expression for (inhomogeneous) multilayers,

$$H_{N,ml} = \frac{2\overline{K_u} - \mu_0(N_z - N_x)\overline{M_s^2}}{\mu_0 \overline{M_s}} \equiv H_{K,eff,ml} \tag{2.12}$$

, this limit equals $H_{N,\,ml}$ = 2000 kA/m for $Co_{50}Ni_{50}$/Pt multilayers (with Table 2.2).
The nucleation field for magnetization curling is given by [2.16]:

$$H_N = \frac{2K_u}{\mu_0 M_s} - N_z M_s + \frac{8q^2 A}{d^2 \mu_0 M_s} \tag{2.13}$$

with:

q = 1.8412 for an infinitely long cylinder
q = 2.0816 for a sphere
q = 2.115 for an infinite plate

and for (inhomogeneous) multilayers,

$$H_N = \frac{2\overline{K_u} - \mu_0 N_z \overline{M_s^2}}{\mu_0 \overline{M_s}} + \frac{8q^2 \overline{A}}{d^2 \mu_0 \overline{M_s}} \tag{2.14}$$

Since nucleation takes place by the mode with the lowest nucleation field, the transition from coherent rotation to magnetization curling is found by equalizing the last term in (2.13) and the term $N_x M_s$ of (2.11):

$$d_{coherent} \leq \frac{2q}{M_s} \sqrt{\frac{2A}{\mu_0 N_x}} \tag{2.15}$$

For (inhomogeneous) multilayers,

$$d_{coherent} \leq 2q \sqrt{\frac{2\overline{A}}{\mu_0 N_x \overline{M_s^2}}} \tag{2.16}$$

For $Co_{50}Ni_{50}$/Pt multilayer dots with h = 30 nm, coherent rotation occurs for diameters < 22 nm. At the transition the calculated nucleation field (Equation (2.12)) equals then approximately the anisotropy field $H_{K,u}$, i.e. 1500 kA/m.

For

$$d >> \frac{2q}{M_s} \sqrt{\frac{2A}{\mu_0}} \tag{2.17}$$

, i.e. when the last term in Equation (2.13) can be neglected, Equation (2.13) can be writen in the usefull form with reduced units:

$$H_N = 1 - \frac{N_z}{Q} \qquad [H_{K,u}] \tag{2.18}$$

with Q as defined in Equation (2.8) and H_N in units of the anisotropy field. For N_z = 1 the lower limit of the nucleation field (thin film limit) is found.

For (inhomogeneous) multilayers,

$$d_{coherent} >> 2q \sqrt{\frac{2\overline{A}}{\mu_0 \overline{M_s^2}}} \tag{2.19}$$

and this limit equals 500 kA/m for $Co_{50}Ni_{50}$/Pt multilayers and is valid for d >> 13 nm (and d>>h).

2.4.2 Micromagnetic calculations of magnetization reversal

According to the foregoing analytical treatment the nucleation field in cylindrical $Co_{50}Ni_{50}$/Pt multilayer dots is estimated to be in the range between 500 and 2000 kA/m. These values are more than sufficient for long-term storage purposes. However, in practice switching fields are usually much smaller than the calculated values of the nucleation field. This fact is well-known as Brown's paradox. Of course, especially for the case of cylindrical multilayer dots, the approximation by homogeneous and uniformly magnetized ellipsoids may be very poor. Other issues are the role of dot shape, edge roughness and local anisotropy variations. In order to investigate the effect of these typically experimental conditions, a study with micromagnetic simulations, as introduced in subsection 2.2.2, has been carried out. For several realistic dot shapes the switching of 'homogeneous' $Co_{50}Ni_{50}$/Pt multilayer dots (magnetic properties in Table 2.2) have been simulated. The initial configuration was the saturated state at zero field. By applying increasing reverse fields the switching field H_{SW} was found. The dot shapes and corresponding switching fields are shown in Table 2.3. Though the extrapolation method may affect the absolute values of the estimated switching field, the observed trend is undisputed.
For all investigated dot shapes the numerically calculated switching field is lower than the theoretical nucleation field for ellipsoids. While for the perfect cylinder the difference is still moderate, for the truncated cones the switching fields are more than 50% lower. This behaviour should be attributed to the increased fanning out of the spins at the edge for the truncated cones [2.22]. It may be expected that some edge roughness may further increase this effect and result in even smaller switching fields.

Table 2.3: *Numerically calculated switching field H_{sw} of $Co_{50}Ni_{50}$/Pt multilayer dots with several different shapes. The parameters used for the micromagnetic simulations are calculated from Table 2.2: Q = 1.5 and d = 2.5 nm. Also the average demagnetizing factor [2.19] and the analytically calculated nucleation field for ellipsoids (Equation (2.18)) are given.*

Dot shape	d_{top} (nm)	d_{bottom} (nm)	h (nm)	$\overline{N_z}$	H_N ($H_{K,u}$)	H_{sw} ($H_{K,u}$)
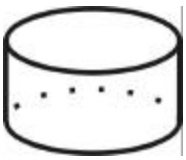	80	80	30	0.54	0.64	0.50 ± 0.05
	40	80	30	0.48	0.68	0.35 ± 0.02
	40	80	20	0.57	0.62	0.23 ± 0.05

2.5 Magnetostatic interactions

The switching field distribution associated with the dipolar interaction between magnetic particles is proportional to the magnetization of the material. This interaction is strongly dependent on inter-particle distance, particle shape and saturation magnetization. Therefore, a simple generalized expression for its magnitude can not be given. Moreover, in the end the allowed switching field distribution will have to be defined by the tolerances of the storage device.
Here, with respect to magnetostatic interactions only a firm statement can be made concerning the stability of the saturated state of a patterned medium. In zero field, the stability of the medium is not dependent on inter-particle distance and saturation magnetisation if the uniaxial anisotropy is larger than the thin film shape anisotropy, i.e. if Q > 1 (Equation 2.8). This means that the highest bit/dot density can be obtained for materials with Q > 1. Table 2.4 shows the Q values of the materials discussed in section 2.2. It can be seen that these materials have a wide variety of Q values. From the point of view of bit density, single-element patterned media are clearly not suitable for storage purposes. Moreover, it will be difficult to

obtain the intrinsic switching field distribution of densely packed single-element pilars.

Table 2.4: *Q values (Equation 2.8) of several materials with uniaxial magnetic anisotropy (with Table 2.1).*

Material	**Q**
Co (hcp)	0.34
Co (fcc)	(0.50) [1]
Ni	(0.50) [1]
Fe	(0.50) [1]
$BaFe_{12}O_{19}$	3.7
FePt ($L1_0$ phase)	5.2
TbFeCo	16
$Co_{50}Ni_{50}$/Pt (multilayer)	1.5

[1] For shape anisotropy of a quasi-infinitely elongated prism or cylinder.

2.6 Thermal stability

At present the problem of thermal instability of written bits is a big issue in conventional magnetic recording and determines the fundamental limit, often called 'the superparamagnetic limit', of the storage density in thin film media [2.23]. The origin of the thermal instability is the competition between the thermal and magnetic energy of a particle. This leads to a relaxation time τ at zero field, which, in its most idealized form and assuming a prefactor of 10^{-10}, is given by [2.16]:

$$t = 10^{-10} e^{\frac{KV}{k_B T}} \tag{2.20}$$

where:
- k_B : Boltzmann's constant
- T : temperature
- K : (uniaxial) magnetic anisotropy
- V : particle volume

For long-term storage purposes thermal relaxation should be prevented for sufficiently long time. Table 2.5 gives the edge of a cubic dot, consisting of materials discussed in section 2.2, for which the relaxation time is 10 years.
Clearly, all calculated values are sufficiently small for patterned medium recording. However, for (most) experimental particles, Equation 2.20 does not apply and the more appropriate expression for the relaxation time is given by [2.24]:

$$t = 10^{-10} \cdot e^{\frac{\frac{1}{2}\mu_0 M_S H_C V_{act}}{k_B T}} \tag{2.21}$$

Table 2.5: *The size of a cubic element at which the thermal relaxation time equals 10 years, for several materials with uniaxial magnetic anisotropy (with Equation (2.20) and Table 2.1).*

Material	**l_{sp} (nm)**
Co (hcp)	7
Co (fcc)	(4) [1]
Ni	(6) [1]
Fe	(3) [1]
$BaFe_{12}O_{19}$	8
FePt ($L1_0$ phase)	4
TbFeCo	12
$Co_{50}Ni_{50}$/Pt (multilayer)	7

[1] For prisms with dimensions l_{sp} x l_{sp} x $10l_{sp}$.

where: M_S : saturation magnetisation
H_C : coercive field
V_{act} : activation volume

The activation volume is associated with the magnetic volume initiating the magnetization reversal and therefore in general deviates from any physical dimension like magnetic particle or dot volume [2.25]. Just as the coercive field, the activation volume needs to be determined experimentally via the following relation [2.26]:

$$V_{act} = \frac{k_B T}{\mu_0 M_S} \cdot \frac{\chi_{irr}}{S} \tag{2.22}$$

where χ_{irr} is the irreversible susceptibility, which equals the derivative of the hysteresis curve if all reversal processes are irreversible; and S is the magnetic viscosity and is determined from the thermally activated switching of magnetization at a certain applied field.

2.7 Summary

In this chapter the requirements for a prototype patterned medium have been given. The magnetic dots should have a strong intergranular exchange coupling, large uniaxial anisotropy and low switching field distribution. Using these guidelines several candidate materials have been proposed: bariumferrite, Co or Fe based alloys with $L1_0$ phase, amorphous rare earth – transition metal alloys and Co based multilayers. All four materials have a large intrinsic uniaxial magnetic anisotropy, which guarantees a sufficiently large switching field and a long-term thermal stability. Moreover, the dots of the patterned medium can be shaped in such a way that magnetostatic interactions are suppressed. In this respect, single-element Co, Ni or Fe patterned media are disadvantageous because they suffer from too large

magnetostatic interactions in a densely packed 2D dot-array and therefore will limit the ultimate bit density. With respect to the amorphous alloys some caution is required, because the origin of their magnetic anisotropy is not undisputed.
In addition to these qualitative considerations, the single- to two-domain transition and the switching field of $Co_{50}Ni_{50}$/Pt multilayer dots have been predicted by analytical and micromagnetic calculations: $d_{crit} \approx 70$ nm and $H_{sw} \geq 500$ kA/m. However, it was shown that the latter is strongly dependent on dot shape and can be considerably smaller.

References

[2.1] J.C. Lodder, *'Magnetic recording hard disk thin film media'*, in *'Handbook of magnetic materials'*, edited by K.H.J. Buschow, Elsevier (1998).

[2.2] L.F. Shew, IEEE Trans. Broad. Tel. Rec. **9** (1963) 56.

[2.3] R.L. White, R.M.H. New, and R.F.W. Pease, *'Patterned media: a viable route to 50 Gbit/in^2 and up for magnetic recording'*, IEEE. Trans. Magn. **33** (1997) 990-995.

[2.4] S.Y. Chou, *'Patterned magnetic nanostructures and quantized magnetic disks'*, Proc. IEEE **85** (1997) 652-671.

[2.5] M. Hehn, S. Padovani, K. Ounadjela, and J.P. Bucher, *'Nanoscale magnetic domain structures in epitaxial cobalt films'*, Phys. Rev. B **54** (1996) 3428-3433.

[2.6] A. Lisfi, J.C. Lodder, P. de Haan, M.A. Smithers, and F.J.G. Roesthuis, *'Barium Ferrite Films grown by laser ablation'*, IEEE Trans. Magn. **34** (1998) 1654-1656.

[2.7] M.R. Visokay, and R. Sinclair, *'Direct formation of ordered CoPt and FePt compound thin films by sputtering'*, Appl. Phys. Lett. **66** (1995) 1692-1694.

[2.8] J.U. Thiele, L. Folks, M.F. Toney, and D.K.Weller, *'Perpendicular magnetic anisotropy and magnetic domain structure in sputtered epitaxial FePt (001) $L1_0$ films'*, J. Appl. Phys. **84** (1998) 5686-5692.

[2.9] V. Gehanno, A. Marty, B. Gilles, and Y. Samson, *'Magnetic domains in epitaxial ordered FePd(001) thin films with perpendicular magnetic anisotropy'*, Phys. Rev. B **55** (1997) 12552-12555.

[2.10] M. Mansuripur, *'The physical principles of magneto-optical recording'*, Cambridge University Press (1995).

[2.11] V.G. Harris, W.T. Elam, and N.C. Koon, *'Structural origins of magnetic anisotropy in amorphous non-s-state rare earth – transition metal films'*, in *'High density digital recording'*, edited by K.H.J. Buschow, G.J. Long, and F. Grandjean, Kluwer Academic Publishers (1993) 483-517.

[2.12] M.T. Johnson, R. Jungblut, P.J. Kelly, and F.J.A. den Broeder, *'Perpendicular magnetic anisotropy of multilayers: recent insights'*, J. Magn. Magn. Mat. **148** (1995) 118-124.

[2.13] H.J.G. Draaisma, F.J.A. den Broeder, and W.J.M. de Jonge, *'Magnetic interface anisotropy in Pd/Co and Pd/Fe multilayers'*, J. Magn. Magn. Mat. **66** (1987) 351-355.

[2.14] The magnetoelastic anisotropy is given by: $K_{me} = -\frac{3}{2}\lambda\sigma$, where λ is the magnetostriction constant and σ the stress in the magnetic material.

[2.15] A.A. Kusov, S.S. Jaswal, and Z.S. Shan, *'Shape anisotropy of magnetic multilayers'*, Phys. Rev. B **46** (1992) 3123-3124.

[2.16] A. Aharoni, *'Introduction to the theory of ferromagnetism'*, Oxford Science Publications (1996).

[2.17] Q. Meng, W.P. van Drent, J.C. Lodder, and Th.J.A. Popma, *'Curie temperature dependence of magnetic properties of CoNi/Pt multilayer films'*, J. Magn. Magn. Mat. **156** (1996) 296-298.

[2.18] W.B. Zeper, F.J.A.M. Greidanus, and P.F. Carcia, *'Evaporated Co/Pt layered structures for magneto-optical recording'*, IEEE Trans. Magn. **25** (1989) 3764-3766.

[2.19] D.X. Chen, and J.A. Brug, *'Demagnetizing factors for cylinders'*, IEEE Trans. Magn. **27** (1991) 3601-3619.

[2.20] K. Ramstöck, J.J.M. Ruigrok, and J.C. Lodder, *'Switching behaviour of small soft-magnetic elements'*, Sens. Act. A: Phys., in press.

[2.21] W.F. Brown, *'Micromagnetics'*, Interscience, New York (1963).

[2.22] W. Rave, K. Ramstöck, and A. Hubert, *'Corners and nucleation in micromagnetics'*, J. Magn. Magn. Mat. **183** (1998) 329-333.

[2.23] D.E. Speliotis, *'Magnetic recording beyond the first 100 years'*, J. Magn. Magn. Mat. **193** (1999) 29-35.

[2.24] J.C. Mallinson, *'The Foundations of Magnetic Recording'*, Academic Press Inc., San Diego (1993).

[2.25] R.W. Chantrell, and J.D. Hannay, *'Micromagnetics, magnetic recording and M-O recording media – thermal instabilities and activation volume (invited)'*, Proceedings of MORIS '99, in press.

[2.26] E.P. Wohlfarth, *'The coefficient of magnetic viscosity'*, J. Phys. F: Met. Phys. **14** (1984) L155-L159.

Chapter 3

Submicron patterning by laser interference lithography

In this chapter firstly an overview of submicron patterning technologies is given. Then the details and principles of laser interference lithography will be described. Problems and possible improvements will be discussed as well.

3.1 Introduction to submicron patterning techniques

For a succesfull application of the concept of patterned media recording the development of a suitable patterning technique is one of the crucial items. The requirement of patterning large areas of regularly spaced uniform dots at nano-dimensions puts strong demands on the patterning technology. Even in the R&D lab such technologies are generally not readily available. Not to speak of manufacturing… However, in this work the goal was not to design a patterning technology for the manufacturing of a patterned disk but to prepare a prototype of a patterned medium and study its relevant magnetic properties. Moreover, the aim was to study magnetic submicron dots in general.
In this section an overview of existing and emerging submicron patterning technologies is given which have the potential for the preparation of sub-100 nm dots and spacings. Some of the discussed technologies are already succesfully applied, other are not yet mature and under development. Three types of technologies will be distinguished. The first two are lithographic techniques based on the patterning of resist layers, either with or without a pre-patterned mask. Only the step of pattern generation is discussed here. In general, this pattern has to be transferred to a magnetic layer by common techniques such as lift-off, etching or electrodeposition. Each of these post-lithography steps is also encountered in section 3.2 where complete processes based on laser interference lithography are discussed. The third type is the family of resist-less patterning techniques which are either single- or two-steps patterning processes.

3.1.1 Nano-patterning with a pre-patterned mask

In state of the art integrated circuits minimum feature sizes are already below 200 nm and these critical dimensions are still decreasing. For the production of these devices optical lithography based on wafer steppers is used. These steppers are

equiped with an excimer laser and demagnify structures on a patterned mask on the substrate wafer. The decrease of the feature size is mainly made possible by the application of lasers with shorter wavelength. At present 248 nm KrF lasers are used in IC production and processes with 193 nm ArF laser are under development [3.1]. However, it is generally realised that for sub-100 nm devices a non-optical lithography needs to be developed [3.2]. Among the candidates are proximity x-ray – [3.3], extreme ultra-violet – [3.4], electron projection – [3.5] and ion projection lithography [3.6]. All these technologies require big and expensive machines and might not be suitable for the production of patterned media. However, for R&D purposes they are very interesting. For instance, Rousseaux *et al.* have succesfully patterned high quality submicron magnetic dots with minimum dot sizes of 200 nm by x-ray lithography [3.7].
Parallel to these developments, still much cheaper optical lithography schemes are being proposed for the realisation of sub-100 nm resolution and certainly worth mentioning here: optical lithography with light-coupling [3.8] or phase [3.9] masks and near-field optical lithography [3.10].
Another true promising and emerging submicron patterning technology is nano-imprint or hot-embossing lithography [3.11-13]. Nanosized holes are physically printed in a thin polymer layer with a mold. With this technology Kong *et al.* have demonstrated the preparation and writing of a patterned medium of 10 Gbit/in^2 [3.14]. Despite of the reported results the technology is still under development and several problems, amongst others the adhesion between mold and substrate, need to be solved [3.15]. A technology related to nano-imprint lithography is microcontact printing with self-assembled monolayer (SAM) resists [3.13,16]. A pattern of SAM can directly be 'deposited' by printing with a stamp and does not even require the large forces needed with nano-imprint. Alternatively, the self-assembling capacity of polymers may be used to form a dot pattern without a stamp [3.17]. However, the limits of the latter technique still need to be explored.

3.1.2 Nano-patterning without a mask

For the preparation of limited numbers of nanosized devices electron beam lithography (EBL) is more or less the standard patterning technology. The principle of the technique is the direct writing of the desired structures in a thin resist layer (PMMA) with a focussed electron beam. The resolution is well below 100 nm. Recently the preparation of metallic dot arrays with 25 nm period was reported [3.18]. This implies that the preparation of a patterned medium with a bit density of 1 Tbit/in^2 is in principle possible. Several groups have indeed succesfully applied EBL for the preparation of magnetic dots for storage applications. The minimum dot sizes are 100 nm [3.19], 50 nm [3.20] and 20 nm [3.21]. However, large areas can not readily be patterned with EBL and macroscopic magnetic characterization is therefore not reported on this type of samples. Alternatively, EBL can be used for

the preparation of masks, which can be used in one of the lithographic technologies described in the previous subsection. The preparation of the mold for the nano-imprint technique is such an example [3.11].
Besides the sequential writing of resist structures with EBL, a true optical maskless lithographic technology exists for the preparation of uniform sub-100 nm lines and dots: i.e laser interference or holographic lithography (LIL). In LIL a resist layer is exposed by an interference pattern generated by two obliquely incident laser beams. After development of the resist, lines are formed. The periodicity p of the lines is determined by the wavelength λ and the angle of incidence Θ of the laser beams:

$$p = \frac{\lambda}{2\sin\Theta} \tag{3.1}$$

Dots can simply be fabricated by a second exposure after rotating the substrate over 90º. The patterned area is determined by the diameter of the two laser beams.
For processes with no need for alignment LIL is relatively simple and cheap and therefore the method of choice. Although this technique is not widely known, LIL is already used for more than twenty years for the preparation of submicron gratings for application in integrated optics [3.22,23]. In recent years the possibility of patterning large areas of dots with LIL has been recognized. Now LIL is attracting great attention for a wide variety of applications, amongst others: field emission displays [3.24-26], patterned magnetic media [3.27-30], antireflection-structures [3.31], photonic crystals [3.32], microfiltration [3.33] and mask-making for nanoimprint - [3.34] and X-Ray lithography [3.35]. Its capability for patterning large areas is clearly demonstrated by the fabrication of 50 x 50 cm^2 areas of submicron dots [3.36] and allows the use of standard magnetic characterization tools on 1x1 cm^2 samples in studies on patterned media [3.37].

3.1.3 Nano-patterning without resist layers

Instead of using resist layers for pattern definition, the desired pattern may also be directly written in the magnetic layer or even be directly deposited. Examples of direct writing are demonstrated by Allenspach *et al.* and Aign *et al.*, who have patterned magnetic layers with a focussed electron beam [3.38] and with a focussed ion beam [3.39]. In both cases the magnetic anisotropy of the magnetic material has locally been modified by electron bombardment respectively ion irradiation. Though these techniques only allow the patterning of small areas, especially the focussed ion beam technology seems very promising for basic studies on patterned media. As Aign *et al.* have shown, minimum dot seperations of only 20 nm can be obtained, which allowed studies of dipolar interactions in patterned media.
The ideal way of the preparation of a patterned medium is the direct deposition of dots. Three such techniques are briefly discussed here: sequential deposition of islands, self-organization and laser-focussed atomic deposition.

Though restricted to small areas, scanning probe microscope and again focussed ion beam technology can deposite submicron islands in a sequential way. An example is the work of Bessho *et al.*, who deposited a variety of nanosized magnetic dots with a commercial atomic force and scanning tunneling microscope [3.40].
Direct deposition of nanosized islands over large areas is attracting much interest for electronic applications of quantum dot arrays. These dots are formed by a process of self-organization during the deposition of multilayers of semiconductors [3.41] and can be used as templates for a patterned medium. Using self-organized $Si_{1-x}Ge_x$ films and shadow deposition of Co Teichert *et al.* have shown the preparation of reasonably regular arrays of 25 x 35 nm^2 Co islands [3.42]. The major drawback of this type of patterning is the complexity of the growth of the self-organised pattern.
Finally, an alternative to self-organisation of semiconductors is the direct deposition with neutral atom lithography. As with laser interference lithography an interference pattern of two laser beams is used for pattern definition. Instead of the use of an intermediate step of the exposure of a resist layer the line or dot pattern is directly deposited by the effect of laser-focussed atom deposition. With this technique Celotta *et al.* have demonstrated the preparation of 80 nm Cr dots [3.43]. Though, at present, this technology works only for a limited number of materials, Cr dots may be used as an etching mask for preparing magnetic dots. An other interesting option is the use of the laser-focussed atoms for the exposure and etching of a self-assembled monolayer resist [3.44] or the growth of a carbonaceous resist [3.45]. Recently, atomic beam holography has been proposed as further expansion of neutral atom lithography [3.46]. A resolution of several nanometers would be possible with this technique.

3.2 Different approaches to laser interference lithography

Because of its simplicity, potential and availability laser interference lithography (LIL) was selected as the technology for the submicron patterning of magnetic thin films in this work. In the MESA Research Institute LIL was originally developed for the fabrication of gratings for devices based on integrated optics [3.47]. Obviously, the work at hand benefited enormously from the knowledge gained for the processing of gratings. The principle of the exposure with the interference pattern is shown in Figure 3.1. In this configuration the interference pattern is formed by a ‘direct-incident’ beam and a ‘mirror-reflected’ beam and is called the ‘mirror’ method. Other research groups use a beam-splitter and two mirrors to make the interference pattern (the ‘two-beam’ method, see for instance [3.28,29,48]). The ‘mirror’ method has the big advantage of simplicity and stability. However, the uniformity and area of the exposed pattern may be better respectively larger in the ‘two-beam’ method.

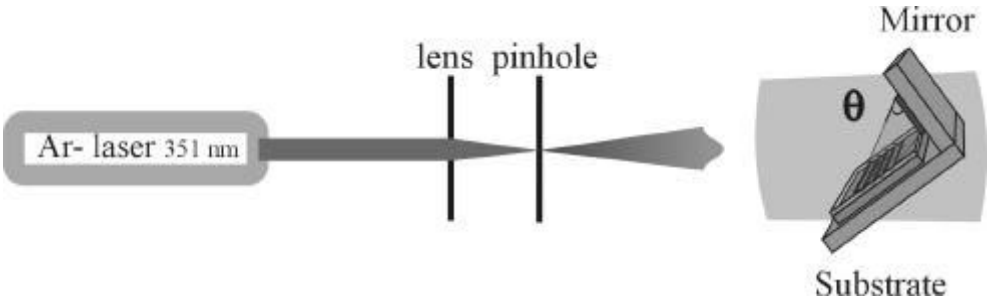

Figure 3.1: *Setup for the pattern exposure in laser interference lithography.*

For the preparation of isolated magnetic dots by LIL, several processing schemes have been developed and are based on the deposition in resist holes by electroplating [3.29] or evaporation-and-lift-off [3.27,28], or, as in this work, on the selective removal of sputter-deposited material by etching [3.30]. For the selection of most suitable processing scheme three criteria are important: i.e. the tailoring of the material properties, the process latitude for pattern definition and the influence of the patterning process on the final magnetic properties of the dots. The first criterium favors deposition by sputtering or perhaps evaporation. As pointed out by Fernandez *et al.* the second criterium favors a process based on resist dots rather than holes [3.48,49]. They have shown that using positive-tone resist the patterning of holes has inferior exposure latitude or requires complex image reversal schemes. Moreover, they state that the limited sensitivity and contrast of negative-tone resist can not solve this problem. The third criterium encompasses effects like the damage induced by resist baking or etching on the dot's magnetic properties and the dot uniformity. From this point of view a post-patterning deposition would be favourable, though not by electroplating. In Table 3.1 a summary of the comparison of the three processing schemes is given.
To conclude this overview of possible processing schemes it should be mentioned that an interesting alternative to etching might be ion irradiation to alternate material properties without physically removing the material. Chappert *et al.* showed that the perpendicular anisotropy could be locally destroyed in Co/Pt multilayers by irradiation of resist lines with He^+ [3.50]. Though the resist lines were not prepared by LIL, this technique may also be incorporated in a process based on LIL.

3.3 Designed patterning process

Since the first objective was the patterning of tailored magnetic films, such as sputtered $Co_{50}Ni_{50}$/Pt multilayers, the third processing scheme in Table 3.1 was selected. Here the separate steps of the designed process are described.

Table 3.1: *A comparison of possible processing schemes for the preparation of magnetic dots with laser interference lithography.*

Process	Advantage	Disadvantage
Resist holes + electroplating	- Requires no etching and allows deposition after processing. - Most simple	- Inferior process latitude for the preparation of resist holes. - Limited to single element pilars and possible bad uniformity of pilar height.
Resist holes + lift-off	- Requires no etching and allows deposition after processing. - The material properties can be well tailored.	- Inferior process latitude for the preparation of resist holes. - Growth in resist holes may result in uncontrolled shapes. - Lift-off processes are not reliable.
Pre-deposited magnetic material + resist dots and etching	- The material properties can be well tailored. - Superior process latitude for the preparation of resist dots	- Material properties may deteriorate during processing.

As a first step, 3” Si (100) wafers are thermally oxidized by a wet oxidation process. Usually 100 to 600 nm thick siliconoxide layers are grown to serve as a diffusion buffer between the silicon and the magnetic thin film, which is subsequently deposited.

Then a thin positive-tone resist layer is spun on top of the magnetic thin film. Standard Shipley 1805 resist is used. The thin resist layers are prepared by diluting the resist with EC solvent (i.e. propylene glycolmonomethyl etheracetate) and spinning at high speed. The final thickness is determined by the ratio of the mixture and the spinning time. Measurements by ellipsometry showed that the resist layer thickness is both highly homogeneous (at the resolution of the laser spot, i.e. < mm) and very reproducible. Over a 3” wafer the thickness varies less than 1% and between different wafers the variation is a few % at most. Here it is interesting to mention that also thin resist layers with similar quality could be prepared on 1x1 cm^2 samples glued on a 3” wafer. Only in an area within 1 mm from the edge the thickness seems to deviate strongly. Apparently also small samples can be patterned with laser interference lithography.

The resist is exposed with an interference pattern using the setup shown in Figure 3.1. By varying the angle of the substrate with the laser beam from 18° to 61° the

periodicity of the interference pattern is decreased from 600 nm to 200 nm. The patterned area is inversely proportional to this angle. At 18° the area is 7x7 mm^2. For angles larger than 45° the area is limited to the size of the mirror, i.e. approximately 25x25 mm^2. In the next section the interference pattern itself will be discussed in more detail.

Development of the exposed resist occurs in a diluted solution of standard developer Microposit 351 (1:7) for 5-15 s. The developed resist pattern is transferred into the magnetic layer with ion beam etching (IBE). IBE is the method of choice for this purpose, because reactive ion etching of magnetic materials is still excluded by the lack of appropriate etching recipes. Since IBE is a purely fysical etching process, the etching rates of various material are approximately equal. This means that the thickness of the magnetic dot is roughly limited to the thickness of the resist dot. Besides, the etching time is most critical. For the purpose of end point detection the resistance can be monitored to calibrate the etching rate. Figure 3.2 shows an example of such measurement.

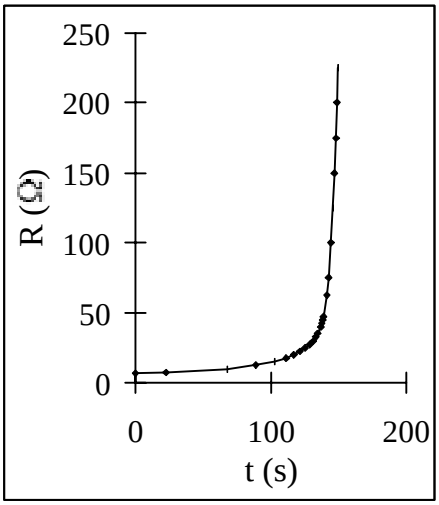

Figure 3.2: *Resistance as function of etching time measured with a four point probe.*

Clearly, the resistance strongly depends on etching time and goes to infinity when the dots are physically separated. In the present process Ar is used as etching gas with ion energy of 500 eV and beam current of 12.5 mA. Typical etch rate is 10 nm/min. The possible etching damage induced by the Ar ions would be limited within the penetration depth of the ions. As calculated by the TRIM software package [3.51] the penetration of Ar ions in the resist layers is only 5 nm at most, which means that only the magnetic material at the edges of the dots will be affected. Nevertheless, in the magnetization reversal this etching damage may play an

important role and considerably reduce the switching fields. Figure 3.3 shows a TEM image of an etched $Co_{50}Ni_{50}$/Pt multilayer dot prepared on top of a siliconnitride membrane. In this top-view image, the polycrystalline structure of the multilayer and a ring of redeposited material can clearly be seen. Also some edge roughness is observed. Clearly, this is of the order of 10 nm at most.

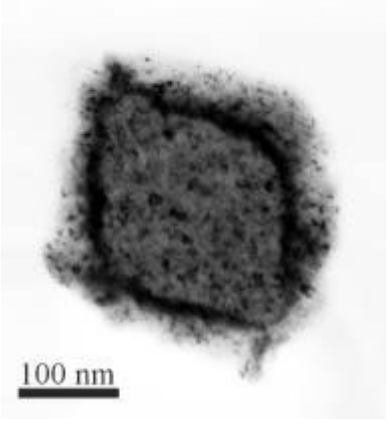

Figure 3.3: *TEM image of an etched $Co_{50}Ni_{50}$/Pt multilayer dot prepared on a siliconnitride membrane (image by K. Kirk, University of Glasgow).*

3.4 Interference pattern and resist structures

The patterning process described in the previous section is simple and straightforward. As described in Chapter 5 high quality samples of $Co_{50}Ni_{50}$/Pt multilayer dots have been prepared with this process. However, towards smaller dot sizes (< 100 nm) the desired disk-shape could clearly not be maintained. In order to understand these results a deeper knowledge of interference pattern and resist properties is necessary.

3.4.1 The role of substrate reflectivity

The first issue that should be discussed is the image of the interference pattern inside the resist layer. Though in principle the interference pattern would simply be a sinus in lateral direction, reflections at the substrate-resist interface add an unwanted modulation of intensity perpendicular to the substrate [3.22]. The period of this modulation Λ_z is given by:

$$\Lambda_z = \frac{\lambda}{2n_{resist}\cos\Theta_{resist}} \tag{3.2}$$

where n_{resist} and Θ_{resist} are the refractive index of the resist and the angle of incidence inside the resist layer respectively. In order to understand the relevance of this effect for the processing of $Co_{50}Ni_{50}$/Pt multilayer dots the true interference pattern inside the resist layer has been calculated in a similar way as done by Johnson *et al.* [3.22]

and Kapon *et al.* [3.52] for other reflective substrates. Since the multilayer is still slightly transparent for the thickness used in our experiments (i.e. 30 nm), also reflections at the underlying siliconoxide layer and silicon substrate are taken into account. The resulting trilayer model used for the calculation is shown in Figure 3.4.

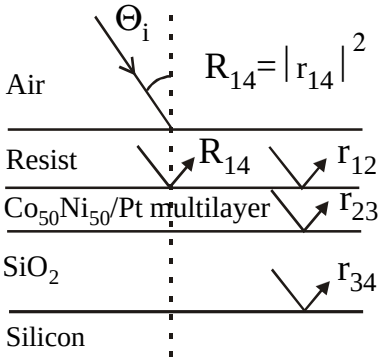

Figure 3.4: *Schematic model for the calculation of the interference pattern.*

The effective reflection coefficient r_{14} can be calculated from all individual reflection coefficients r_{ij}, which are given by the complex Fresnel equations (see e.g. [3.53]). For the interference patterns also the first internal reflection at the resist-air interface is taken into account. The data for the refractive indices of the materials used in this chapter is given in Table 3.2. All calculations have been carried out with Maple V and for the TE mode.
Figure 3.5 shows the calculated interference pattern for the cases of zero substrate reflectivity and for actual experimental conditions.

Table 3.2: *Refractive index, n (1+i κ), of relevant materials used in the calculation of interference patterns and substrate reflectivity.*

Material	**n**	**κ**
Resist [1]	1.72	0.017
Antireflective coating [2]	1.68	0.083
$Co_{50}Ni_{50}$/Pt multilayer [3]	1.5	1.73
SiO_2	1.47	0
Si	5.47	0.53

[1] Data for n are supplied by manufacturer, data for κ are derived from [3.54].
[2] For Brewer Science ARC-XL [3.54].
[3] From [3.55].

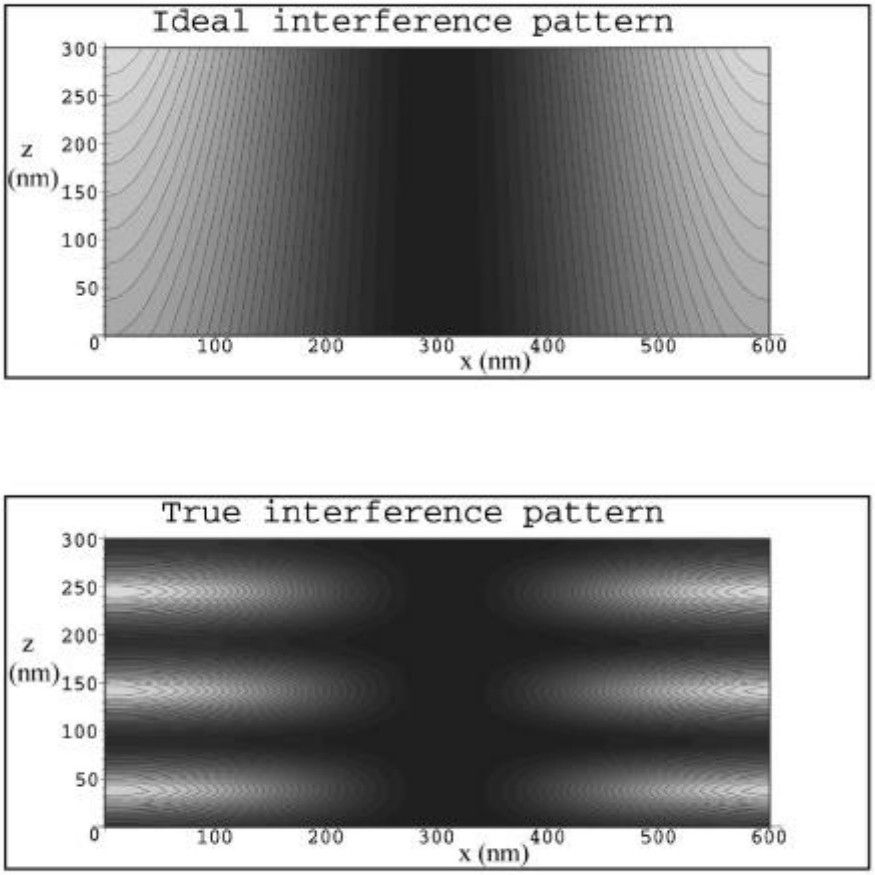

Figure 3.5: *Cross section of calculated interference pattern (z=height in the resist, x=lateral position) in a 300 nm resist layer during exposure at a period of 600 nm for two cases: Top = for zero substrate-reflectivity; Down = for the Si-SiO_2 (320 nm)-$Co_{50}Ni_{50}$/Pt (30 nm) substrate as used in the experiments (R=0.4).*

The effect of the large substrate reflectivity is clearly present. While in the absence of substrate reflections the interference pattern shows only absorption effects, a strong vertical modulation of light intensity appears in the interference pattern for the Si-SiO_2-$Co_{50}Ni_{50}$/Pt substrate. The period of the modulation is approximately 100 nm. Due to this modulation the development rate of the resist layer is highly inhomogenous and the resist needs to be overexposed to allow development to the bottom of the resist layer. Such properties lead to a strong decrease in process latitude. For instance, from the bottom image in Figure 3.5 one can learn that at z=140 nm the development in the lateral direction is much faster than the development in the vertical direction, leading to poor control of dot size. Also

experimental results show the effects of substrate reflectivity. Figure 3.6 shows two resist structures prepared on a Si-SiO_2-$Co_{50}Ni_{50}$/Pt substrate.

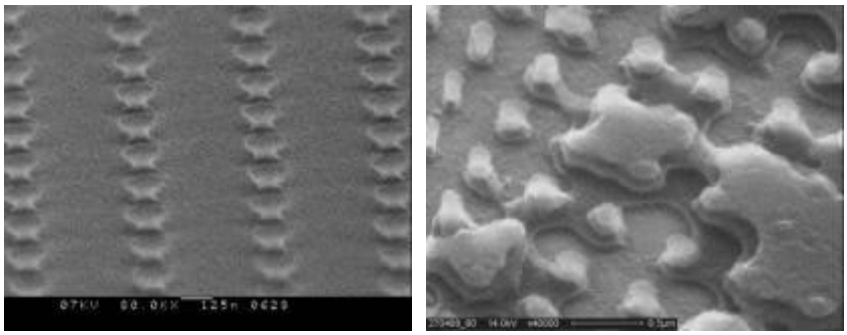

Figure 3.6: *SEM images of two resist patterns at a period of approximately 600 nm showing the effect of the presence of standing waves perpendicular to the substrate: Left = 'mushroom' resist dots prepared from a 120 nm resist layer; Right = unevenly developed 300 nm resist layer with plateaus corresponding to the intensity minima at 90, 190 and 290 nm (for this sample, diluted Olin 907 resist was used, exposed at 2x60 s.).*

The left image shows resist dots patterned from a 120 nm thick resist layer. As can be seen in Figure 3.5 at this thickness a strong local intensity minimum is present in the upper part of the resist. Therefore the resist dots have a mushroom shape with a small base and a broad top. The right image shows resist dots patterned from a 300 nm thick resist layer. In this case the resist has developed unevenly and shows three plateaus corresponding to the local intensity minima in the interference pattern of Figure 3.5.
The problems associated with the vertical modulation in intensity are clearly encountered in a series of exposures with increasing dose. As shown in Table 3.3, for a 120 nm resist layer the final dot size is rather unpredictable, while a proportional relationship between dot size and exposure dose would be desired.

Table 3.3: *Etched dot size vs. exposure time for a series of $Co_{50}Ni_{50}$/Pt multilayer dots at a period of 570 nm prepared from a 120 nm resist layer at a fixed laser power of 170* m*Watt/cm*^{2}.

t_{exp} (s)	d (nm)
2 x 120	280
2 x 150	180
2 x 180	280
2 x 210	140

If one would like to reproducably vary the dot size over a large range, the suppression of the vertical modulation is absolutely required. These problems may be overcome by using very thin resist layers ($d < z_{\text{first minimima}}$). However, this is only an option for the patterning of ultrathin layers.
Moreover, two other consequences of the vertical modulation, which have not been discussed here, are that the slopes of the dot's side walls will be only small and that a lift-off process is impossible due to the intensity minima at the resist-substrate interface.
As an intermediate conclusion, can be stated that the vertical modulation in light intensity in interference patterns can not be denied. Calculated images of the interference pattern greatly improve the understanding of this effect. In the next subsection the use of antireflective coatings to suppress the vertical modulation will be discussed.

3.4.2 Antireflective coatings

Several ways have been proposed to circumvent the problem of the vertical modulation of light intensity in interference lithography. Initially, a method based on a partial development of thick resist layers followed by the evaporation of a shadow mask and a reactive ion etch was generally used [3.23]. In recent years antireflective coatings have become commercially available due to the interest from IC industry and have shown to improve reproducibility of laser interference lithography considerably [3.54]. In a similar way as in the previous subsection the resulting interference pattern in a 300 nm resist layer on top of a 160 nm ARC layer has been calculated. Because the calculation was designed for only three layers, for this calculation the siliconoxide layer was omitted. Since the absorption in the ARC and multilayer will be nearly unity, the error made with this approximation can be neglected. Figure 3.7 shows the result. Clearly, the vertical modulation of light intensity is considerably suppressed compared to the configuration without an ARC layer in Figure 3.5. Further improvement of the interference pattern is possible by increasing the ARC thickness.
In this work Brewer Science ARC-XHRi was tested. A 160 nm ARC layer is spun on top of the Si-SiO_2-$Co_{50}Ni_{50}$/Pt substrate and baked at 120°C for 4 minutes. Figure 3.8 shows SEM images of a series of exposures with increasing dose. In this case, a clear proportional relation between feature size and exposure dose is observed. On the other hand, some details in the images can be attributed to the vertical modulation in light intensity. The resist dots exposed at 2x40 s. show some incompletely seperated dots due to undeveloped traces of resist associated at sites of local minima in the intensity pattern. Moreover, all dots and gratings show a broadening at the base. Anyway, as conclusion can be stated that the patterning process is considerably improved by the application of an antireflective coating.

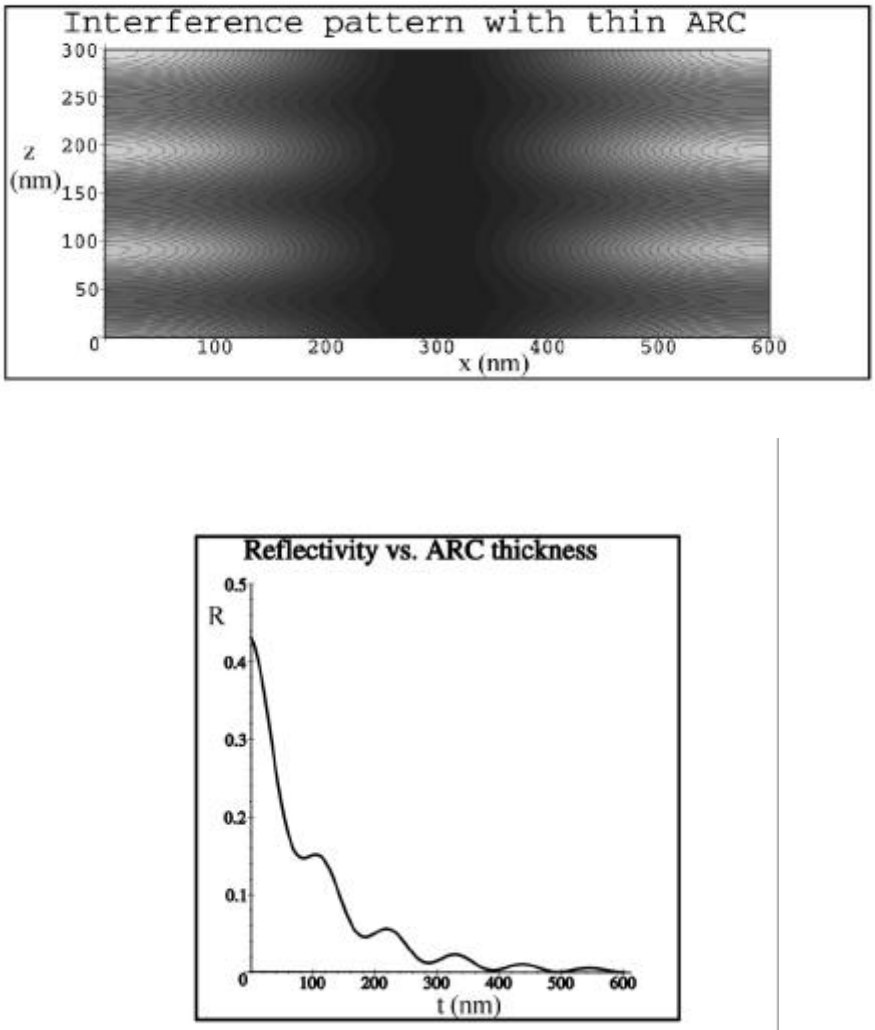

Figure 3.7: *Calculated interference pattern (top, ARC thickness = 160 nm) and substrate reflectivity (bottom) for a Si-$Co_{50}Ni_{50}$/Pt (30 nm)-ARC substrate at a period of 600 nm.*

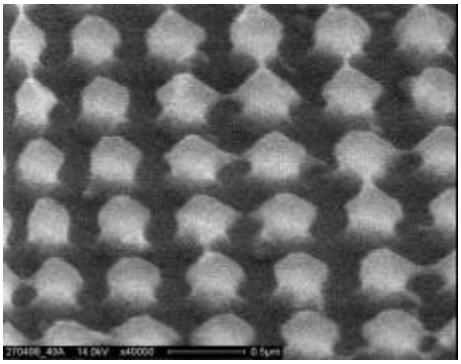

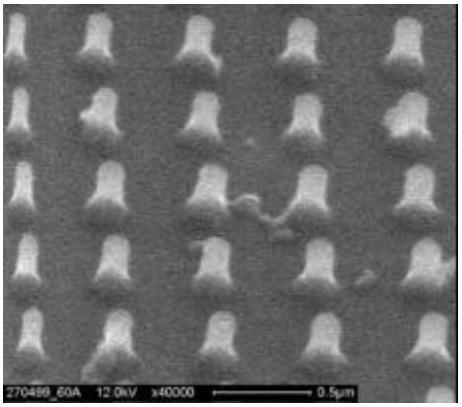

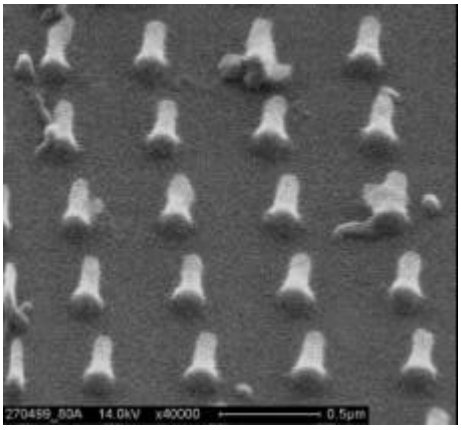

Figure 3.8: *SEM images of resist dots (period=550 nm) prepared in a 300 nm Olin 907 layer on top of a 160 nm ARC and a 30 nm $Co_{50}Ni_{50}$/Pt multilayer, with an exposure time of A = 2x40s, B = 2x60s and C = 2x80s.*

3.5 Limits of laser interference lithography

In the previous section only resist patterns with a period of 600 nm were discussed. In this section results on exposures at a period of 200 nm will be discussed. In principle, besides the increase in period of vertical modulation, the interference pattern at 200 nm is very similar to that at 600 nm. However, a series of exposure at increasing dose points to a much narrower process window (see Table 3.4).

Table 3.4: *Resist pattern vs. exposure time at a period of 200 nm prepared from a 60 nm resist layer at a fixed laser power of 170* m*Watt/cm*^{2}.

t_{exp} (s)	resist pattern
2 x 50	shallow
2 x 80	dots
2 x 110	overexposed

While minimum exposure times of approximately 2 x 60 s. are required to make any pattern at all, doubling of the exposure dose leads to overexposure of the whole resist layer. SEM images of resist patterns of two rather succesfull exposures are shown in Figure 3.9. Most important observation is that the developed resist structures are rounded, appear to have smaller thickness than the original resist layer and are only 80 nm wide at the base.

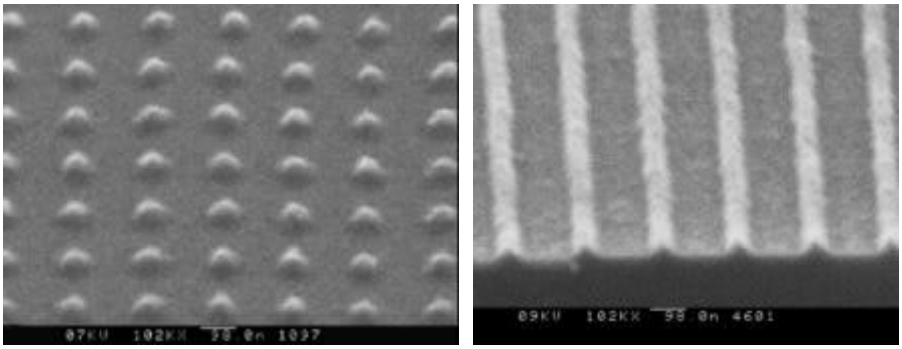

Figure 3.9: *Resist patterns at a period of 200 nm prepared from a 60 nm resist layer: Left = dots on top of a Si-SiO_2-$Co_{50}Ni_{50}$/Pt substrate; Right = lines on top of Si substrate.*

Now the possible origin of the decrease in process latitude for smaller periods will be discussed. Because in principle the development process stops at surfaces of constant intensity, the expected dot or line shape can be derived from the calculated interference pattern. In Figure 3.10 the expected dot or line shape is drawn for an 80 nm wide resist structure.

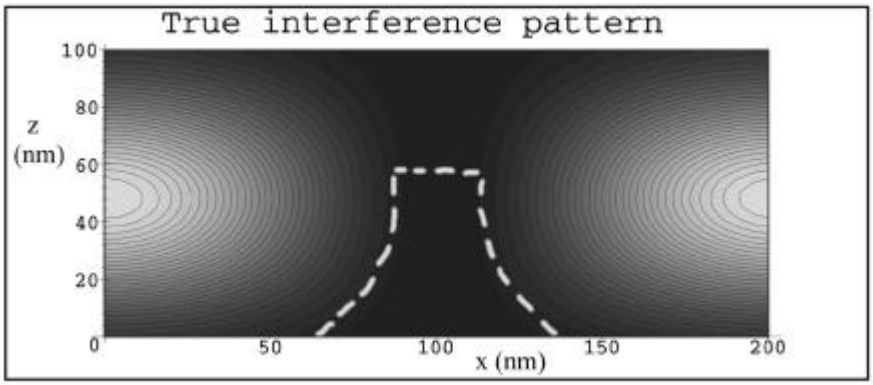

Figure 3.10: *Calculated interference pattern in a 100 nm resist layer on top of a Si-SiO_2 (320 nm)-$Co_{50}Ni_{50}$/Pt (30 nm) substrate at a period of 200 nm. The sketch represents the ideal resist structure with a base of 80 nm wide.*

This figure clearly shows that the rounding effect of the resist structure can not be explained by the interference pattern itself. Two other factors influencing the final resist structures can be discussed.
Firstly, the limited contrast of the resist will lead to a degradation of the expected resist structure. Since resists like Shipley 1800 are designed for use in broadband optical lithography of micron-sized dimensions, this surely is a relevant issue. Indeed, Schattenburg *et al.* have compared several resists and found that at sub 100 nm dimensions contrast properties of Shipley 1800 are inferior to those of other resists [3.54]. Moreover, contrast properties may strongly depend on the resist preparation and developer concentration [3.56,57]. Therefore, optimization of these parameters may be fruitfull.
Secondly, limitations of the exposure setup will play a role. Besides laser instabilities and air streams, substrate instabilities as drift or vibrations and intensity differences between the direct-incident and mirror-reflected beam may be important. Especially, the observation that at 200 nm period the resist layer is easily overexposed points to the presence of such effects. The former two effects should be suppressed by avoiding air displacements during exposure and optimizing laser operation. Since these effects were not encountered in the patterning of 600 nm period structures, apparently they play a minor role. The significance of the latter two effects can be determined by calculating their impact on the contrast present in the interference pattern. Therefore, a contrast parameter C is defined as the relative intensity ratio between a point in the bottom of the bright region and a point in the middle of the dark region of Figure 3.10:

$$C = \frac{I(x=0, z=20) - I(x=70, z=45)}{I(x=0, z=20)} \tag{3.3}$$

If C > 0 than there exists a combination of development time t_{dev} and exposure time t_{exp} for the preparation of a resist pattern. Moreover, process latitude is proportional to C. Ideally, C equals unity but, due to the sinus-like intensity pattern, this can never be achieved in interference lithography.
Now the contrast parameter can be calculated for the two different effects. The intensity differences between the two beams (due to beam positioning and non-unity reflectivity of the Al mirror) can simply be incorporated in the model. Substrate instabilities are more complicated to take into account. However, an approximation can be made by adding two interference patterns shifted over a distance corresponding to an average amplitude of the vibrations or distance of drift. The calculated contrast parameter is plotted in Figure 3.11 and 3.12 vs. beam intensity ratio respectively substrate instability.

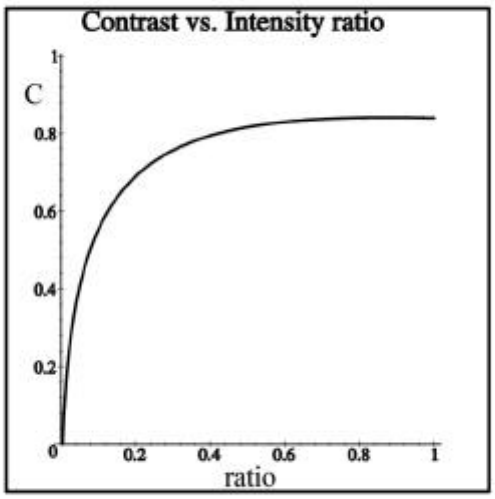

Figure 3.11: *Calculated contrast (as defined in the text) present in the exposed interference pattern as function of the ratio between the intensities of the direct incident and mirror-reflected beam for exposure conditions as in Figure 3.10.*

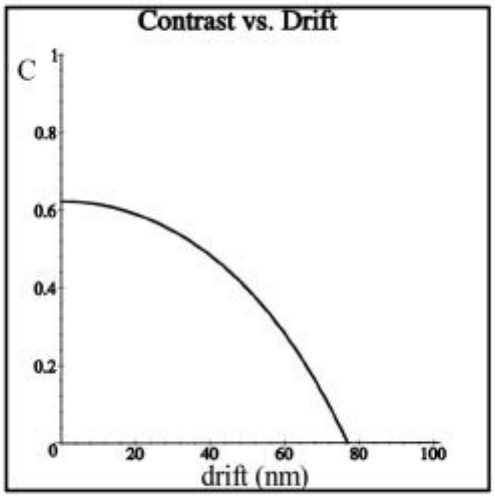

Figure 3.12: *Calculated contrast (as defined in the text) present in the exposed interference pattern as function of drift or vibration amplitude of the substrate for exposure conditions as in Figure 3.10.*

A typical experimental beam intensity ratio is at least 0.6. Apparently, for such a value still plenty of contrast is present in the interference pattern. Note, that for reflectivity = 0 and ratio = 1, the contrast is maximum and equals 0.75. On the other hand, substrate instabilities have a much more dramatic effect. Though it is difficult to estimate the actual substrate instabilities, they can surely be a significant source for a reduction of process latitude and consequently lead to a degradation of resist structures.
Finally, it should be strongly emphasized that the impact of the reduction of contrast in the interference pattern due to the described problems is also dependent on the intrinsic contrast properties of the resist itself. Therefore, for a higher contrast resist, in combination with an antireflective coating, the process window is larger and the quality of resist structures greatly improves (see Figure 3.13). A thorough study of the relation between dot size and exposure time would be necessary to really quantify the limitations in the present exposure setup.

As a conclusion of this discussion, several guidelines for improvement of the patterning process can be given:

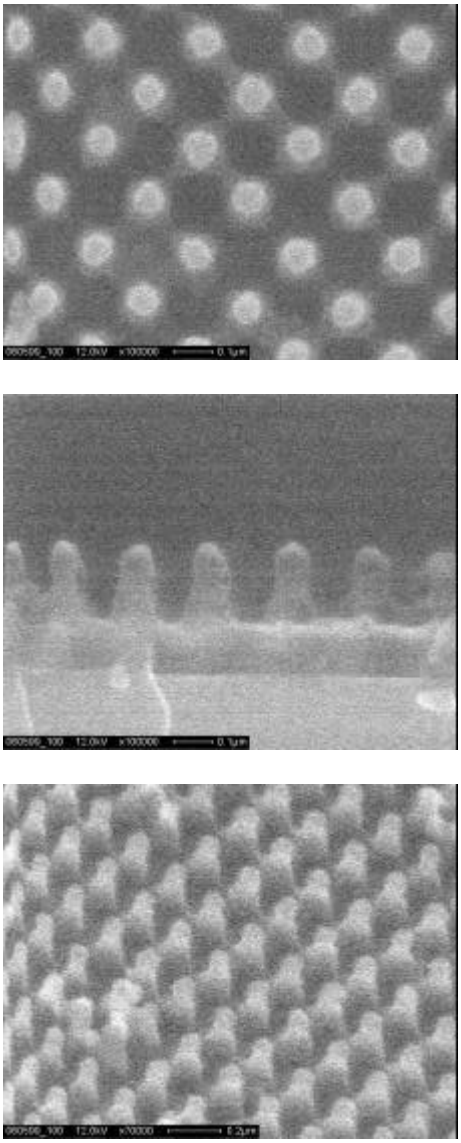

Figure 3.13: *SEM images of resist dots (period=200 nm) prepared in a 200 nm Olin 907 layer on top of a 160 nm ARC and a silicon substrate (exposure time = 2x100s).*

- Application of higher contrast resists and developers (less influence of a decrease of contrast parameter on process latitude).
- Application of ARC (reduces exposure times and improves the process latitude).

- Decrease of exposure time in one of the following ways: 1) by increasing power density via an increase in laser power or a decrease in substrate-pinhole distance at the cost of a decrease in area and uniformity over area; 2) by choosing resists with increased sensitivity.

Moreover, when pushing the patterning process to its limits, exposure time and development time should be chosen with care. In this respect, end-point detection of the development process would be advantageous [3.58].

3.6 Summary and outlook

In this chapter the patterning technology for our studies on submicron patterned magnetic thin films has been motivated and discussed. A review of existing submicron patterning technologies showed that laser interference lithography uniquely combines simplicity, large areas and sub 100 nm dimensions. With the present process sub-100 nm resist structures at a period of 200 nm can be prepared. However, at these dimensions the process latitude is limited. With a higher contrast resist in combination with an antireflective coating considerable improvement is achieved. Further progress may be limited by instabilities of the present exposure setup.

At present the minimum period of the interference pattern is 200 nm. For a further decrease of feature dimensions the wavelength of the laser should be decreased. Recently, Hinsberg *et al.* showed interference lithography with a laser wavelength of 257 nm and the application of deep UV resists with high contrast [3.59]. Lasers with even smaller wavelength have poor temporal and spatial coherence and are therefore not suitable for laser interference lithography. However, achromatic interference lithography with ArF excimer lasers at 193 nm has the capability of patterning resist structures with periods of 100 nm [3.60,61]. The principle of the technique is the use of an exposure setup with vanishingly small difference in the length of the two light paths. Yen *et al.* proposed that this technique can be expanded for the patterning of structures with 50 nm period [3.62].

References

[3.1] M. Rothschild, J.A. Burns, S.G. Cann, A.R. Forte, C.L. Keast, R.R. Kunz, S.C. Palmateer, J.H.C. Sedlacek, R. Uttaro, A. Grenville, and D. Corliss, *'How practical is 193 nm lithography'*, J. Vac. Sci. Technol. B **14** (1996) 4157-4161.

[3.2] SEMATECH, *'The National Technology Roadmap for Semiconductors'* (1997).

[3.3] J.P. Silverman, *'Challenges and progress in x-ray lithography'*, J. Vac. Sci. Technol. B **16** (1998) 3137-3141.

[3.4] C.W. Gwyn, R. Stulen, D. Sweeney, and D. Attwood, *'Extreme ultraviolet lithography'*, J. Vac. Sci. Technol. B **16** (1998) 3142-3149.

[3.5] S.T. Stanton, J.A. Liddle, W.K. Waskiewicz, and A.E. Novembre, *'Critical dimension control at stitched subfield boundaries in a high-throughput SCALPEL® system'*, J. Vac. Sci. Technol. B **16** (1998) 3197-3201.

[3.6] G. Gross, R. Kaesmaier, H. Löschner, and G. Stengl, *'Ion projection lithography: Status of the MEDEA project and United States/European cooperation'*, J. Vac. Sci. Technol. B **16** (1998) 3150-3153.

[3.7] F. Rousseaux, D. Decanini, F. Carcenac, E. Cambril, M.F. Ravet, C. Chappert, N. Bardou, B. Bartenlian, and P. Veillet, *'Study of large area high density magnetic dot arrays fabricated using synchotron radiation based x-ray lithography'*, J. Vac. Sci. Technol. B **13** (1995) 2787-2791.

[3.8] H. Schmid, H. Biebuyck, B. Michel, O.J.F. Martin, and N.B. Piller, *'Light-coupling masks: An alternative, lensless approach to high-resolution optical contact lithography'*, J. Vac. Sci. Technol. B **16** (1998) 3422-3425.

[3.9] M.M. Alkaisi, R.J. Blaikie, and S.J. McNab, *'Nanolithography using wet etched silicon nitride phase masks'*, J. Vac. Sci. Technol. B **16** (1998) 3929-3933.

[3.10] R.J. Blaikie, M.M. Alkaisi, S.J. McNab, D.R.S. Cumming, R. Cheung, and D.G. Hasko, *'Nanolithography using optical contact exposure in the evanescent near field'*, Microelectronic Engineering, in press.

[3.11] S.Y. Chou, P.R. Krauss, and L. Kong, *'Nanolithographically defined magnetic structures and quantum magnetic disk'*, J. Appl. Phys. **79** (1996) 6101-6106.

[3.12] R.W. Jaszweski, H. Schift, J. Gobrecht, and P. Smith, *'Hot embossing in polymers as a direct way to pattern resist'*, Microelectronic Engineering **41/42** (1998) 575-578.

[3.13] X.M. Zhao, Y. Xia, and G.M. Whitesides, *'Soft lithographic methods for nano-fabrication'*, J. Mater. Chem. **7** (1997) 1069-1074.

[3.14] L. Kong, L. Zhuang, M. Li, B. Cui, and S.Y. Chou, *'Fabrication, writing and reading of 10 Gbits-in^2 longitudinal quantized magnetic disks with a switching field over 1000 Oe'*, Jpn. J. Appl. Phys. **37** (1998) 5973-5975.

[3.15] H.C. Scheer, H. Schulz, T. Hoffmann, and C.M. Sotomayor Torres, *'Problems of the nanoimprinting technique for nanometer scale pattern definition'*, J. Vac. Sci. Technol. B **16** (1998) 3917-3921.

[3.16] H.A. Biebuyck, N.B. Larsen, E. Delamarche, and B. Michel, *'Lithography beyond light: Microcontact printing with monolayer resists'*, IBM J. Res. Develop. **41** (1997) 159-170.

[3.17] S. Zhu, R.J. Gambino, M.H. Rafailovich, J. Sokolov, S.A. Schwarz, and R.D. Gomez, *'Microscopic magnetic characterization of submicron cobalt islands prepared using self assembled polymer masking technique'*, IEEE Trans. Magn. **33** (1997) 3022-3024.

[3.18] O. Dial, C.C. Cheng, and A. Scherer, *'Fabrication of high-density nanostructures by electron beam lithography'*, J. Vac. Sci. Technol. B **16** (1998) 3887-3890.

[3.19] R.M.H. New, R.F.W. Pease, and R.L. White, *'Submicron patterning of thin cobalt films for magnetic storage'*, J. Vac. Sci. Technol. B **12** (1994) 3196-3201.

[3.20] P.R. Krauss, and S.Y. Chou, *'Fabrication of planar quantum magnetic disk structure using electron beam lithography, reactive ion etching and chemical mechanical polishing'*, J. Vac. Sci. Technol. B **13** (1998) 2850-2852.

[3.21] R. O'Barr, S.Y. Yamamoto, S. Schultz, W. Xu, and A. Scherer, *Fabrication and characterization of nanoscale arrays of nickel columns'*, J. Appl. Phys. **81** (1997) 4730-4732.

[3.22] L.F. Johnson, G.W. Kammlott, and K.A. Ingersoll, *'Generation of periodic surface corrugations'*, Applied Optics **17** (1978) 1165-1181.

[3.23] E.H. Anderson, C.M. Horwitz, and H.I. Smith, *'Holographic lithography with thick photoresist'*, Appl. Phys. Lett. **43** (1983) 874-875.

[3.24] J.P. Spallas, A.M. Hawryluk, and D.R. Kania, *'Field emitter array mask patterning using laser interference lithography'*, J. Vac. Sci. Technol. B **13** (1995) 1973-1978.

[3.25] X. Chen, S.H. Zaidi, S.R.J. Brueck, and D.J. Devine, *'Interferometric lithography of sub-micrometer sparse hole arrays for field-emission display applications'*, J. Vac. Sci. Technol. B **14** (1996) 3339-3349.

[3.26] J. Nole, *'Holographic lithography needs no mask'*, Laser Focus World (1997) 209-212.

[3.27] A. Fernandez, P.J. Bedrossian, S.L. Baker, S.P. Vernon, and D.R. Kania, *'Magnetic force microscopy of single-domain cobalt dots patterned using interference lithography'*, IEEE Trans. Magn. **32** (1996) 4472-4474.

[3.28] E.F. Wassermann, M. Thielen, S. Kirsch, A. Pollmann, H. Weinforth, and A. Carl, *'Fabrication of large scale periodic magnetic nanostructures'*, J. Appl. Phys. **83** (1998) 1753-1757.

[3.29] M. Farhoud, M. Hwang, H.I. Smith, M.L. Schattenburg, J.M. Bae, K. Youcef-Toumi, and C.A. Ross, *'Fabrication of large area nanostructured magnets by interferometric lithography'*, IEEE Trans. Magn. **34** (1998) 1087-1089.

[3.30] M.A.M. Haast, J.R. Schuurhuis, L. Abelmann, J.C. Lodder, and Th.J.A. Popma, *'Reversal mechanism of submicron patterned CoNi/Pt multilayer dots'*, IEEE Trans. Magn. **34** (1998) 1006-1008.

[3.31] D.H. Raguin, and G.M. Morris, *'Structured surfaces mimic coating performance'*, Laser Focus World (1997) 113-117.

[3.32] V. Berger, O. Gauthier-Lafaye, and E. Costard, *'Photonic band gaps and holography'*, J. Appl. Phys. **82** (1997) 60-64.

[3.33] C.J.M. van Rijn, G.J. Veldhuis, and S. Kuiper, *'Nanosieves with microsystem technology for microfiltration applications'*, Nanotechnology **9** (1998) 343-345.

[3.34] W. Wu, B. Cui, X.Y. Sun, W. Zhang, L. Zhuang, L. Kong, and S.Y. Chou, *'Large area high density quantized magnetic disks fabricated using nanoimprint lithography'*, J. Vac. Sci. Technol. B **16** (1998) 3825-3829.

[3.35] M.L. Schattenburg, C.R. Canizares, D. Dewey, K.A. Flanagan, A. Hammett, A.M. Levine, K.S.K. Lam, R. Manikkalingam, T. Markert, and H.I. Smith, *'Transmission grating spectroscopy and the Advanced X-ray Astrophysics Facility'*, Opt. Eng. **30** (1991) 1590-1600.

[3.36] J.P. Spallas, R.D. Boyd, J.A. Britten, A. Fernandez, A.M. Hawryluk, M.D. Perry, and D.R. Kania, *'Fabrication of sub-0.5 mm diameter cobalt dots on silicon substrates and photoresist pedestals on 50 cm x 50 cm glass substrates using laser interference lithography'*, J. Vac. Sci. Technol. B **14** (1996) 2005-2007.

[3.37] M.A.M. Haast, I.R. Heskamp, L. Abelmann, J.C. Lodder, and Th.J.A. Popma, *'Magnetic characterization of large area arrays of single and multi domain CoNi/Pt multilayer dots'*, J. Magn. Magn. Mat. **193** (1999) 511-514.

[3.38] R. Allenspach, A. Bischof, U. Dürig, and P. Grütter, *Local modification of magnetic properties by an electron beam'*, Appl. Phys. Lett. **73** (1998) 3598-3600.

[3.39] T. Aign, P. Meyer, S. Lemerle, J.P. Jamet, J. Ferré, V. Matthet, C. Chappert, J. Gierak, C. Vieu, F. Rousseaux, H. Launois, and H. Bernas, *'Magnetization reversal in arrays of perpendicularly magnetized ultrathin dots coupled by dipolar interaction'*, Phys. Rev. Lett. **81** (1998) 5656-5659.

[3.40] K. Bessho, Y. Iwasaki, and S. Hashimoto, *'Fabricating nanoscale magnetic mounds using a scanning probe microscope'*, J. Appl. Phys. **79** (1996) 5057-5059.

[3.41] J. Tersoff, C. Teichert, and M.G. Lagally, *'Self-organization in growth of quantum dot superlattices'*, Phys. Rev. Lett. **76** (1996) 1675-1678.

[3.42] C. Teichert, J. Barthel, H.P. Oepen, and J. Kirschner, *Fabrication of nanomagnet arrays by shadow deposition on self-organized semiconductor substrates'*, Appl. Phys. Lett. **74** (1999) 588-590.

[3.43] R.J. Celotta, R. Gupta, R.E. Scholten, and J.J. McCelland, *'Nanostructure fabrication via laser-focussed atomic deposition'*, J. Appl. Phys. **79** (1996) 6079-6083.

[3.44] W. Lu, K.G.H. Baldwin, M.D. Hoogerland, S.J. Buckman, T.J. Senden, T.E. Sheridan, and R.W. Boswell, *'Sharp edged silicon structures generated using atom lithography with metastable helium atoms'*, J. Vac. Sci. Technol. B **16** (1998) 3846-3849.

[3.45] J.H. Thywissen, K.S. Johnson, N.H. Dekker, A.P. Chu, and M. Prentiss, *'Using neutral atoms and standing light waves to form a calibration artifact for length metrology'*, J. Vac. Sci. Technol. B **16** (1998) 3841-3845.

[3.46] J. Fujita, T. Kisimoto, M. Morinaga, S. Matsui, and F. Shimizu, *'Atomic beam holography for nanofabrication'*, J. Vac. Sci. Technol. B **16** (1998) 3855-3858.

[3.47] J.H. Berends, *'Integrated optical Bragg reflectors as narrow-band wavelength filters'*, Ph.D. thesis, University of Twente 1997.

[3.48] A. Fernandez, H.T. Nguyen, J.A. Britten, R.D. Boyd, M.D. Perry, D.R. Kania, and A.M. Hawryluk, *'Use of interference lithography to pattern arrays of submicron resist structures for field emission flat panel displays'*, J. Vac. Sci. Technol. B **15** (1997) 729-735.

[3.49] A. Fernandez, J.Y. Decker, S.M. Herman, D.W. Phillion, D.W. Sweeney, and M.D. Perry, *'Methods for fabricating arrays of holes using interference lithography'*, J. Vac. Sci. Technol. B **15** (1997) 2439-2443.

[3.50] C. Chappert, H. Bernas, J. Ferré, V. Kottler, J.P. Jamet, Y. Chen, E. Cambril, T. Devolder, F. Rousseaux, V. Mathet, and H. Launois, *'Planar patterned magnetic media obtained by ion irradiation'*, Science **280** (1998) 1919-1922.

[3.51] Transport of Ions in Matter (TRIM) software package, written by J.F. Ziegler.

[3.52] E. Kapon, and A. Katzir, *'Photoresist gratings on reflecting surfaces'*, J. Appl. Phys. **53** (1982) 1387-1390.

[3.53] M.A. Born, and E. Wolf, *'Principles of Optics'* (6^{th} ed.) Pergamon Press (1980).

[3.54] M.L. Schattenburg, R.J. Aucoin, and R.C. Fleming, *'Optically matched trilevel resist process for nanostructure fabrication'*, J. Vac. Sci. Technol. B **15** (1995) 3007-3011.

[3.55] R. Atkinson, S. Pahirathan, I. W. Salter, P. J. Grundy, C. J. Tatnall, J. C. Lodder, and Q. Meng, *'Fundamental optical and magneto-optical constants of Co/Pt and CoNi/Pt multilayered films'*, J. Magn. Magn. Mater. **162** (1996) 131-138.

[3.56] B. de A. Mello, I.F. da Costa, C.R.A. Lima, and L. Cescato, *'Developed profile of holographically exposed photoresist gratings'*, Applied Optics **34** (1995) 597-603.

[3.57] V. Marriott, Y.C. Lin, and G. Fuller, *'Resolution enhancement of positive photoresist through optimization of thermal processing'*, SPIE **469** (1984) 65-71.

[3.58] H. Kawata, N. Kasamatsu, and K. Murata, *'Holographic lithography with endpoint detection of resist development'*, Jpn. J. Appl. Phys. **32** (1993) 3321-3327.

[3.59] W. Hinsberg, F.A. Houle, J. Hoffnagle, M. Sanchez, G. Wallraff, M. Morrison, and S. Frank, *'Deep-ultraviolet interferometric lithography as a tool for assessment of chemically amplified photoresist performance'*, J. Vac. Sci. Technol. B **16** (1998) 3689-3694.

[3.60] T.A. Savas, S.N. Shah, M.L. Schattenburg, J.M. Carter, and H.I. Smith, *'Achromatic interferometric lithography for 100 –nm-period gratings'*, J. Vac. Sci. Technol. B **13** (1995) 2732-2735.

[3.61] A. Yen, E.H. Anderson, R.A. Ghanbari, M.L. Schattenburg, and H.I. Smith, *'Achromatic holographic configuration for 100-nm-period lithography'*, Applied Optics **31** (1992) 4540-4545.

[3.62] A. Yen, M.L. Schattenburg, and H.I. Smith, *'Proposed method for fabricating 50-nm-period gratings by achromatic holographic lithography'*, Applied Optics **31** (1992) 2972-2973.

Chapter 4

Preparation and characterization of $Co_{50}Ni_{50}$/Pt multilayers

In this chapter a study on the magnetic and structural properties of sputtered $Co_{50}Ni_{50}$/Pt multilayers is presented. The origin of the magnetic anisotropy and its relation with the deposition parameters are discussed. At the end the deposition parameters are selected for the application of the multilayers as a patterned medium.

4.1 Introduction

In the mid-1980's Carcia *et al.* [4.1-2] discovered the perpendicular magnetic anisotropy in Co/Pt and Co/Pd multilayers. Due to their potential interest for magneto-optic recording these multilayers have attracted great interest and their properties have extensively been studied [4.3-6]. Despite of promising results the relatively high Curie temperature of Co-based multilayers remained an issue. This problem could be overcome by replacing the Co layer by a $Co_{1-x}Ni_x$-alloy layer [4.7-11]. The Curie temperature has considerably been reduced while other magnetic and magneto-optic properties, like the perpendicular magnetic anisotropy and polar Kerr rotation, hardly deteriorated.
The numerous studies on Co- and CoNi-based multilayers show that, if deposited under the right conditions, these multilayers may have both a strong intergranular exchange coupling and a large perpendicular magnetic anisotropy. Therefore Co- and CoNi-based multilayers may be very suitable for application as patterned medium (see also Chapter 2). It is interesting to note that the recording principle of such a medium then could be either based on magnetic probes or on magneto-optic technology. Moreover, the large polar Kerr rotation provides the possibility to benefit from sensitive characterization tools, such as Polar Kerr Magnetometry and Microscopy. Motivated by these expectations, sputtered $Co_{50}Ni_{50}$/Pt multilayers were selected as magnetic material for our research on magnetic micro- and nanostructures. In order to optimize the multilayer's properties for application as patterned medium a profound study into the relation between their deposition parameters, microstructure and magnetic anisotropy has been carried out. Besides, through this study, our knowledge concerning the sputtering process could be expanded.

4.2 Deposition by magnetron sputtering

The deposition method used in this work is magnetron sputtering. In this section, firstly, some of the details and physical background of this technology will be discussed to make clear that growth features can be related to the deposition pressure. Then the relation between these growth features and magnetic anisotropy will be discussed. Finally, the experimental approach to our study will be outlined.

4.2.1 Technology

The sputtering system (VSW Inc.) has two 2'' circular planar magnetrons. Due to its specific configuration the plasma (incl. electrons) is confined within approximately 1'' distance from the targets [4.12]. Since the target to substrate distance is 100 mm, this means that the substrate is completely saved from plasma damage. The base pressure of the system is smaller than $5 \cdot 10^{-8}$ mbar and a loadlock provides a high sample throughput. The sputtering gas is Argon and the deposition pressure can be varied from 6 to 36 μbar. The deposition rates are kept low for a good control of layer thickness and assure a smooth layer growth. Pt is DC (30 W, V ≈ 400 V) sputtered with a typical deposition rate of 1.6 Å/s. $Co_{50}Ni_{50}$ is RF (40 W, 13.52 MHz) sputtered with a typical deposition rate of 0.5 Å/s. A more extensive description of the system can be found elsewhere [4.13].

4.2.2 Thin film growth by sputtering

In the sputtering process the kinetic energy of the incident atoms plays an important role in the growth of the thin-film's microstructure. In a discussion of the incident energy flux not only the sputtered atoms itself should be taken into account but also the gas neutrals reflected from the target. The latter arise from ions, which are accelerated through the plasma sheath and are neutralized upon reflection on the target. On their way from the target to the substrate both type of atoms are thermalized in the sputtering gas. Their incident energy is therefore considerably lower than their initial kinetic energy. The degree of thermalization is strongly dependent on the deposition pressure, target to substrate distance, target composition and sputtering gas. Following the calculations of Somekh [4.14], the kinetic energy of the incident atoms has been estimated for the case of the sputtering of Pt and CoNi in our process. The results are shown in Table 4.1. Because there is only little difference in the energies of sputtered Pt resp. Co/Ni atoms, no discrimination has been made between these two.
Clearly, the energetic bombardment of the reflected Ar neutrals is dominant when depositing Pt but drastically decreases with increasing Ar pressure. The energy of the deposited atoms decreases as well, even with two orders of magnitude over this range of Ar pressure. Due to the large variation in the energy of incident atoms, the thin film growth can be expected to be strongly dependent on the deposition pressure, especially in the case of Pt.

Table 4.1: *Estimated energies of Ar neutrals reflected from the targets, $E_{Ar,Pt}$ resp. $E_{Ar,CoNi}$, and of the sputtered atoms itself, E_{atoms} , bombarding the substrate as a function of deposition pressure (following the calculations in [4.14]).*

p (μbar)	$E_{Ar,Pt}$ (eV)	$E_{Ar,CoNi}$ (eV)	E_{atoms} (eV)
6	90	6	10
12	50	4	6
36	8	0.5	0.1

Indeed, Bijker *et al.* [4.15] have shown strong effects of the deposition pressure on the microstructure of CoNi/Pt multilayers. At high deposition pressure voids appeared in the thin film. The cause of the void formation is the high degree of scattering of the sputtered atoms combined with their very low kinetic energy. Obviously, the state of the interfaces in such multilayers will also depend on deposition pressure. Under the high energy bombardment at low Ar pressure or at the low deposition energies at high Ar pressure, alloyed respectively rough interfaces may be expected (see Figure 4.1).

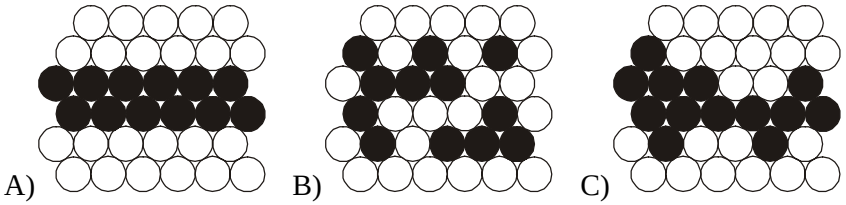

Figure 4.1: *Schematic drawing of three different types of interfaces in multilayers: A) atomically sharp and smooth; B) (non-ordered) alloyed; C) atomically rough.*

Before discussing the relation between these deposition features to properties as magnetic anisotropy, some additional notes should be made with respect to the expected crystallographic structure of sputtered $Co_{50}Ni_{50}$/Pt multilayers. $Co_{50}Ni_{50}$ and Pt are both fcc metals, but have a lattice mismatch of approximately 10%. Though an epitaxial growth can not be expected, still a strong correlation between the texture of the two layers may exist. The interface will then be incoherent and both layers have different and/or inhomogeneous (in-plane) lattice spacings. For Co/Pt multilayers where fcc to hcp phase transitions may occur in the Co layer, several interesting growth features have been revealed by X-Ray Diffraction [4.16] and High Resolution Electron Microscopy [4.17-19]. These studies show that both the interface structure and the crystallographic phase is also highly dependent on the designed layer geometry (i.e. number of bilayers, individual layer thicknesses, with or without underlayer etc.).

4.2.3 Deposition pressure and magnetic anisotropy

In addition to the void formation, Bijker *et al.* [4.15] noticed a large increase in perpendicular anisotropy with increasing deposition pressure. The origin of the latter effect could not be fully clarified. In principle, an analysis of the relation between deposition pressure and magnetic anisotropy of multilayers requires a large set of samples and an extensive structural and magnetic characterization. The main problem is that all the contributions to the magnetic anisotropy (as discussed in Chapter 2) may have a different dependence on deposition pressure due to their strong relation with microstructural properties as crystal orientation, interfacial roughness, interfacial mixing, columnar growth and intralayer strain. This can be illustrated by refering to several studies concerning Co/Pt multilayers.
As has firstly been recognized by Carcia *et al.* [4.20], energetic bombardment of a growing Co/Pt multilayer by recoiling neutrals may cause a severe mixing of the individual layers and degrade the (perpendicular) interface anisotropy. Indeed, the energetic neutrals reflected from the target could explain the dependence of the effective magnetic anisotropy on the deposition pressure and gas to a large extent. On the other hand Kim *et al.* [4.21] found that the interface anisotropy of Co/Pt multilayers as function of the deposition pressure shows a maximum at intermediate pressure. They proposed that, besides the energetic bombardment, also the interface roughness might play a role. In fact, they found a strong correlation between interface roughness and interface anisotropy. Although both studies were carried out in a similar sputtering geometry, they seem to have given partially contradicting results. However, the thickness of the studied multilayers differed enormously in both experiments. Moreover, in both papers no crystallographic data has been reported. The importance of the crystal orientation is shown by Lee *et al.* [4.22]. They have grown Co/Pt multilayers with three different crystal orientations by molecular beam epitaxy. The effective magnetic anisotropy was strongly perpendicular for (111) orientation and strongly in-plane for (001) orientation. An intermediate behaviour was observed for (110) orientation.

4.2.4 Experiments

Clearly, it is not really fair or possible at all to make a comparison between the different studies. With reference to the mentioned studies we aimed to make an unambiguous analysis of the pressure and thickness dependence of the magnetic anisotropy in $Co_{50}Ni_{50}$/Pt multilayers. For this purpose, five series of multilayers have been deposited at a broad range of deposition pressures and with varying layer geometry. The multilayers have been subjected to an extensive magnetic and structural analysis. The deposition conditions are shown in Table 4.2. At every condition, nine multilayers have been prepared with 2 Å < t_{CoNi} < 30 Å.

Table 4.2: *Deposition conditions of the series of {Pt underlayer} / {$Co_{50}Ni_{50}$ (t_{CoNi})/Pt (t_{Pt})} x N multilayers studied in this work.*

Name of series	Pressure (μbar)	Pt underlayer (Å)	t_{Pt} (Å)	N
p6	6	100	6.5	17
wsnb12	12	7.2	7.2	9
ws12	12	7.2	7.2	17
p12	12	104	6.6	17
p36	36	110	8.0	17

Magnetization and effective magnetic anisotropy were measured on a home built VSM and Torque Magnetometer respectively. Low and high angle X-Ray Diffraction analysis have been done on a Philips PW 1820/00 x-ray goniometer using Cu K_α radiation (40 kV, 30 mA). The GIXA software [4.23] has been used to determine the layer thickness and surface roughness. The multilayers have been deposited on oxidized Si(100) substrates. It should be noted that multilayers deposited on quartz substrates showed equal values for the magnetic anisotropy.
Now, firstly, the growth of single Pt and $Co_{50}Ni_{50}$ layers will be discussed to get some idea of the crystal quality of sputtered thin films. Then the multilayer growth is described. This will be followed by an analysis of the contributions to the magnetic anisotropy and their relation with the total film thickness at a single (intermediate) pressure (series wsnb12, ws12 and p12). Finally, the results on the pressure dependence of magnetic anisotropy will be presented (series p6, p12 and p36).

4.3 Texture in sputtered $Co_{50}Ni_{50}$ and Pt thin films

In the same time period when this work was carried out, Shimatsu *et al.* [4.24] studied on the same deposition system the crystalline quality of Pt thin films deposited on Si(100) substrates. They showed that at low deposition pressure the layers are very smooth and have only one crystallographic orientation perpendicularly to the substrate's plane, i.e. a strong (111) texture (see Figure 4.2). Moreover, they showed that the grain orientation and roughness drastically deteriorate at high deposition pressure. The question arises whether these results are also valid for Pt thin films deposited on oxidized Si substrates. In particular, the formation of platinasilicide in the deposition on non-oxidized Si substrates may significantly influence the thin film growth. Therefore, a similar study has been carried out and the results will be presented here. Besides, for a good understanding of the multilayer growth, the growth of single $Co_{50}Ni_{50}$ thin films will be discussed. Please note that the analysed samples were selected because they are simply relevant for the discussion about the magnetic anisotropy later in this chapter. A full study of the growth itself would certainly require more research.

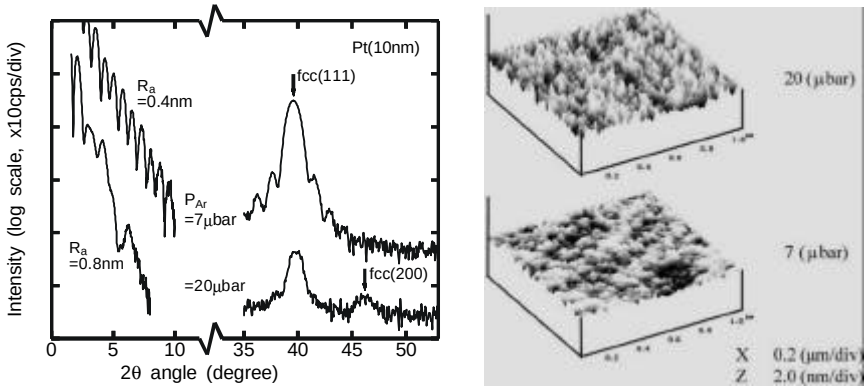

Figure 4.2: *Low and high angle XRD patterns (top) and AFM images (bottom) of single Pt thin films (10 nm) deposited on Si(100) at 7 and 20* mbar *(from [4.24]).*

4.3.1 XRD analysis of Pt thin films

Figures 4.3A-C show the XRD analysis of Pt thin films deposited at different deposition pressure and with different thickness.

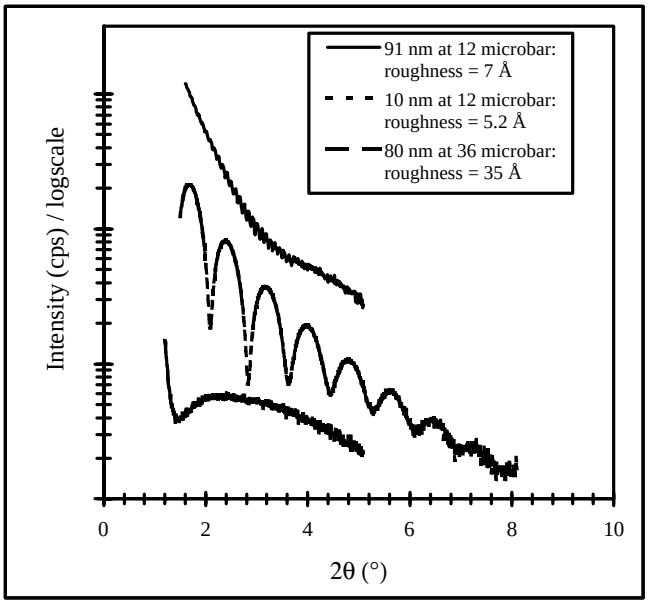

Figure 4.3A: *Low angle XRD patterns of single Pt thin films deposited on thermally oxidized Si(100) at 12 and 36* mbar*. The order of the entries in the legend corresponds to the order of the curves. The surface roughness and layer thickness have been determined from simulations with GIXA [4.23].*

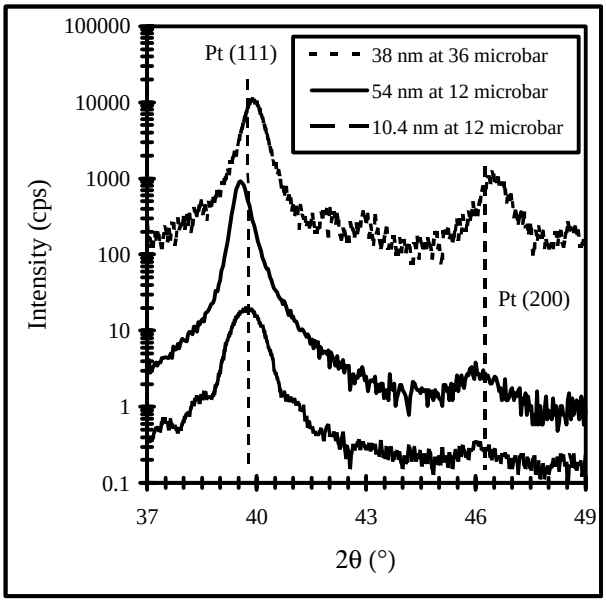

Figure 4.3B: *High angle XRD patterns of single Pt thin films deposited on thermally oxidized Si(100) at 12 and 36* mbar*. The curves have been shifted for clarity.*

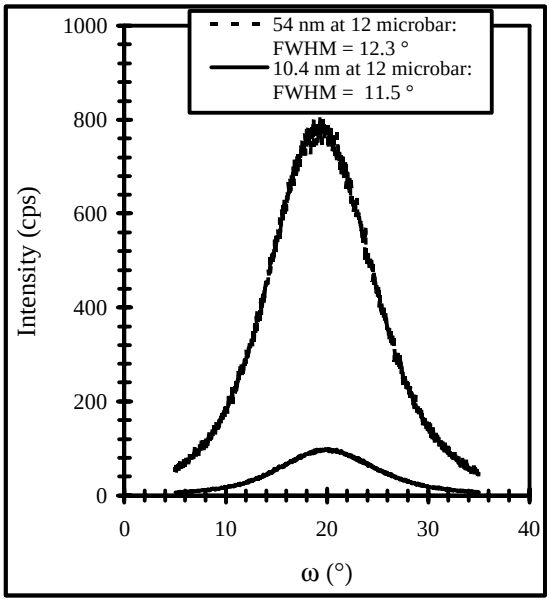

Figure 4.3C: *XRD Rocking curves of (111) crystal orientation of Pt thin films.*

An overview of the peak analyses is shown in Table 4.3. For a good interpretation of the tabulated values, it should be noted that generally the peak width is inversely proportional to the grain size and that the scattering sensitivity of X-Rays is strongly dependent on the crystallographic orientation (for Pt the sensitivity for (200) crystal orientation is 53% of the sensitivity for (111) crystal orientation).

Table 4.3: *Width and relative intensity of the measured peaks in the XRD patterns of Pt thin films shown in Figure 4.3B.*

Sample (thickness /pressure)	I (111) (cps)	FWHM (111) (º)	I (200) (cps)	FWHM (200) (º)	I (200) / I (111)
10.4 nm / 12 μbar	100	0.90	0.8	1.3	1 %
54 nm / 12 μbar	960	0.40	2.1	1.1	0.2 %
38 nm / 36 μbar	113	0.55	10.4	0.65	9 %

Now, concerning the growth of Pt thin films several conclusions can be made:

- The low angle XRD patterns show that the surface roughness at 12 microbar is at most only slightly dependent on layer thickness, but that it drastically increases by raising the deposition pressure to 36 microbar.
- The high angle XRD patterns show that all Pt films have a (111) preferred grain orientation. The distribution of the (111) grain orientation is independent of the layer thickness within the range of study (see Figure 4.3C).
- (200) texture is present in films deposited at 12 μbar, but the ratio of (200) and (111) grains is in the order of a few percents or less and decreases with increasing thickness.
- By raising the deposition pressure to 36 μbar the (111) peak position is shifted to higher angle and the amount of (200) grains increases by one order of magnitude (corrected for orientation sensitivity the ratio of (200) and (111) grains is around 20%). Shifts in peak position are often due to the presence of stress in the layer, so probably the stress in the layer is different for both deposition pressures.

Though the deposition pressures in both studies are different, we may conclude that some of the observed trends are similar to those observed by Shimatsu *et al* [4.24].
A closer look to Figure 4.3B reveals some less evident features of the growth at 12 μbar. The (111) peak of the 10 nm layer is slightly shifted to a higher angle compared to the (111) peak of the 54 nm layer. Moreover, at least after the growth of 10 nm, the amount of (200) grains does not seem to increase proportionally to layer thickness. Apparently, the growth is not homogenous through the whole layer

and the initial stage of the thin film growth is different. Note that this effect is also observed in the (111) peak of the 54 nm layer. The shoulder to the high angle side clearly indicates an inhomogeneous growth. Indeed, by etching the 54 nm layer by ion beam etching to 18 nm this could be revealed. The high angle XRD pattern of the thinned layer showed a shift in (111) peak position and an unchanged intensity of the (200) peak (not shown here). It should be mentioned that the surface roughness and FWHM of the (111) rocking curve remained unchanged. Therefore, it can be concluded with confidence that an initial layer of approximately 5-10 nm with inferior crystal quality exists. On top of this layer the growth has a purely (111) orientation.

4.3.2 XRD analysis of $Co_{50}Ni_{50}$ thin films

The XRD analysis of some $Co_{50}Ni_{50}$ thin films is shown in Figure 4.4A-B. The low angle XRD patterns show that the surface roughness of $Co_{50}Ni_{50}$ thin films is modest and only slightly dependent on deposition pressure and layer thickness. The high angle XRD patterns show a weak fcc (111) texture with also fcc (200) oriented grains present.

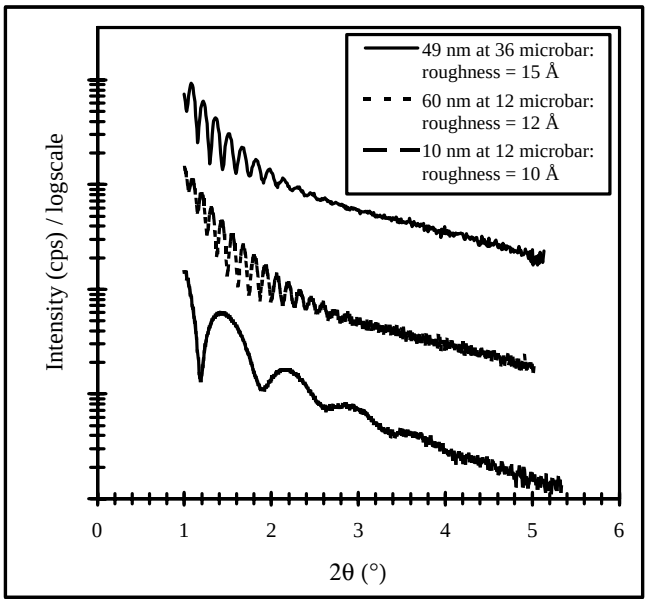

Figure 4.4A: *Low angle XRD patterns of single $Co_{50}Ni_{50}$ thin films deposited on thermally oxidized Si(100) at 12 and 36 mbar. The order of the entries in the legend corresponds to the order of the curves. The surface roughness and layer thickness have been determined from simulations with GIXA [4.23].*

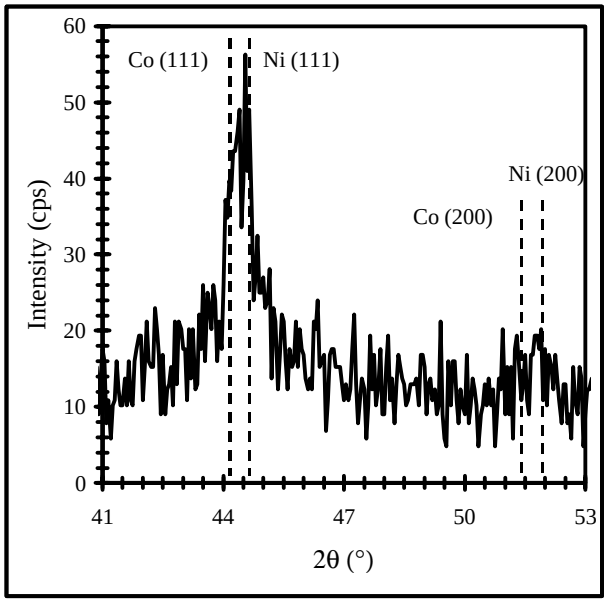

Figure 4.4B: *High angle XRD pattern of a 46 nm $Co_{50}Ni_{50}$ thin film deposited on thermally oxidized Si(100) at 12 mbar.*

4.4 Texture in sputtered $Co_{50}Ni_{50}$/Pt multilayers

In the previous section good texture in Pt thin films and bad texture in $Co_{50}Ni_{50}$ thin films has been observed. Now, we aim to obtain information about the growth of both elements in a multilayer and its relation with the deposition conditions.

4.4.1 XRD analysis of $Co_{50}Ni_{50}$/Pt multilayers

Figure 4.5A shows a typical high angle XRD pattern of a $Co_{50}Ni_{50}$/Pt multilayer deposited at 12 μbar. Two peaks are observed. The largest peak is present in between the Pt (111) and $Co_{50}Ni_{50}$ (111) lattice positions and indicates a good (111) texture in both the Pt and $Co_{50}Ni_{50}$ layer. Since (111) texture was absent in single $Co_{50}Ni_{50}$ thin films, it may be concluded that the Pt promotes (111) texture in the $Co_{50}Ni_{50}$ layer. The origin of the 'multilayer' peak is the artificial layer modulation and its position corresponds to the average lattice spacing in the multilayer [4.25-27]. The FWHM of the rocking curve is approximately 14 º (see Figure 4.5B). This value is close to the FWHM of the (111) rocking curve of single Pt thin films. Apparently, the direction of the layer modulation is strongly correlated with the crystallographic orientation.

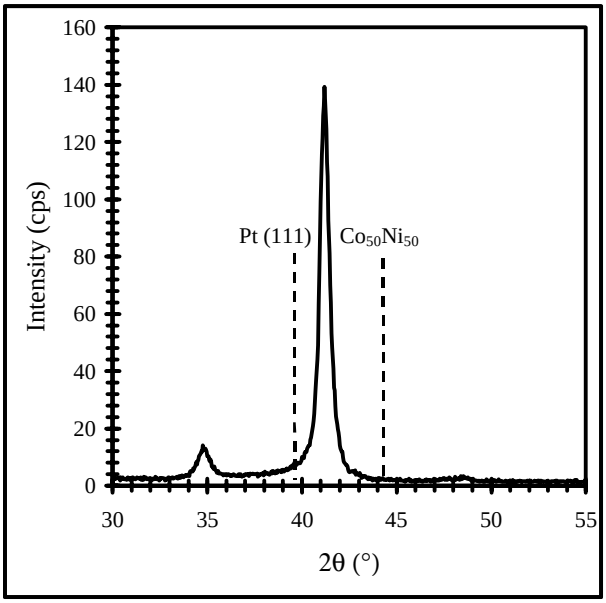

Figure 4.5A: *High angle XRD pattern of a Pt (0.8 nm)/{$Co_{50}Ni_{50}$ (0.7 nm)/Pt (0.8 nm)} x 26 multilayer.*

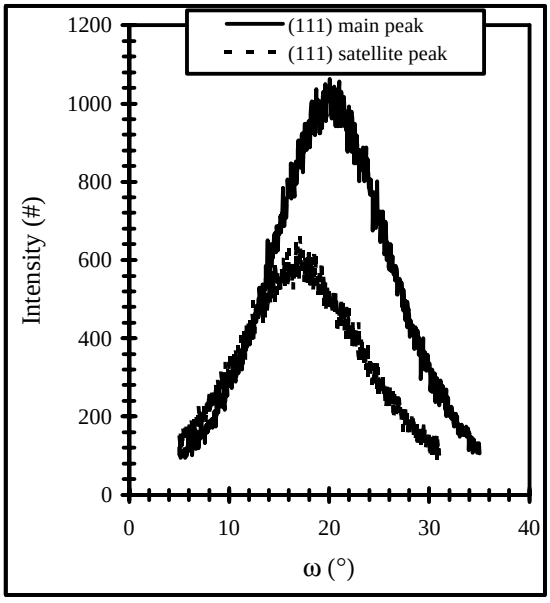

Figure 4.5B: *XRD Rocking curves of the (111) multilayer and satellite peak of a Pt (0.8 nm)/{$Co_{50}Ni_{50}$ (0.7 nm)/Pt (0.8 nm)} x 26 multilayer.*

At the left side of the 'main' peak a much smaller satellite peak is observed in the high angle XRD pattern. With Bragg's law the bilayer thickness can be calculated from the distance between this satellite peak and the main peak. The relative intensity of the satellite peak is amongst others dependent on the uncorrelated interface roughness, i.e. the variation in the layer thicknesses, and the strain and thickness ratio of the individual layers [4.27]. Note that the lateral scale of this interface roughness may principally differ from the lateral scale of surface roughness determined with low angle XRD. The former concerns intragranular roughness with atomic dimensions while the latter concerns intergranular roughness of tens of nanometers or more. Moreover, surface roughness is suspected to be developed mainly at the initial stages of the growth, while atomic roughness will be formed throughout the whole thin film.
The satellite peak itself gives similar information as the main peak, as is shown by the rocking curve (Figure 4.5B). Due the dominant presence of the (artificial) interference peaks, the true (perpendicular) lattice spacings of the individual layers can not be measured by X-Ray Diffraction. This means that the intralayer strain should be derived in a different way. In fact, off-axis XRD measurements can be used to determine the lattice spacings in the direction of other (111) planes. In the fcc lattice (111) planes are at an angle of 70.5º with respect to eachother. Since $Co_{50}Ni_{50}$/Pt multilayers grow with a strong (111) texture perpendicular to the substrate plane, another (111) plane can be found at a psi-angle of 70.5º in the diffractometer. Figure 4.6 shows an off-axis measurement at another (111) plane.

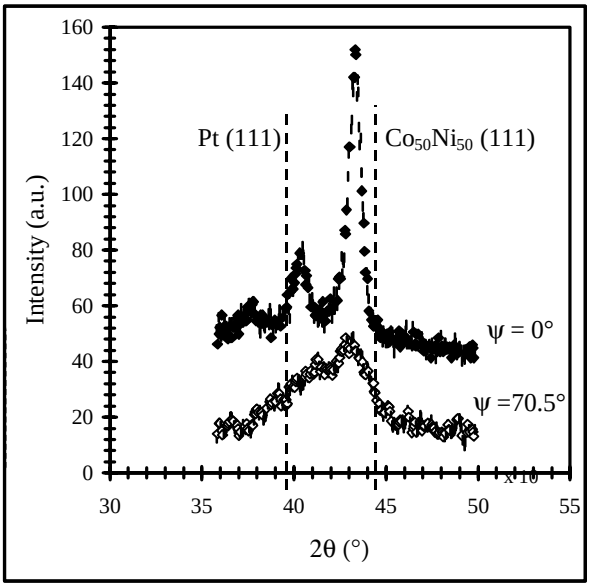

Figure 4.6: *High angle XRD patterns at two different psi-angles for a (Pt (0.7 nm)/{$Co_{50}Ni_{50}$ (2.5 nm)/Pt (0.7 nm)} x 26 multilayer (from series ws12).*

Though the signal-to-noise ratio of this measurement is relatively bad due to the absence of texturing in the plane of the substrate, a broad diffraction peak can be observed in between the bulk positions of Pt and $Co_{50}Ni_{50}$. Moreover, this broad peak seems to have two contributions: a broad Pt peak and a smaller $Co_{50}Ni_{50}$ peak. From the peak positions can be concluded that in the direction of measurement the Pt lattice is compressed and the $Co_{50}Ni_{50}$ lattice is expanded.

4.4.2 Texture at different deposition conditions

Now that a good understanding of the growth and XRD analysis of $Co_{50}Ni_{50}$/Pt multilayers has been obtained, the dependence of texture on deposition conditions can be discussed. Figure 4.7A shows the low angle XRD patterns of three $Co_{50}Ni_{50}$/Pt multilayers deposited at different pressures. For multilayers deposited at 6 and 12 μbar, the first order Bragg peak due to the layer modulation is clearly present. The surface roughness follows the trend observed for Pt thin films in Figure 4.3A. Since the simulation of multilayers is very difficult, no value of the roughness is given here.
Figure 4.7B+C show high angle XRD patterns of two sets of multilayers selected from series p6, ws12, p12 and p36. Several peak characteristics are shown in Table 4.4.

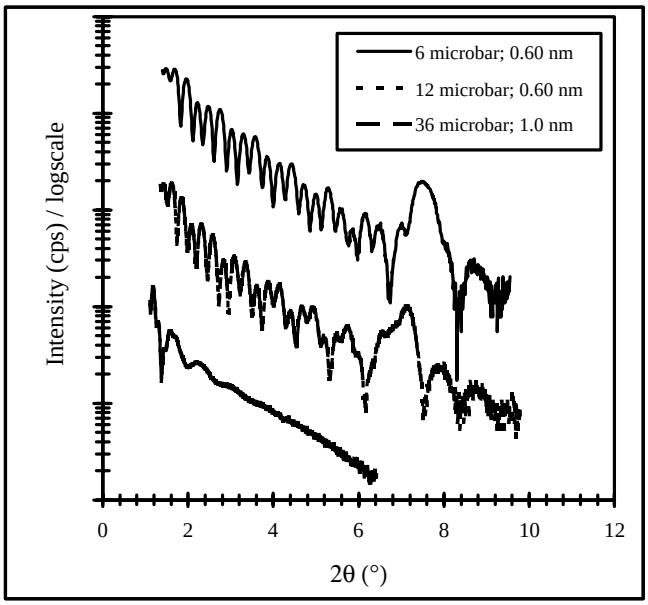

Figure 4.7A: *Low angle XRD patterns of $Co_{50}Ni_{50}$/Pt multilayers deposited at different pressure (from series p6, p12 and p36; t_{CoNi} is indicated in the legend).*

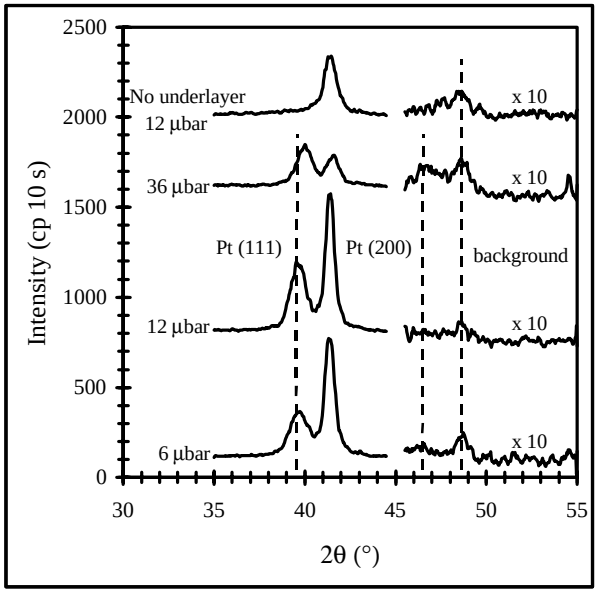

Figure 4.7B: *High angle XRD patterns of $Co_{50}Ni_{50}$/Pt multilayers with t_{CoNi} = 6 Å (from series p6, ws12, p12 and p36). The origin of the peaks is indicated.*

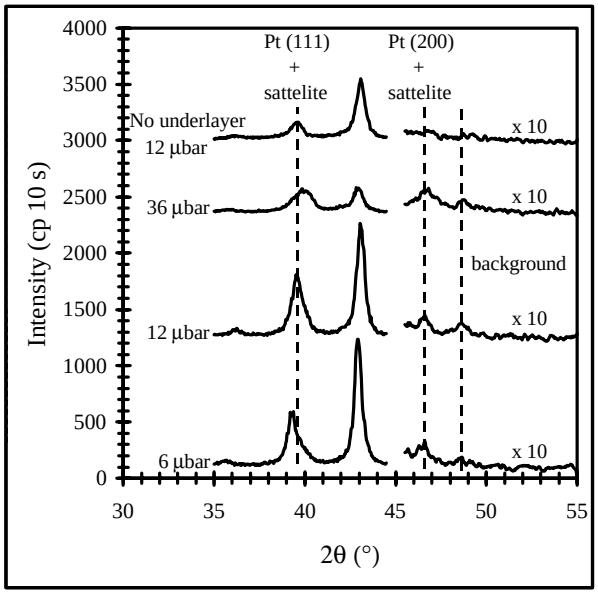

Figure 4.7C: *High angle XRD patterns of $Co_{50}Ni_{50}$/Pt multilayers with t_{CoNi} = 20 Å (from series p6, ws12, p12 and p36) The origin of the peaks is indicated.*

Table 4.4: *Width and absolute intensity of the measured peaks in the XRD patterns of $Co_{50}Ni_{50}$/Pt multilayers shown in Figure 4.7B+C.*

Sample (series/ t_{CoNi} (Å))	I [Pt (111)] (cps)	I [ML (111)] (cps)	I [ML (111)] / I [Pt (111)]	FWHM Pt (111) (º)	FWHM ML (111) (º)
p6 / 6	24	65	2.7	1.2	0.6
ws12 / 6	-	32	-	-	0.8
p12 / 6	37	75	2.0	0.9	0.6
p36 / 6	12	17	1.4	1.0	0.9
p6 / 20	24*	112	4.7	?*	0.4
ws12 / 20	-	51	-	-	0.6
p12 / 20	24*	98	4.1	?*	0.5
p36 / 20	18*	21	1.2	1.2*	0.5

* The peak of Pt (111) coincides with the first order satellite peak. The given value of the intensity is an estimation of the true Pt (111) contribution to the measured peak. The FWHM can not be determined.

The most important observations are:

- The diffraction patterns of multilayers deposited on Pt underlayers at 6 and 12 microbar are very similar. The Pt underlayers show good (111) texture and no (200) texture is observed. The multilayers deposited on top of these underlayers also show good (111) texture. The underlayer, multilayer and sattelite peaks have approximately equal intensity. Apparently, microstructural features as the local variations in thickness (interface roughness) and strain of the individual layers are similar in both conditions.
- The texture of the Pt underlayer in multilayers deposited at 36 µbar is worse, as for single Pt thin films (see subsection 4.3.1). The Pt (111) peak of the underlayer is reduced and also the Pt (200) peak is observed. Moreover, the intensity of the multilayer peak is reduced and no sattelite peaks are present. This might point to either a simple reduction of (111) texture of the multilayers, but also the presence of larger interface roughness and/or different intralayer strain may contribute to this effect. It should be reminded that the stress/strain in single Pt thin films also changes for high deposition pressure (see subsection 4.3.1).
- The main peak in the diffraction pattern of the multilayer without underlayer is considerably smaller than that of multilayers with underlayer. Probably, the (111) texture is less due to the bad initial growth as reported for single Pt thin films (see subsection 4.3.1). This may also explain that the sattelite peaks are less sharp. Then, after several bilayers, the interface roughness and intralayer strain seems to be not much different from multilayers deposited with thick underlayer.

Concluding, the growth of $Co_{50}Ni_{50}$/Pt multilayers is strongly dependent on the deposition conditions. Large differences in both texture and interface quality have been observed. In the next sections, these results will be used for the explanation of the dependence of magnetic anisotropy on the deposition conditions.

4.5 Magnetic anisotropy and layer geometry

As was observed in the previous sections, bad initial growth causes a deteriorated texture and crystalline quality in the first nanometers of $Co_{50}Ni_{50}$/Pt thin films and multilayers. Now, the consequences of these effects on the magnetic anisotropy will be discussed. Therefore, the magnetic moment and anisotropy of all samples of multilayer series wsnb12, ws12 and p12 have been measured. Both are shown in Figure 4.8A respectively 4.8B.

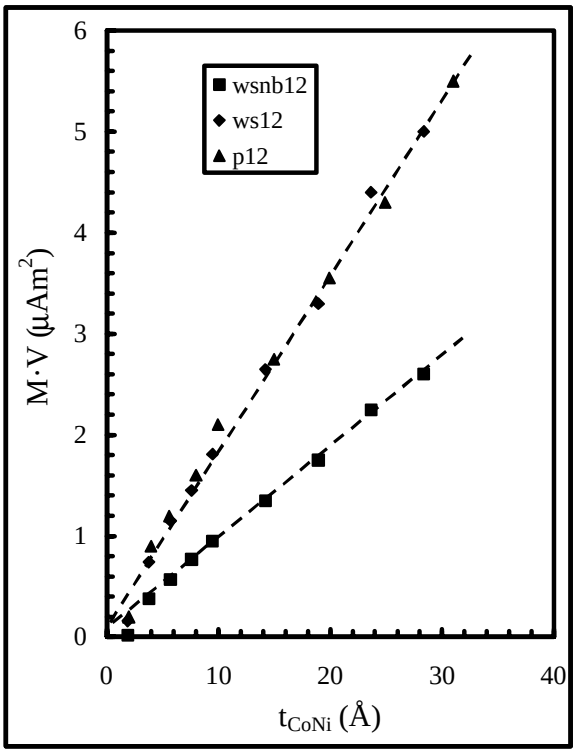

Figure 4.8A: *Magnetic moment M·V vs. t_{CoNi} for the multilayer series wsnb12, ws12 and p12.*

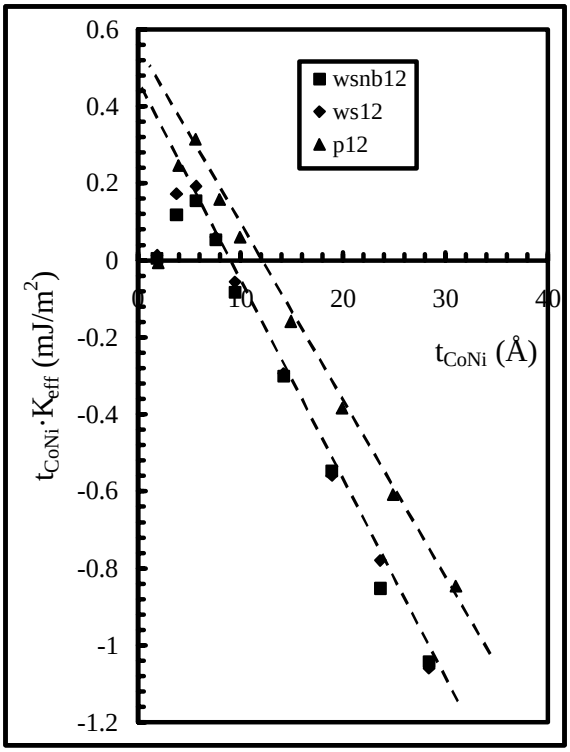

Figure 4.8B: *Effective magnetic anisotropy (expressed as) $t_{CoNi} \cdot K_{eff}$ vs. t_{CoNi} for the multilayer series wsnb12, ws12 and p12.*

Except for $t_{CoNi} < 4$ Å, the magnetic moment clearly is linear with the magnetic layer thickness for all three series. From the slope of the curves, the saturation magnetization M_s of $Co_{50}Ni_{50}$ has been determined: $M_s = (10.0 \pm 0.3) \cdot 10^2$ kA/m. Within the inaccuracy of measurement, M_s corresponds with the bulk saturation magnetization of $Co_{50}Ni_{50}$: 987 kA/m [4.28].
For all three series the magnetic anisotropy $t_{CoNi} \cdot K_{eff}$ vs. t_{CoNi} shows linear behaviour for $6 < t_{CoNi} < 30$ Å. Apparently, interface roughness is smaller than 6 Å and does not dependent on the layer geometry. Moreover, since the magnetic anisotropy is highly sensitive for crystal structure, the latter is suspected to be homogeneous over the range of linear behaviour. Note that this is an important observation, which could not be determined with X-Ray Diffraction analysis. At fixed t_{CoNi}, multilayers deposited on top of a Pt underlayer clearly have larger contributions of perpendicular anisotropy. From a linear fit, the interface and volume contributions to the magnetic anisotropy have been determined and are shown in Table 4.5.

Table 4.5: *Contributions to the magnetic anisotropy of the three series of (Pt underlayer) / {$Co_{50}Ni_{50}$ (t_{CoNi})/Pt (t_{Pt})} x N multilayers deposited at 12 mbar, with: K_i = interface anisotropy; K_v = volume anisotropy; K_d = shape or demagnetization anisotropy.*

Layer geometry (series nr)	K_i (mJ/m^2)	K_v (kJ/m^3)	K_v- K_d (kJ/m^3)
9 bilayers (wsnb12)	0.22 ± 0.01	-(5.3 ± 0.2) · 10^2	+(8 ± 2) · 10
17 bilayers (ws12)	0.24 ± 0.01	-(5.4 ± 0.2) · 10^2	+(7 ± 2) · 10
17 bilayers with underlayer (p12)	0.26 ± 0.01	-(4.5 ± 0.2) · 10^2	+(16 ± 2) · 10

Multilayers deposited on top of a 10 nm Pt underlayer have the largest interface anisotropy (in fact, it would be more correct to speak of the *average* interface anisotropy). Obviously, the presence of bad 'initial' bilayers with reduced (111) texture explains the lower interface anisotropy for multilayers deposited without underlayer. This also explains the difference in average interface anisotropy between the 9 bilayers series and 17 bilayers series.

Interestingly, the volume anisotropy is equal for both multilayers deposited without underlayer, but is considerably smaller (i.e. less negative) for multilayers deposited on top of a Pt underlayer. Considering the volume anisotropy, in general three contributions are important: shape or demagnetization anisotropy K_d , crystal anisotropy $K_{crystal}$ and magneto-elastic or strain-induced anisotropy K_{strain} (see Chapter 2). K_d can be calculated from the saturation magnetisation, i.e. 987 kA/m, which results in K_d = -610 kJ/m^3. After correction of K_v for K_d still a positive, i.e. perpendicular, contribution to the magnetic anisotropy remains. The values of K_v- K_d are also shown in Table 4.5. The (bulk) crystal anisotropies, K_1 and K_2, of $Co_{50}Ni_{50}$ alloy are –10.8 and –4.0 kJ/m^3 respectively [4.28]. Clearly, these values are much too small to explain the remaining anisotropy. Apparently, magneto-elastic anisotropy is contributing to the perpendicular anisotropy. The direction of magneto-elastic anisotropy is determined by the signs of the lattice strain and magnetostriction constant. As shown in subsection 4.4.1, the $Co_{50}Ni_{50}$ lattice is expanded in the plane of the film (and therefore compressed perpendicular to the film). Moreover, the magnetostriction constant is negative for $Co_{50}Ni_{50}$ (λ_{111}=-35*10^6 [4.29]). The induced magneto-elastic anisotropy is then indeed in the perpendicular direction. Just as for interface anisotropy, the magneto-elastic effect seems larger for multilayers deposited on top of a Pt underlayer. Because the magneto-elastic anisotropy increases with (111) texture, this can be well understood.

Herewith, all contributions to the magnetic anisotropy have been identified and quantified. The most important conclusion is that, due its strong relation with interface and magneto-elastic anisotropy, the degree of (111) texture plays an important role in the measured magnetic anisotropy of $Co_{50}Ni_{50}$/Pt multilayers.

4.6 Magnetic anisotropy and deposition pressure

Next, on the basis of multilayer series p6, p12 and p36 the role of the deposition pressure in the magnetic anisotropy of $Co_{50}Ni_{50}$/Pt multilayers will be discussed. All multilayers of these series have been deposited on top of a 10 nm Pt underlayer so initial growth effects can be ruled out. The magnetic moment and anisotropy vs. t_{CoNi} are shown in Figure 4.9A and 4.9B respectively.
Also for these series the measured magnetic moment is highly linear with t_{CoNi}. The magnetic anisotropy vs. t_{CoNi}, however, shows important different behaviour. Though the magnetic anisotropy of multilayers deposited at 6μbar exhibits the expected linear behaviour, the magnetic anisotropy of multilayers deposited at 36 μbar seems non-linear, which is most visible for large t_{CoNi}. As in the previous section the volume and interface contributions to the magnetic anisotropy have been determined from a linear fit and are shown in Table 4.6. For the 36 μbar linear fits have been made at small and large t_{CoNi}.

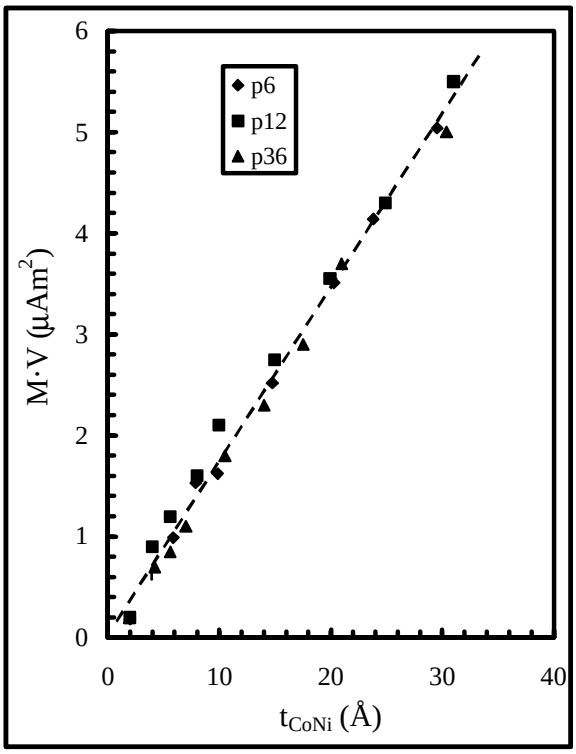

Figure 4.9A: *Magnetic moment M·V vs. t_{CoNi} for the multilayer series p6, p12 and p36.*

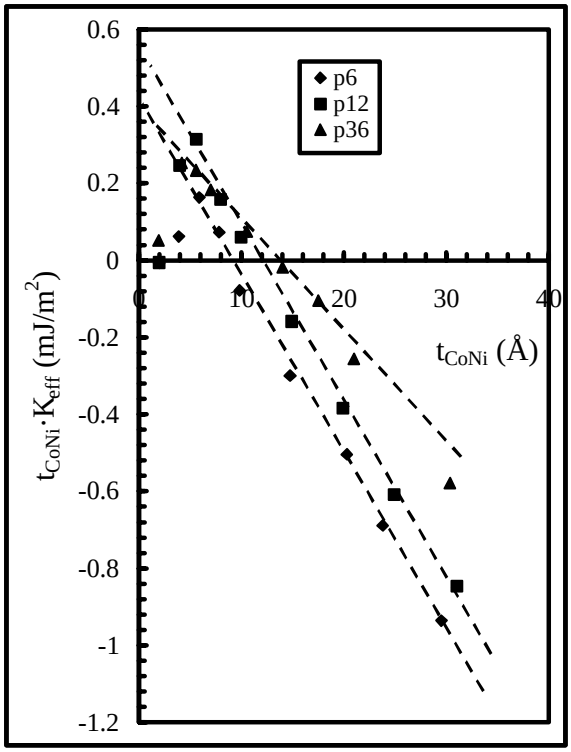

Figure 4.9B: *Effective magnetic anisotropy (expressed as) $t_{CoNi} \cdot K_{eff}$ vs. t_{CoNi} for the multilayer series p6, p12 and p36.*

Compared to multilayers deposited at intermediate pressure, the interface anisotropy decreases for lower deposition pressure. This may well be explained considering the more energetic bombardment of the multilayer during growth at lower pressure (see Table 4.1 and [4.20]). On the other hand, the magneto-elastic anisotropy, which is assumed to be responsible for the remaining contribution of perpendicular anisotropy (see section 4.5), is unchanged. This is in agreement with the X-Ray Diffraction analysis in section 4.4 where no differences between the crystallographic structure of both series could be revealed.

Table 4.6: *Contributions to the magnetic anisotropy of the three series of Pt underlayer / {$Co_{50}Ni_{50}$ (t_{CoNi})/Pt (t_{Pt})} x N multilayers deposited at different pressure, with: K_i = interface anisotropy; K_v = volume anisotropy; K_d = shape or demagnetization anisotropy.*

Deposition pressure (series nr)		**K_i (mJ/m^2)**	**K_v (kJ/m^3)**	**K_v- K_d (kJ/m^3)**
6 μbar (p6)		0.21 ± 0.01	$-(4.6 \pm 0.2) \cdot 10^2$	$+(15 \pm 2) \cdot 10$
12 μbar (p12)		0.26 ± 0.01	$-(4.5 \pm 0.2) \cdot 10^2$	$+(16 \pm 2) \cdot 10$
36 μbar* (p36)	t_{CoNi} = 6 Å	0.19± 0.01	$-(2.9 \pm 0.2) \cdot 10^2$	$+(32 \pm 2) \cdot 10$
	t_{CoNi} = 30 Å	0.29± 0.01	$-(3.6 \pm 0.2) \cdot 10^2$	$+(25 \pm 2) \cdot 10$

*For the series deposited at 36 μbar $t_{CoNi} \cdot K_{eff}$ vs. t_{CoNi} seems slightly non-linear. Therefore, linear approximations have been made in a region of small and large t_{CoNi}.

For multilayers deposited at 36 μbar the interface anisotropy seems to increase with t_{CoNi}. A likely explanation is the presence of significant interface roughness due to the low deposition energies of the sputtered atoms (see Table 4.1). Its consequence is that the effective interface area increases with t_{CoNi} and that the measured interface anisotropy should be corrected for this area. Unfortunately, this is not possible. Assuming that for t_{CoNi} = 30 Å the measured interface anisotropy is 'saturated', it may be concluded that for pressures larger than 12 μbar the true interface anisotropy still increases with pressure. Apparently, this effect dominates the expected reduction of interface anisotropy due to the presence of (200) grains. Note that the interface roughness is (at least) around the thickness of the Pt layer, i.e. 8 Å. Therefore the interface anisotropy should also be corrected for the effective Pt coverage, which would give an even larger value.

The interface roughness may also explain the apparent decrease of magneto-elastic anisotropy for larger t_{CoNi}. Due to the large interface roughness and thin Pt layer, the growth of the $Co_{50}Ni_{50}$ layer may be inhomogeneous. Therefore, also strain effects may be inhomogeous in the $Co_{50}Ni_{50}$ layer. Quantification of these effects would be very difficult.

In collaboration with the Research Institute for Materials of the Universiy of Nijmegen the interface structure as function of deposition pressure has been further characterized with magnetization-induced second-harmonic generation (MSHG) [4.30]. With this optical measurement technique 'magnetic' and 'crystallographic' information of the structure of the interface can be obtained. A detailed description of the technique is beyond the scope of this thesis but can be found elsewhere [4.31]. To allow a quantitative analysis, single Pt (40 nm)/$Co_{50}Ni_{50}$ (3 nm)/Pt (3 nm) sandwiches have been prepared for MSHG measurements. A total of eight samples have been deposited in a pressure range 4-36 μbar. The measured magnetic and crystallographic contributions to the MSHG (m and χ_{cr} respectively) are plotted as function of deposition pressure in Figure 4.10.

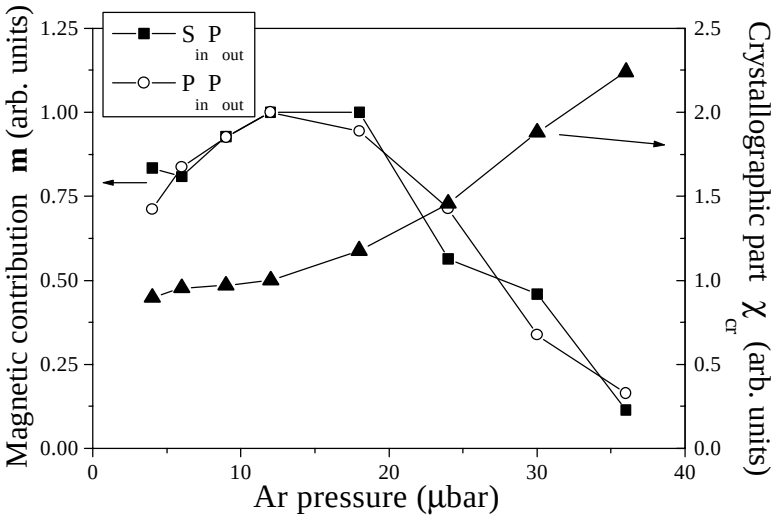

Figure 4.10: *Magnetic and crystallographic contribution to the Magnetization-induced Second-Harmonic Generation in a Pt/$Co_{50}Ni_{50}$/Pt sandwich as function of deposition pressure [4.30]. The legend indicates the polarization of incident and reflected light in the experiment.*

M shows a maximum at intermediate deposition pressure. For low pressure the relative decrease of m is comparable to the decrease of K_i , which is related to the increased interfacial mixing. For high pressure m decreases with an order of magnitude. Due to the different behaviour of magnetic spins in a rough interface, this may be indirectly caused by an increase of interface roughness [4.30]. On the other hand, the crystallographic contribution χ_{cr} monotonically increases with deposition pressure. In fact, χ_{cr} follows the same trend as the presence of (200) grains reported in subsection 4.3.1. Both are approximately constant up to 12 μbar but drastically increase for higher pressure. However, χ_{cr} is expected to be strictly proportional to the interface roughness [4.30]. Therefore, it may be concluded that indeed the interface roughness drastically increases with deposition pressure. These measurements then confirm the observations made above from Figure 4.9B.
Summarizing, the combination of the anisotropy and MSHG measurements lead to the remarkable conclusion that the true interface anisotropy (corrected for effective interface area) still increases for high pressures, despite of the formation of (200) textured grains. Since the amount of (200) grains still is only about 10 to 20 % (judged from Figure 4.7B+C and the remarks in subsection 4.3.1), this is not in contradiction with work by Lee *et al.*, who showed that the interface anisotropy is strongly dependent on crystallographic orientation [4.22].

4.7 $Co_{50}Ni_{50}$/Pt multilayer for application as patterned medium

When choosing the deposition conditions of $Co_{50}Ni_{50}$/Pt multilayers for the application as patterned medium, the requirements of large perpendicular anisotropy and strong intergranular exchange coupling should be kept in mind. In the previous sections a clear picture of the microstructure and magnetic anisotropy of $Co_{50}Ni_{50}$/Pt multilayer has been obtained. Based on this data the optimal deposition conditions can now be selected.

4.7.1 Selection of deposition conditions

Multilayers deposited at high pressure can exhibit large perpendicular anisotropy but are unfavourable due to their reduced intergranular exchange coupling, which is indicated by the void formation and large surface roughness. Note that this effect is experimentally observed as a large coercivity in the as deposited multilayer and a 'particle'-like magnetization reversal [4.15]. Clearly, the deposition pressure should be in the low pressure range. Then, optimizing for perpendicular anisotropy, the choice of a deposition pressure of 12 μbar is obvious. With several practical considerations the layer geometry is then designed. In order to allow a simple patterning process the thickness of the multilayer including any Pt underlayer should be less than approximately 30 nm (see also Chapter 3). On the other hand, from the point of view of the limited sensitivity of the magnetic characterization equipment, the magnetic volume and torque should be as high as possible. Therefore, any Pt underlayer is omitted and the Pt layer thickness is minimized to 6 Å. Finally, the $Co_{50}Ni_{50}$/Pt multilayer designed for application has the following characteristics:

- deposition pressure = 12 μbar
- bilayer = {Pt (6 Å)/ $Co_{50}Ni_{50}$ (6 Å)}
- number of bilayers = 26
- Pt 'underlayer' = 6 Å
- substrate = thermally oxidized Si

4.7.2 Magnetization reversal in the optimized $Co_{50}Ni_{50}$/Pt multilayer

Both minor and major hysteresis curves of the optimized $Co_{50}Ni_{50}$/Pt multilayer are shown in Figure 4.11.

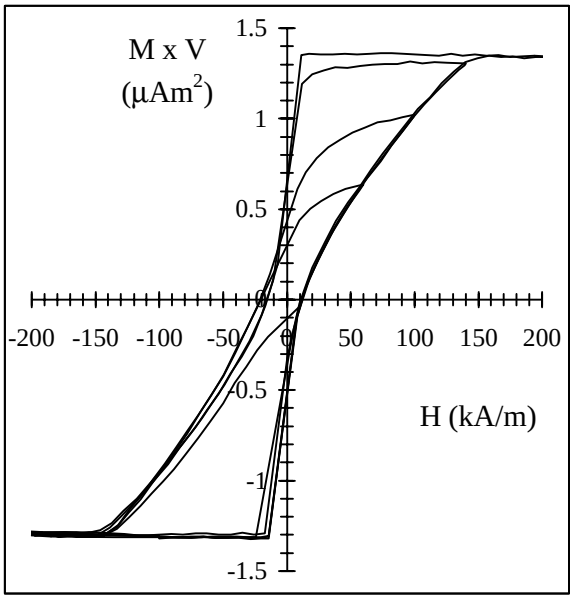

Figure 4.11: *Major and minor VSM hysteresis curves of the Pt (6 Å)/{$Co_{50}Ni_{50}$ (6 Å)/Pt (6 Å)} x 26 multilayer deposited at 12* mbar *on a thermally oxidized silicon substrate.*

The magnetization reversal is similar to that observed by Kooy *et al.* in thin plates of bariumferrite [4.32]. After saturation, the magnetization of the multilayer nucleates into a stripe domain pattern at the nucleation field H_N, in this case close to zero. With a small increase of the applied field beyond the nucleation field this stripe domain pattern becomes a demagnetized state with zero net magnetic moment. This observation means that the magnetization reversal is a dynamic process which is also observed in Figure 4.12 (see the discussion following below). Upon further increase of the applied field the reversed domains grow at the cost of the unreversed ones. Finally, saturation is reached at the saturation field H_S. This specific type of magnetization reversal is a good indication for the strong intergranular exchange coupling of the multilayer.
According to Zeper *et al.* the value of the nucleation field is determined by so-called vestigal domains [4.3]. These are small domains, which can not be saturated, and become unstable at H_S. Unfortunately, the origin of these domains remained undiscussed. The nucleation in the $Co_{50}Ni_{50}$/Pt multilayer has been observed in more detail by polar Kerr microscopy. Figure 4.12A shows a sequence of images at a constant applied field of –10 kA/m. Note that the magnetic contrast observed in the images is the intensity of the saturated state compared to the intensity of the stripe domain state. The dendretic growth of the stripe domain pattern is typical for (thick) multilayers (see also [4.33]). The normal microscopy image shows no irregularities at the site of the start of the nucleation. Apparently, inhomogeneities

smaller than the resolution of optical microscopy are responsible for the nucleation at the specific site. As shown in Figure 4.12B the position of nucleation is always the same. However, the direction of the growth of the stripe domain pattern is not reproducible but seems to be determined by statistical processes such as thermal activation. It should be noted that more than one nucleation site is present in the film. This phenomenum will be discussed in more detail in the next chapter.

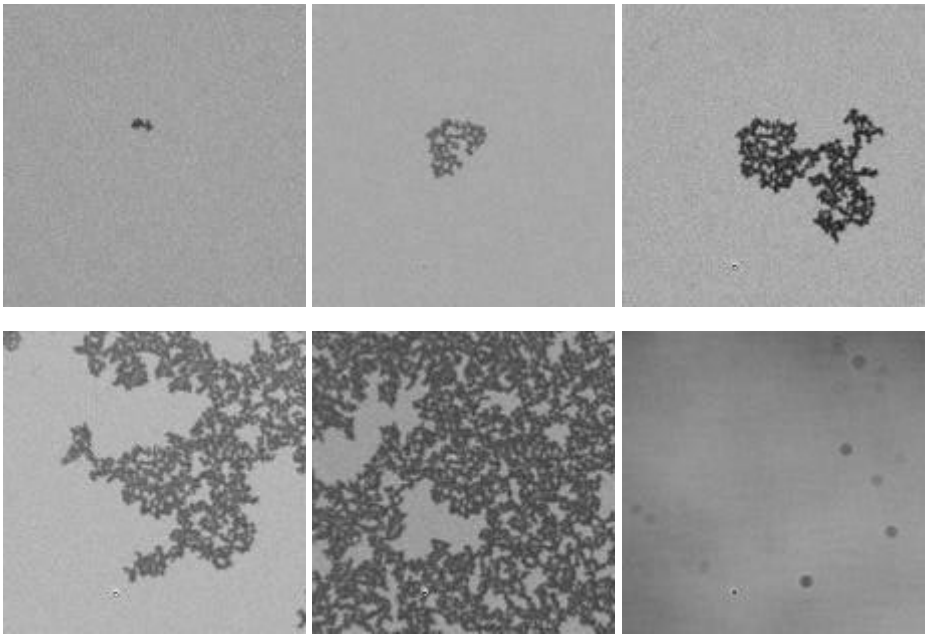

Figure 4.12A: *A sequence of Polar Kerr microscopy images taken during the nucleation of the Pt (6 Å)/{$Co_{50}Ni_{50}$ (6 Å)/Pt (6 Å)} x 26 multilayer. The applied field is near the nucleation field in the VSM hysteresis curves of Figure 4.11 and the time between the first and last images is approximately one minute. The field of view of these images is several hundred mm. The last image is the non-magnetic image. The big black spots are contaminations of dust particles in the optical path of the microscope.*

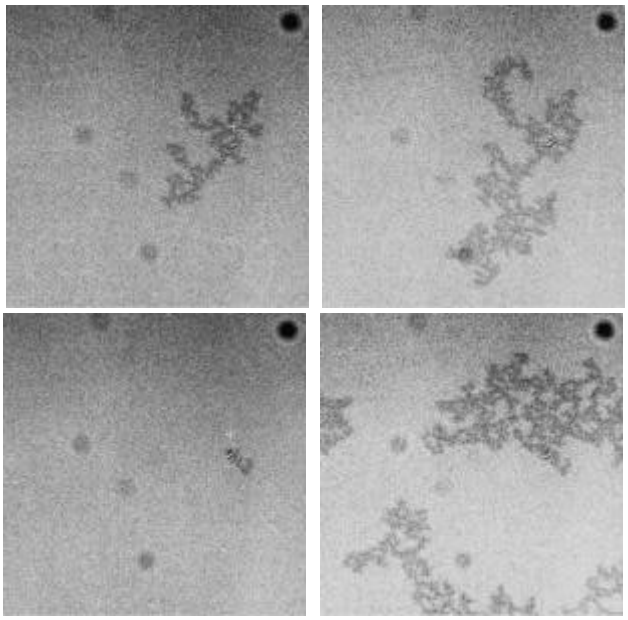

Figure 4.12B: *Two times two polar Kerr microscopy images of the same area during two different nucleations of the Pt (6 Å)/{$Co_{50}Ni_{50}$ (6 Å)/Pt (6 Å)} x 26 multilayer. The field of view is several tens* mm. *The big black spots are contaminations of dust particles inside the microscope.*

From the measured saturation magnetization and torque maximum the effective anisotropy field has been calculated for the optimized $Co_{50}Ni_{50}$/Pt multilayer, $H_{K,eff}$ = $(4.7\pm0.2)\cdot10^2$ kA/m. Clearly, a considerable coercivity may be expected for single domain dots patterned from these multilayers (see also Chapter 2). Interestingly, the value of $H_{K,eff}$ is approximately equal to the field where the rotational hysteresis loss W_R vanishes (see Figure 4.13).
Apparently, the rotational hysteresis loss curve can be used to determine $H_{K,eff}$. Since such a procedure is less affected by background signal in the torque magnetometer and thus more accurate, this method may also be usefull for the determination of $H_{K,eff}$ in submicron structures. Moreover, except for the slope up to the maximum, the W_r curve is very similar to that measured and calculated for aligned single domain elongated ferromagnetic particles [4.34,35]. W_r peaks around H_c and vanishes around $H_{K,eff}$. The slope present in the W_r curve is probably related to strong demagnetizing effects in the (perpendicular) multilayer. The rotational hysteresis loss integral R_H is 1.3, which indicates a reversal by nucleation rather than domain wall motion. However, the presence of demagnetizing effects may require a more carefull interpretation, but unfortunately a good reference is not yet available on this topic.

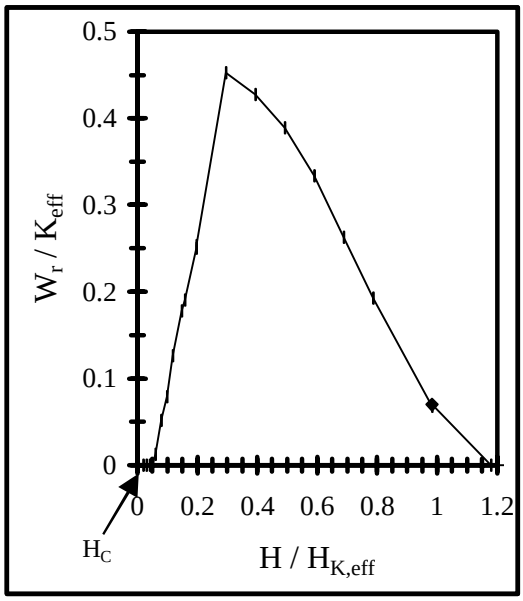

Figure 4.13: *Normalized rotational hysteresis loss W_R / K_{eff} of a Pt (6 Å)/{$Co_{50}Ni_{50}$ (6 Å)/Pt (6 Å)} x 26 multilayer vs. normalized field $H/H_{K,eff}$ (VSM hysteresis curves in Figure 4.11).*

4.8 Conclusions

In this chapter an extensive study into the relation between deposition conditions, microstructure and magnetic anisotropy of sputtered $Co_{50}Ni_{50}$/Pt multilayers was presented. The degree of texture, as determined with X-Ray Diffraction, appeared to be strongly dependent on the total layer geometry and deposition pressure. At low deposition pressure the multilayers have a low atomic roughness and a strong preferred (111) texture, while at high deposition pressure the multilayers have a large atomic roughness and an additional (200) texture is present. Moreover, if deposited without underlayer, the first several nm's of the multilayer stack have a lack of texturing, even at low deposition pressure.
The magnetic anisotropy consists of interface, shape and magneto-elastic anisotropy. The magneto-elastic anisotropy contributes to the perpendicular direction, but is only 10-20% of the shape anisotropy. Therefore, interface anisotropy is the most significant contribution to the effective perpendicular magnetic anisotropy. Thin multilayers have a lower average interface anisotropy because of the 'initial layer effects'. Besides, due to an increase in interfacial mixing by high-energy bombardment, the interface anistropy decreases towards lower deposition pressure. On the other hand, due to the increase of atomic roughness, the effective area and herewith the effective interface anisotropy decreases towards higher deposition pressure. Therefore, in order to optimize

perpendicular magnetic anisotropy, the multilayers should be as thick as possible and be deposited at an intermediate pressure.
Finally, based on these results and the constraints of the patterning process, the deposition conditions of the $Co_{50}Ni_{50}$/Pt multilayers for the research on patterned media were selected. This multilayer has 26 bilayers of $Co_{50}Ni_{50}$ (6 Å) / Pt (6 Å) and is deposited at 12 μbar. It has a large perpendicular magnetic anisotropy ($H_{K,eff}$ = $(4.7\pm0.2)\cdot10^2$ kA/m) and a strong intergranular exchange coupling. Therefore, the basic requirements for a patterned storage medium have been fullfilled.

References

[4.1] P.F. Carcia, A.D. Meinhaldt, and A. Suna, *'Perpendicular magnetic anisotropy in Pd/Co thin film layered structures'*, Appl. Phys. Lett **47** (1985) 178-180.

[4.2] P.F. Carcia, *'Perpendicular magnetic anisotropy in Pd/Co and Pt/Co thin film layered structures'*, J. Appl. Phys. **63** (1988) 5066-5073.

[4.3] W.B. Zeper, H.W. van Kesteren, B.A.J. Jacobs, J.H.M. Spruit, and P.F. Carcia, *'Hysteresis, microstructure, and magneto-optical recording in Co/Pt and Co/Pd multilayers'*, J. Appl. Phys. **70** (1991) 2264-2271.

[4.4] S. Hashimoto, A. Maesaka, K. Fujimoto, and K. Bessho, *'Magneto-optical applications of Co/Pt multilayers'*, J. Magn. Magn. Mat. **121** (1993) 471-478.

[4.5] C.J. Lin, *'Co/Pt multilayers for magneto-optical recording'* in: *'High density digital recording'*, edited by K.H.J. Busschow and G.J. Long, Kluwer (1993) 461-481.

[4.6] P.F. Carcia, *'Evolution of metal multilayers for MO recording'*, J. Magn. Soc. Jpn. **19** S1 (1995) 5-16.

[4.7] M. Mes, J.C. Lodder, T. Takahata, I. Moritani, and N. Imamura, *'Evaporated CoNi/Pt multilayers for magneto-optical recording'*, J. Magn. Soc. Jpn. **15** S1 (1993) 44 **-???** .

[4.8] S. Hashimoto, *'Adding elements to the Co layer in Co/Pt multilayers'*, J. Appl. Phys. **75** (1993) 438-441.

[4.9] R. Krishnan, H. Lassri, M. Seddat, M. Porte, and M. Tessier, *'Magnetic properties of $Co_x Ni_{1-x}$/Pt multilayers'*, Appl. Phys. Lett. **64** (1994) 2312-2314.

[4.10] Q. Meng, W.P. van Drent, J.C. Lodder, and Th.J.A. Popma, *'Curie temperature dependence of magnetic properties of CoNi/Pt multilayer films'*, J. Magn. Magn. Mat. **156** (1996) 296-298.

[4.11] J.G. Ha, K. Kyuno, and R. Yamamoto, *'Perpendicular magnetic anisotropy and magneto-optical properties of $(Co_{1-x}Ni_x)$/Pd multilayers'*, IEEE Trans. Magn. **33** (1997) 1049-1051.

[4.12] A.S. Penfold, *'Magnetron sputtering'* in: *'Handbook of thin film process technology'*, edited by D.A. Glocker and S.I. Shah, Institute of Physics Publishing (1995) A3.2:10.

[4.13] W.P. van Drent, *'CoNi/Pt multilayers for magneto-optical recording'*, Ph.D. thesis, Universiteit Twente, The Netherlands (1995).

[4.14] R.E. Somekh, *'The thermalization of energetic atoms during the sputtering process'*, J. Vac. Sci. Technol. A **2** (1984) 1285-1291.

[4.15] M.D. Bijker, D.M. Donnet, and J.C. Lodder, *'The effects of sputter pressure on the microstructure of CoNi/Pt multilayers'*, J. Magn. Soc. Jpn. **20** S1 (1996) 407-410.

[4.16] N. Sato, *'Crystallographic structure and magnetism of Co-Pd and Co-Pt films with an artificially layered structure'*, J. Appl. Phys. **64** (1988) 6424-6433.

[4.17] Z.G. Li, P.F. Carcia, and Y. Cheng, *'Co thickness dependence of the microstructure of Pt/Co multilayers'*, J. Appl. Phys. **73** (1993) 2433-2437.

[4.18] B. Zhang, K.M. Krishnan, and R.F.C. Farrow, *'Crystallography of Co/Pt multilayers and nanostructures'*, Ultramicroscopy **51** (1993) 298-305.

[4.19] G.A. Bertero, R. Sinclair, C.H. Park, and Z.X. Shen, *'Interface structure and perpendicular magnetic anisotropy in Pt/Co multilayers'*, J. Appl. Phys. **77** (1995) 3953-3959.

[4.20] P.F. Carcia, S.I. Shah, and W.B. Zeper, *'Effect of energetic bombardment on the magnetic coercivity of sputtered Pt/Co thin film multilayers'*, Appl. Phys. Lett. **56** (1990) 2345-2347.

[4.21] J.H. Kim, and S.C. Shin, *'Interface roughness effects on the surface anisotropy in Co/Pt multilayer films'*, J. Appl. Phys. **80** (1996) 3121-3123.

[4.22] C.H. Lee, R.F.C. Farrow, C.J. Lin, E.E. Marinero, and C.J. Chien, *'Molecular-beam-epitaxial growth and magnetic properties of Co-Pt superlattices oriented along the [001], [110], and [111] axes of Pt'*, Phys. Rev. B **42** (1990) 11384-11387.

[4.23] The Glancing Incidence X-ray Analysis program is commercial software from Philips Analytical B.V., Almelo, The Netherlands.

[4.24] T. Shimatsu, R.H. Mollema, D. Monsma, E.G. Keim, and J.C. Lodder, *'Metal bonding during sputter film deposition'*, J. Vac. Sci. Technol. A **16** (1998) 2125-2131.

[4.25] M.R. Khan, C.S.L. Chun, G.P. Felcher, M. Grimsditch, A. Kueny, C.M. Falco, and I.K. Schuller, *'Structural, elastic, and transport anomalies in molybdenum/nickel superlattices'*, Phys. Rev. B **27** (1983) 7186-7193.

[4.26] H. Vanderstraeten, *'Characterization of structural disorder in multilayers and superlattices using X-ray Diffraction'*, Ph.D. thesis, Katholieke Universiteit Leuven, Belgium (1991).

[4.27] B. Liebemann, *'Röntgenographische analyse des schichtwachstums von gesputterten Co- und Pt-einzelschichten, sowie Co/Pt-viellagenschichten'*, Ph.D. thesis, Friedrich-Schiller-Universität Jena, Germany (1994).

[4.28] R.M. Bozorth, *'Ferromagnetism'*, Princeton (1951).

[4.29] M. Yamamoto, and T. Nakamichi, *'Magnetostriction constants of Nickel-Copper and Nickel-Cobalt alloys'*, J. Phys. Soc. Japan **2** (1958) 228-229.

[4.30] A. Kirilyuk, Th. Rasing, M.A.M. Haast, and J.C. Lodder, *'Probing structure and magnetism of CoNi/Pt interfaces by nonlinear magneto-optics'*, Appl. Phys. Lett. **72** (1998) 2331-2333.

[4.31] Th. Rasing, *'Nonlinear magneto-optics: a novel probe for magnetic interfaces'*, J. Magn. Soc. Jpn **22** S2 (1998) 1-5.

[4.32] C. Kooy and U. Enz, *'Experimental and theoretical study of the domain configuration in thin layers of $BaFe_{12}O_{19}$'*, Philips Res. Rep. **15** (1960) 7-29.

[4.33] J.N. Chapman, J. Rose, I.S. Weir, I.S. Molchanov, and D.M. Titterington, *'The direct observation of magnetisation reversal in films of interest for high density information storage'*, J. Magn. Soc. Jpn. **22** S2 (1998) 15-20.

[4.34] I.S. Jacobs and F.E. Luborsky, *'Magnetic anisotropy and rotational hysteresis in elongated fine-particle magnets'*, J. Appl. Phys. **28** (1957) 467-473.

[4.35] S. Shtrikman and D. Treves, *'The coercive force and rotational hysteresis of elongated ferromagnetic particles'*, J. De Phys. et Radium **20** (1959) 286-289.

Chapter 5

Magnetization reversal in patterned $Co_{50}Ni_{50}$/Pt multilayers

The magnetization reversal in $Co_{50}Ni_{50}$/Pt multilayer dots has been studied. The as deposited multilayer has large perpendicular anisotropy and strong intergranular exchange coupling. Dots with sizes in the range of 60 nm to 215 mm have been prepared. Different type of characterization tools have been developed and/or applied to measure the most important magnetic properties, such as coercivity, demagnetized domain state, and effective anisotropy field.

5.1 Introduction

The patterning technology based on laser interference lithography (see Chapter 3) gives the unique possibility to prepare high-quality large-area samples of non-interacting single domain dots. Although our principal goal is the preparation of a patterned medium for discrete magnetic recording, such samples also allow a verification of the theoretical models of magnetization reversal (as discussed in Chapter 2). In this chapter results on both subjects will be presented for dots patterned from a $Co_{50}Ni_{50}$/Pt multilayer. For all studies quasi-identical multilayers with large perpendicular magnetic anisotropy and strong intergranular exchange coupling have been used. The details of their deposition conditions and magnetic properties have been discussed in Chapter 4. With respect to the topic of this chapter, the observation that the magnetization reversal of $Co_{50}Ni_{50}$/Pt multilayers is dominated by the presence of some sort of inhomogeneities, defined here as (magnetic) defect, is most important (see section 4.7). The origin and nature of these defects is unknown so far, but their density is very low, i.e. in the order of $10/mm^2$ at most. In patterned multilayers the defects may therefore be isolated and the anisotropy field may increasingly determine the mechanism of magnetization reversal. However, for dots larger than approximately 20 μm broad distributions of low nucleation field are observed. Apparently, magnetic defects still play a dominant role in the magnetization reversal. To study these defects in detail the work on patterned $Co_{50}Ni_{50}$/Pt multilayers has been expanded with series of micron-sized dots. In particular it is aimed to reveal the origin and position of the defects. The results on this work will be presented in section 5.3. Then, in section 5.4, the results on the magnetic characterization of submicron, defect-free dots will be discussed.

5.2 Patterning process and stability of $Co_{50}Ni_{50}$/Pt multilayer

Since the laser interference lithography has extensively been described in Chapter 3, only the preparation of micron-sized dots is discussed here. Moreover, the stability and reproducibility of the $Co_{50}Ni_{50}$/Pt multilayer is confirmed.

5.2.1 Preparation of micron-sized dots

The preparation of the micron-sized dots is straightforward, so only some relevant comments will be made. The square dots have been prepared by standard optical lithography with Shipley 1800 photoresist followed by pattern transfer with ion beam etching. The total area of the 2D arrays is 1x1 cm^2. The dot size after patterning, defined as the (approximate) length of the dot edge, generally deviates from the designed dot size and can vary up to 10% over the whole area. The true average dot size is therefore determined with an optical microscope. Moreover, it should be noted that for dots designed with a size of only several μm's a strong rounding effect is observed. Throughout the whole chapter the true average dot size and periodicity of any sample will be named as Size/Period. The unit of length is μm resp. nm for sections 5.2 and 5.3 respectively 5.4. So here 50/100 dots have a dot edge of 50 μm and a period of 100 μm.
All samples were investigated by Vibrating Sample Magnetometry (VSM) for macroscopic magnetic characterization and by polar Kerr Microscopy for observing the nucleation field H_N of individual dots. H_N is defined as the reverse field at which the saturated state splits up in domains. At nucleation the contrast in the Kerr image changes. By studying the nucleation of a large area of dots a nucleation field distribution can be constructed.

5.2.2 Stability and reproducibility of $Co_{50}Ni_{50}$/Pt multilayer

It may be argued whether $Co_{50}Ni_{50}$/Pt multilayers are suitable for patterning. The individual layer thicknesses are only 6 Å and especially intermixing of the layers during bake-out of the photoresist may be feared. In this respect the observations by Jamet *et al.* on the damage induced by the patterning process in Au/Co/Au sandwiches are important [5.1]. They reported a considerable increase in strong domain-wall-pinning sites for the processed, but unetched, sandwich. Since in our case the baking temperature of the resist is only maximum 120 ºC, no annealing effects are expected but still small structural and magnetic changes may occur. To detect modifications in the multilayer structure during the patterning process, both structural and magnetic characterization tools can be used:

- Domain-wall pinning sites will affect the sharp nucleation in the hysteresis.
- An initial magnetization (IM) curve easily reveals deteriorations of the smooth domain wall movement. Note that the IM curve directly can be compared with

the hysteresis curve of the as deposited multilayer because the latter nucleates around zero field into a demagnetized state.

- The perpendicular magnetic anisotropy is strongly dependent on the interface structure and therefore will be affected by intermixing effects. When comparing different samples, the strong dependence of the magnetic torque on the individual Pt and $Co_{50}Ni_{50}$ layer thicknesses should be taken into account (see Chapter 4 and section 5.3.3). For instance, a 10% decrease or increase in $Co_{50}Ni_{50}$ thickness causes a 20% increase respectively decrease in effective anisotropy field.
- The multilayer and satellite peaks in the high angle XRD pattern are also very sensitive to intermixing effects. However, it should be mentioned that the absolute height of the multilayer peak is not well reproduced for dot samples prepared with intervals of several months. From rocking curves it was confirmed that the variation in peak height is not correlated with grain orientation. Though the peak height surely strongly depends on the exact Pt thickness, the full origin of this effect is still unknown.

Figure 5.1 shows the VSM hysteresis/initial-magnetization curves and the high angle XRD patterns of arbitrarily selected as-deposited, processed and patterned $Co_{50}Ni_{50}$/Pt multilayers. The differences in nucleation and domain wall movement are at most only marginal. Some details of the XRD patterns and of other magnetic properties are summarized in Table 5.1.

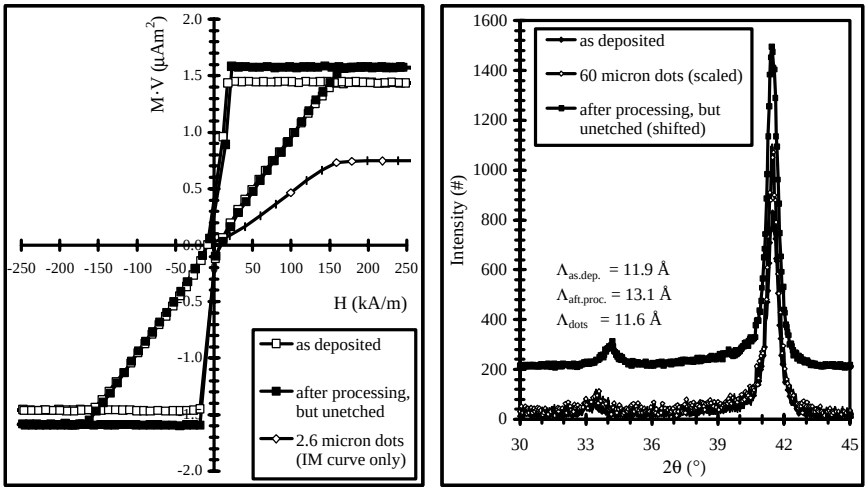

Figure 5.1: *VSM hysteresis curves (left) and XRD patterns (right) of as deposited, processed and patterned $Co_{50}Ni_{50}$/Pt multilayers. For the 2.6 micron dots only the initial magnetization curve is shown. The hysteresis of micron dots will be discussed in the next section (see also Figure 5.2).*

Table 5.1: *Bilayer thickness Λ, XRD peak intensity I, XRD peak position θ_{ml}, saturation magnetization $M_S \cdot V$, torque maximum L and effective anisotropy field $H_{K,eff}$ of as deposited, processed and patterned $Co_{50}Ni_{50}$/Pt multilayers. The data of the dots have been corrected for the coverage ratio.*

Sample	Λ (Å)	θ_{ml} (°)	I (cps)	$M_S \cdot V$ (μAm^2)	L (μNm)	$H_{K,eff}$ (kA/m)
As deposited	11.9	41.50	80	1.45	0.44	480
Processed[1]	13.1	41.45	130	1.60	0.53	530
50/100 micron dots[2]	11.7	41.40	140	1.40	0.64	730[3]

[1] The processed sample is another multilayer than the as-deposited sample, but was prepared in the same week. Though the $Co_{50}Ni_{50}$ thickness of this sample is larger than the as deposited multilayer the measured torque maximum is much larger!
[2] The dot sample was prepared more than one year later.
[3] This value has been confirmed by measurement of the rotational hysteresis loss as function of the applied field.

Considerable variations in the magnetic moment are observed, but this effect can be assigned to the relatively large variation in the $Co_{50}Ni_{50}$ thickness. It should be mentioned that with more effort the individual layer thickness can even be much better reproduced. Especially within a set of samples, e.g. the samples discussed in subsection 5.3.1, the variation in bilayer thickness is less than 3%. Then the only effect induced by the patterning process seems to be an increase in the height of the multilayer peak and in the value of the torque. Both effects may be explained by a slight improvement of the interface structure. Apparently, the patterning process can increase the perpendicular magnetic anisotropy and herewith the effective anisotropy field with up to 50%.
As conclusion can be stated that $Co_{50}Ni_{50}$/Pt multilayers can be patterned without any negative modifications in magnetic and structural properties. Instead, an increase in effective anisotropy field of up to 50% can be expected for processed multilayers. Moreover, due to the variation of bilayer thickness in different dot samples, especially in series of samples deposited over a large time period, a variation in effective anisotropy field of 20% should be taken into account.

5.3 Magnetization reversal dominated by 'defects'

5.3.1 Hysteresis in micron-sized dots

One set of micron-sized dot samples has been prepared: 2.6/4.0, 21/25, 62/80 and 215/250. Since these dots have been prepared in a very short time period, this series can be used to study the size-dependence of the magnetization reversal. The VSM hysteresis curves of all four samples are shown in Figure 5.2.

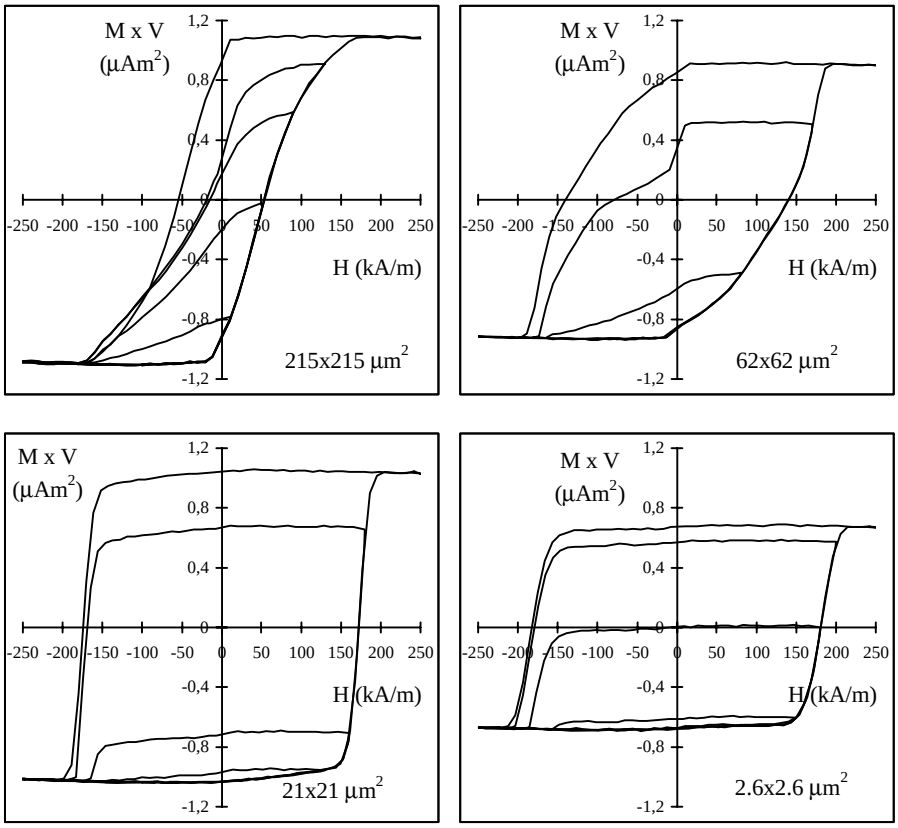

Figure 5.2: *VSM hysteresis curves of micron sized $Co_{50}Ni_{50}$/Pt multilayer dots.*

With decreasing dot size the 'normal' hysteresis curve becomes more rectangular. In fact, the magnetization reversal seems to be gradually changing from a large-dot-like reversal with low coercivity to a small-dot-like reversal with large coercivity. The following discussion will be focussed on the hysteresis in the largest and smallest dot samples only. Besides the standard hysteresis curve also 'partial' VSM hysteresis curves are shown in Figure 5.2. These curves give valuable information of the magnetization reversal. In a partial hysteresis curve the reverse field is kept smaller than the saturation field of the sample. Since no general name is known for this type of measurement (note that it is principally different from a DCD curve), it is named a partial hysteresis curve here.

For the 215x215 μm^2 dots all reversal processes are not fully irreversible. In fact, the partial hysteresis curves are very similar to the ones measured for the continuous $Co_{50}Ni_{50}$/Pt multilayer (see Figure 4.11). Apparently, for this sample similar stripe domain patterns are formed during the magnetization reversal. However, the increase of the area in the hysteresis can not be understood by this macroscopic measurement only.

On the other hand for the 2.6x2.6 μm^2 dots all reversal processes are irreversible and during magnetization reversal no domains are formed. This means that in the latter case the nucleation field should actually be called the switching field. Interestingly, this switching field approximately equals the saturation field of the as deposited multilayer. The latter is known to be proportional to the uniaxial anisotropy [5.2]. Apparently, for small dots the effective anisotropy field determines the switching field. The partial hysteresis curves also show that every dot has a fixed switching field. The rounding of the hysteresis curve therefore indicates a (narrow) switching field distribution. The latter is subject of discussion in subsection 5.4.4.
Clearly, the observed hysteresis in the 2.6/4.0 sample can be better understood than that of the 215/250 sample. In order to gain deeper understanding of the magnetization reversal of the latter sample polar Kerr microscopy has been applied to measure its nucleation field distribution. For comparison the same analysis has been applied for the 2.6/4.0 sample. For all observed 2.6/4.0 and 215/250 dots the nucleation or switching occurred immediately throughout the whole dot. The nucleation field distribution has been constructed by counting the number of nucleated dots at every field step. This measurement procedure is similar as that applied by Jamet *et al.* in their study of the magnetization reversal in micron-sized Au/Co/Au dots [5.1]. The observed nucleation field distributions are shown in Figure 5.3.

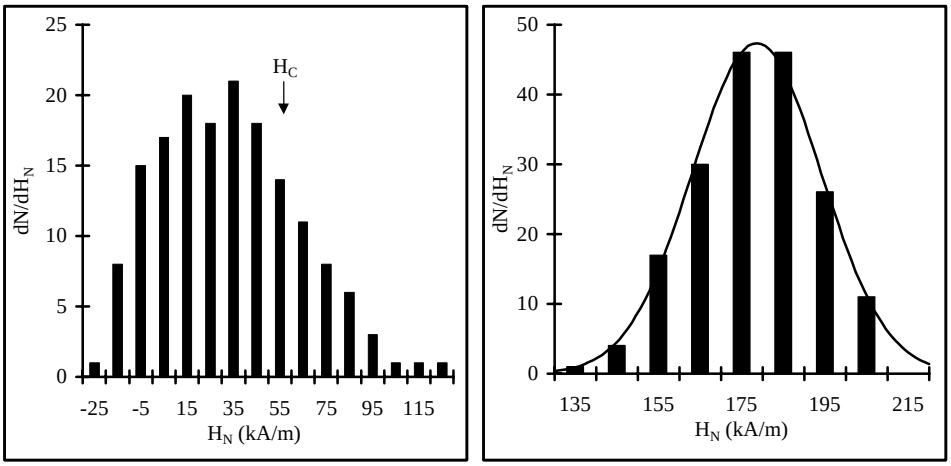

Figure 5.3: *Nucleation field distribution for 215/250 (left) and 2.6/4.0 (right) $Co_{50}Ni_{50}$/Pt multilayer dots.*

The switching field distribution of the 2.6/4.0 sample is clearly observed and can be approximated by a gaussian probability distribution centered on the macroscopic coercivity. Now also the magnetization reversal of the large dots can be discussed in more detail. The large dots have a broad nucleation field distribution. Moreover, the average nucleation field is much smaller than the coercive field of the

macroscopic hysteresis curve. This shows that every dot has a characteristic nucleation field and that at this field a stripe domain pattern is formed throughout the dot. In fact, the observed hysteresis curve could well be simulated with a broad distribution of nucleation fields and a hysteresis similar as that of the as deposited multilayer.
Concluding, the magnetization reversal in micron-sized dots is strongly dependent on the dot size. Small dots have a switching field determined by the effective anisotropy field of the $Co_{50}Ni_{50}$/Pt multilayer and therefore behave in this respect as single domain particles. Large dots have a broad distribution of nucleation fields and stripe domain patterns are formed during reversal. For dots with intermediate size both types of magnetization reversal are observed. The question arises what is the origin of the low-field nucleation in large dots. Since the contribution of low-field nucleation to the total magnetization reversal gradually decreases with dot size, the presence of some sort of defects with a random distribution in the sample seems a reasonable assumption. Then in these samples the density of defects is such that the probability to find a defect in the smallest dots is negligibly small. In the next subsection the origin and density of these defects will be further discussed. It should be emphasised that a deeper understanding of this phenomenum is required if $Co_{50}Ni_{50}$/Pt multilayers are to applied as patterned medium for recording: low-field nucleation sites would give unstable bits in an actual recording medium!

5.3.2 Origin and density of the defects

In an as deposited multilayer the nucleation sites could well be explained by the presence of so-called 'vestigal' domains [5.3] (see also section 4.7). If this type of defects would be the cause of the broad nucleation field distribution in the sample with large dots, then apparently the density of 'vestigal' domains present in the as deposited multilayer is much larger than the estimation of $< 10/mm^2$ mentioned in the introduction of this chapter. Besides, then every nucleation event should take place at a random but fixed position inside a dot. As shown in Figure 5.4.A, such nucleations have indeed been observed. However, due to the large domain wall speed, only the nucleation sites in dots having very low nucleation field ($H_N < 10$ kA/m, i.e. for 215/250 approximately only 10% of all dots) can be located. This means that the analysed nucleation sites may just be the same sites as those observed in the as deposited multilayer. Therefore the origin and position of the majority of the nucleation sites remains unknown. Interestingly, in other samples it was found that nucleation occurred only at very low field and at the edge of the dots. An example is shown in Figure 5.4.B. However, from SEM observations it was found that these types of dots always have a very rough edge compared with the sample series under study here (see Figure 5.4).

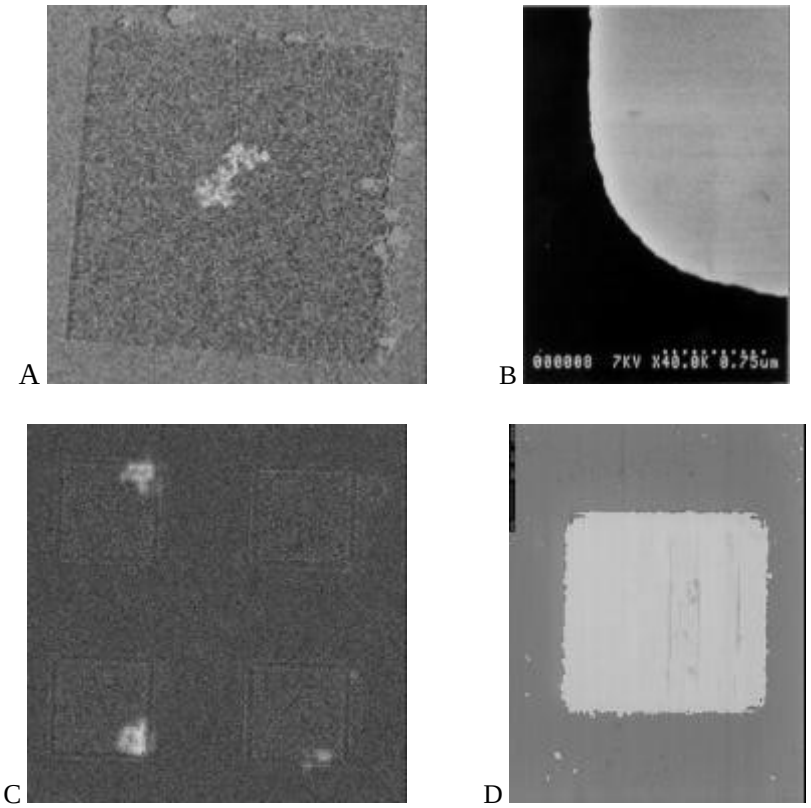

Figure 5.4: *Polar Kerr microscopy observations (images A and C) of low-field magnetization reversal in dots from two different samples (SEM images B and D):*
A,B = a 215/250 dot from the sample of Figure 5.2 and 5.3. The nucleation occurs inside the dot. The SEM image of a 2.0 x 3.0 μm^2 *area shows that these dots have a sharp and well defined edge.*
C,D = a 70/120 dot sample with a narrow nucleation field distribution ($-20<H_N<0$ *kA/m). The nucleation occurs at the dot edge. The SEM image shows that these dots have a very rough and deteriorated edge.*

Since a direct analysis of the origin (position) of the defects is not possible, an indirect method is proposed here. Following the reported observations two cases can be expected: the nucleation occurs either inside a dot or at the edge of the dot. Supposing that defects are randomly distributed along the dot edge or over the sample area and that the size of the defect is much smaller than the distance between them, then the presence of a defect in a dot is simply determined by Poisson statistics. The size-dependence of the probability for a dot to contain a defect will be different for the two cases. In the former case the average density of defects is expressed per unit of area and in the latter case the average density of defects is expressed per unit of length. This means that for defects that are also

present in the as deposited multilayer (5.1) resp. for defects introduced at the lithographically defined dot edge (5.2), different probability equations apply:

$$P(N_D \geq 1) = 1 - e^{-n_A L^2} \tag{5.1}$$

$$P(N_D \geq 1) = 1 - e^{-4 n_L L} \tag{5.2}$$

with:

N_D	:	number of defects in dot
n_A	:	average density of defects in the case of in-dot nucleation [μm^{-2}]
L	:	dot edge [μm]
n_L	:	average density of defects in the case of dot-edge nucleation [μm^{-1}]

Next with Figure 5.2 the fraction of dots containing a defect are determined for each dot size: it is assumed that dots with a nucleation field smaller than 150 kA/m contain a defect and dots with a nucleation field larger than 150 kA/m are defect-free. Finally, the defect density n_A and n_L can be determined by fitting equation (5.1) respectively (5.2) with these experimental data. The results of the fitted equations are plotted in Figure 5.5.

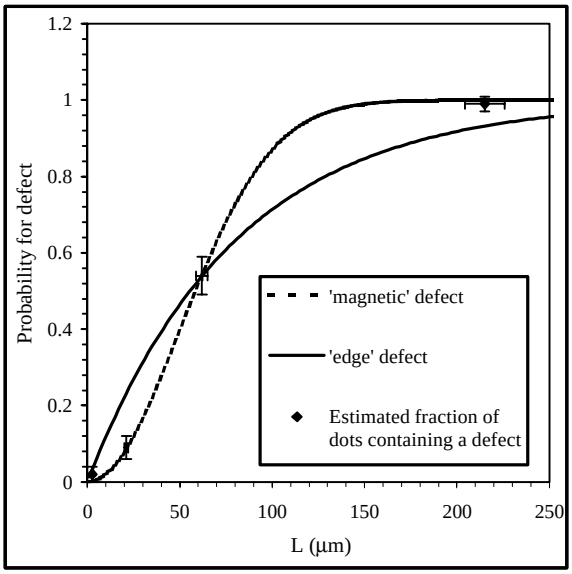

Figure 5.5: *Estimated fraction of dots containing a defect for the set of samples of Figure 5.2 as function of dot edge L. The drawn lines represent the estimated probability for the presence of a low-field-nucleation site for two cases: 1) nucleation at irregularity at the dot edge (edge defect); 2) nucleation at magnetic defect in the as deposited multilayer.*

The estimated defect densities are: $n_A = 2.0 \cdot 10^2$ mm^{-2} and $n_L = 3.1$ mm^{-1}. From a comparison of the accuracies of both fits it may immediately be concluded that the nucleation sites are not distributed along the dot edge but randomly over the surface of the multilayer and only equation 5.1 is valid. Though this information has been acquired in an indirect way, it seems convincing evidence for in-dot nucleation over the whole range of investigated dot sizes. Apparently, instead of only a few nucleation sites that were detected in the nucleation of the as deposited multilayer, many nucleation sites are present. The density of defects is $2.0 \cdot 10^2$ mm^{-2}. Moreover, these sites have a broad nucleation field distribution. Both effects can only be observed by patterning of the multilayer!

5.3.3 Relation between defect and microstructure

As mentioned before, the presence of vestigal domains have been proposed to be responsible for the low-field nucleation sites. Though this gives an explanation for the magnetic behaviour, the true origin of these sites has never been discussed in literature. If a relation with some sort of microstructural inhomogeneity could be found, this would be much more satisfactory. Assuming that low-field nucleation has to be somehow related to low magnetic anisotropy, a reasonable explanation is the presence of grains with reduced perpendicular magnetic anisotropy (PMA). Since interface anisotropy is the driving force behind the PMA, good interfaces are crucial in these multilayers. Macroscopically this has been extensively discussed in Chapter 4. Local effects were not studied. A realistic possibility is that locally the PMA is destroyed by formation of pinholes in the Pt layer. The density of pinholes will be inversely proportional to the thickness of the individual Pt layer. This suggests that the density of low-field nucleation sites is strongly related to the thickness of the Pt layer. It should be mentioned that probably a pinhole should have a minimum size to act as a low-field nucleation site.
A simple experiment can verify this suggestion. Multilayers with different Pt layer thickness have been patterned into 35/70 dots. Figure 5.6 shows the VSM hysteresis curves of multilayers with a Pt thickness of 6.7 Å and 4.5 Å. Note that these thicknesses correspond to only 2 respectively 3 monolayers. The hysteresis in both samples is significantly different. The multilayer with a Pt layer thickness of 6.7 Å has a sharp nucleation field distribution around 70 kA/m. On the other hand, the multilayer with a Pt layer thickness of 4.5 Å has a broad nucleation field distribution between 10 and 60 kA/m. These observations have been confirmed by polar Kerr microscopy. Apparently, at this specific dot size the probability for a defect increases from very small for a Pt thickness equivalent to 3 monolayers, to very large for a Pt thickness equivalent to 2 monolayers. Indeed, it seems that the decrease in Pt thickness of one monolayer causes an enormous increase in the density of low-field nucleation sites. The suggestion that these low-field nucleation sites are pinholes in the Pt layers seems therefore justified.

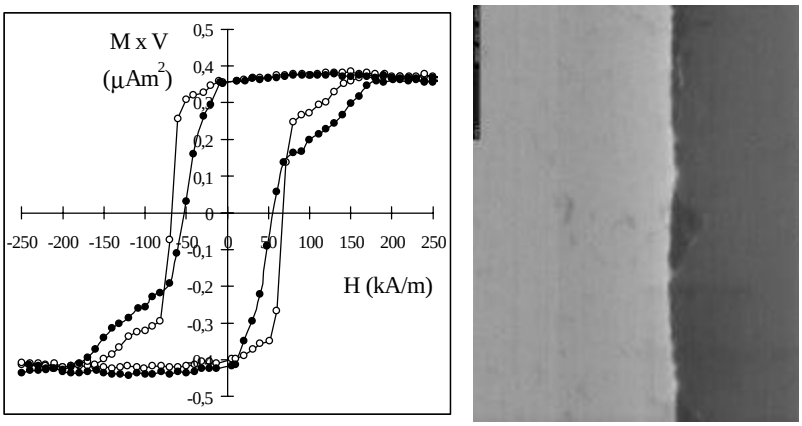

Figure 5.6: *Left: VSM hysteresis curves of 35/70 $Co_{50}Ni_{50}$/Pt multilayer dots with different Pt interlayer thickness; open circles : t_{Pt} = 6.7 Å and filled circles : t_{Pt} = 4.5 Å; Right: Typical SEM image of a 3.0 x 4.0 mm^2 area at the edge of these dots.*

Several remarks should be added to this discussion. Firstly, the nucleation or switching field of 'defect-free' dots of the sample with t_{Pt}=6.7 Å is only 70 kA/m while for the series of samples of Figure 5.2 much larger nucleation/switching fields have been observed. Since in the present series of samples an edge effect was suspected, a SEM image was taken from the edge of these dots (see Figure 5.6). Clearly, the edge is much better defined than that of the sample shown in Figure 5.4.B. Though some edge features can be observed, it is difficult to judge whether the edge of these dots is significantly worse than that of the other series of dots, shown in Figure 5.4.A. However, still it must be assumed that the quality of the dot edge is the origin for the reduction of nucleation/switching field. No other explanation can be given at this stage. It should be mentioned that the sharp nucleation field distribution around 70 kA/m showed to be very well reproducible. In fact, the large switching fields of the series of samples of Figure 5.2 have never been reproduced.

Secondly, the PMA of the samples with varying Pt thickness has been measured. From t_{Pt}=4.5 Å to t_{Pt}=6.7 Å the PMA increases with 40%, which confirms the decrease in pinhole density for larger Pt thickness. In fact, Meng *et al.* showed that the PMA of $Co_{50}Ni_{50}$/Pt multilayers shows a maximum for a Pt thickness of 9 Å [5.4]. It may be concluded that up to the deposition of approximately 4 monolayers still a considerable density of pinholes exists in the Pt layer of the as deposited multilayer.

Finally, one may still argue whether the majority of the nucleation sites (and pinholes) is not formed during the processing of the multilayer. A convincing case can be made against this suggestion. Firstly, in section 5.2 it was shown that the processing of $Co_{50}Ni_{50}$/Pt multilayers induces a significant increase in PMA. This suggests that at most the pinhole density decreases instead of increases during patterning. Secondly, whether this decrease is realistic, can be strongly questioned.

In this respect an important observation is that the minimum nucleation field observed in dots is equal to the nucleation field in as deposited multilayers. This seems a solid confirmation that the pinholes present in the multilayer do not change in size during patterning. Besides, changes in pinhole size would involve true crystal modifications and these are not expected at the temperatures involved in the patterning process. Finally, recrystallization processes probably would also introduce stress or strain effects. The multilayer peak in the high angle X-Ray Diffraction pattern is unchanged after patterning, which also seems to exclude such effects.

5.3.4 Summary

Concluding, two series of samples have been prepared to study the nature and origin of the magnetization reversal in micron-sized $Co_{50}Ni_{50}$/Pt multilayer dots. The observed hysteresis could well be explained by the presence of randomly distributed low-field nucleation sites. These sites are already present in the as deposited multilayer and are probably pinholes in the Pt layer. While in continuous multilayers only the softest nucleation site is measured, in patterned multilayers the whole distribution of nucleation fields is probed. In patterned structures also lithographically induced defects can be present, but their role in the hysteresis can generally well be separated from that of the intrinsic defects in the multilayers.
Though quite strong evidence has been gathered, some additional experiments are necessary for a confirmation of the proposed mechanism of magnetization reversal. First of all, the position of nucleation should be located for defect-dots nucleating at high field, i.e. $+10<H_N<+120$ kA/m. At present the high domain wall speed makes this impossible. Probably, a method like the one applied by Kirilyuk *et al.* may be usefull [5.5]. They used field pulses of only a few microseconds to freeze the propagating domains in Au/Co/Au sandwiches. Also a synchronisation of image acquisition and generation of a nucleation event may be used to 'catch' the nucleation in a dot. Secondly, other patterning techniques should be applied to determine the density of low-field nucleation sites. For instance, a process based on lift-off would circumvent any baking steps of the as deposited multilayer. Also, totally different patterning technology, such as Focussed Ion Beam etching, provides an independent way to determine the defect density in the as deposited multilayers.

5.4 Magnetization reversal in 'defect-free' multi and single domain dots

In the previous section the magnetization reversal in $Co_{50}Ni_{50}$/Pt multilayer dots with defects has extensively been discussed. It was also shown that 2.6 x 2.6 μm^2 dots are free from defects and that their switching field is mainly determined by the effective anisotropy field. In this section the magnetization reversal in defect-free dots will be discussed in more detail. Moreover, the goal is to show the preparation and characterization of single domain dots.

5.4.1 Prepared submicron sized dot samples

A set of samples with 2D arrays of submicron $Co_{50}Ni_{50}$/Pt multilayer dots has been prepared by laser interference lithography (LIL). For all samples the standard $Co_{50}Ni_{50}$/Pt multilayer discussed in section 4.7 has been used. The details of the patterning process are described in section 3.3. At a fixed period of 570 nm, arrays with different dot diameter D have been prepared by varying the exposure dose in LIL. The final dot size, determined with SEM, showed to be in the range between 140 and 280 nm: 140, 180, 280 (I) and 280 (II) nm. For all 570 nm arrays the dots have the shape of a disk and after etching a thin resist layer remains on their top (see Figure 5.7).

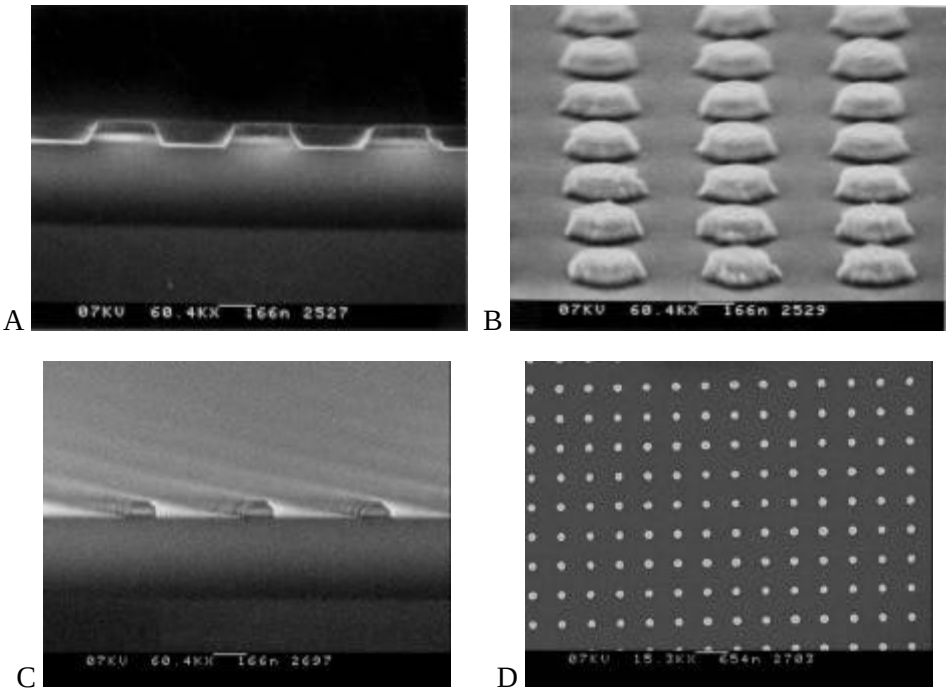

Figure 5.7: *SEM images of submicron $Co_{50}Ni_{50}$/Pt multilayer dots prepared with Laser Interference Lithography at a fixed period of 570 nm: A) Cross section of 280 nm dots; B) Oblique view of 280 nm dots; C) Cross section of 140 nm dots; D) Top view of 140 nm dots.*

The exposure time for the 200 nm array showed to be very critical and therefore for this study only one dot diameter was patterned. These dots have the shape of a pyramid or cone (see Figure 5.8).

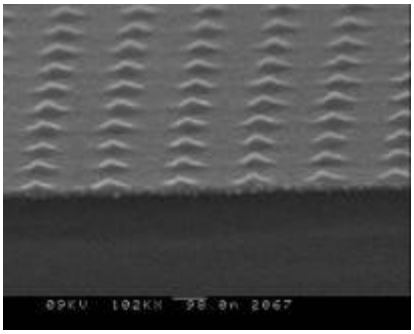

Figure 5.8: *SEM image of nanoscale $Co_{50}Ni_{50}$/Pt multilayer dots prepared with Laser Interference Lithography at a period of 200 nm.*

After etching no resist was left on their top, which means that the multilayer has partially been etched and the total thickness has been reduced to approximately 15 nm. The area of the 200 nm arrays is around 2.5 x 2.5 cm^2, from which four samples were cut. Because the dot size was inhomogeneous over the whole area, D of each sample varied from 60 to 80 nm.
With Magnetic Force Microscopy (using EBID tips) the domain state after in-plane demagnetization of the samples with D = 180 nm and 70 nm has been imaged. As shown in Figure 5.9, the 180 nm dots are multi domain (MD) with two or three domains, while for the 70 nm dots only single domain (SD) states are observed.

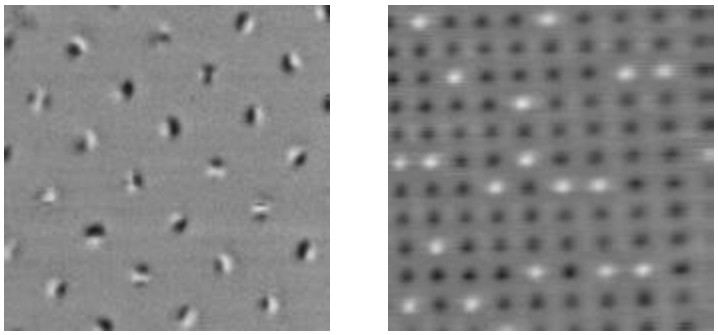

Figure 5.9: *Magnetic force microscopy images of $Co_{50}Ni_{50}$/Pt multilayer dots with different dot diameter: 180/570 nm and multi domain (left;measurement by K. Babcock, Digital Instruments); 70/200 nm and single domain (right).*

5.4.2 Hysteresis and initial magnetization

The perpendicular hysteresis curves of the 70 nm and 180 nm dots are shown in Figure 5.10. They look very similar. In fact, the hysteresis curve has an identical shape for all samples: the remanence is close to 100 % and the reversal takes place in a narrow field range around H_c. In Table 5.2 H_c is given as function of D.

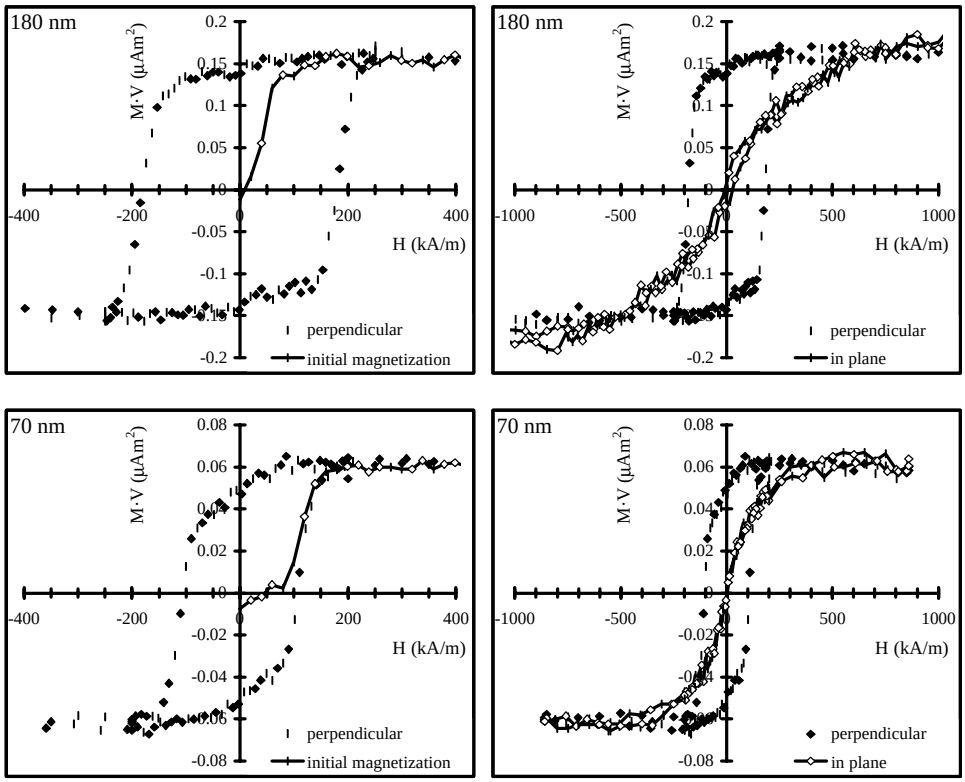

Figure 5.10: *VSM hysteresis and initial magnetization curves for 180/570 nm (top) and 70/200 nm (bottom) $Co_{50}Ni_{50}$/Pt multilayer dots.*

Table 5.2*: H_C, $H_{K,eff}$ and demagnetized domain state as function of dot size. Also the properties of the unpatterned multilayer are given.*

D (nm)	H_C (kA/m)	$H_{K,\,eff}$ (kA/m)	SD/MD
60 – 80	120 - 80	500	SD
140	260	850	SD/MD
180	180	700	MD
280 (I)	160	700	MD
280 (II)	250	800	MD
$Co_{50}Ni_{50}$/Pt multilayer	15	500	MD

Over the whole range, no clear relation between D and H_c is found. This phenomenum will be discussed later.
Both the initial magnetization curves and the in-plane hysteresis curves are significantly different for the 180 nm multi domain dots and 70 nm single domain dots (Figure 5.10). The 180 nm dots show smooth domain wall movement and the in-plane remanence is non-zero, while the 70 nm dots show switching similar to the

perpendicular hysteresis curve and the in-plane remanence is zero. Apparently, for these samples, the demagnetized domain state can be probed by both the initial magnetization and the in-plane hysteresis measurements. Therefore, initial magnetization curves have been used to determine the demagnetized domain state for all samples. The results are also shown in Table 5.2. The initial magnetization curve of the 140 nm dots shows both MD and SD states (see Figure 5.11). The ratio of MD to SD dots, as determined from the ratio of magnetization reversals at low field to those at high field, is around 8:1, which is probably related to the spread in dot size. So, roughly estimated, the transition from MD to SD occurs at 140 nm.

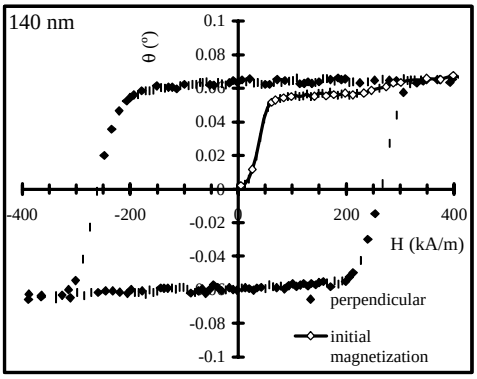

Figure 5.11: *Polar Kerr hysteresis and initial magnetization curves for 140/570 nm $Co_{50}Ni_{50}$/Pt multilayer dots.*

Now the demagnetized domain state has unambiguously been determined, the differences in magnetization reversal of single and multi domain dots may be discussed. Interestingly, no difference in the shape of the perpendicular hysteresis curves can be found. However, when comparing only the single domain dot samples, it shows that with decreasing dot size the coercivity increases. This phenomenum is in agreement with common single domain theory (see Chapter 2). The ratio between coercivity and effective anisotropy field is approximately 0.20. The dominant mechanism of magnetization reversal probably is some sort of incoherent rotation like curling. The observation that there is no correlation between dot size and coercivity for the multi domain dot samples might indicate that the switching field more strongly depends on the roughness of the dot edges or the sharpness of the dot corners. This phenomenum will be more deeply discussed in subsection 5.4.4.

Surprising result is that H_c of the SD dots is considerably smaller than H_c of the MD dots. This contradiction might be explained by a comparison of $H_{K,eff}$ between all samples. Therefore $H_{K,eff}$ was calculated from the ratio of the torque maximum and the magnetic moment and is also given in Table 5.2. Indeed, compared to the MD dots, a significantly lower effective anisotropy field is found for the SD dots.

Note that for the SD dots $H_{K,eff}$ is approximately equal to the saturation field of the in-plane hysteresis curve (Figure 5.10).
The variation in effective anisotropy field needs further discussion. Compared to the unpatterned $Co_{50}Ni_{50}$/Pt multilayer, $H_{K,eff}$ of the MD dots is about 50 % larger. The origin was found to be an increase in K_{eff}. As shown in section 5.2 such an increase may be induced by the patterning process. However, at these aspect ratios, shape effects can play an important role as well. The contribution of the shape anisotropy to this increase can roughly be estimated by approximating the dot shape with an oblate ellipsoid. With the analytical expression for the demagnetizing factor [5.8] and the proper expression for the shape anisotropy of a multilayer based on the mean square magnetisation [5.9], it can be calculated that for 140 - 280 nm dots the shape anisotropy induces a 64 - 36 % increase of K_{eff}. Apparently, for the 140 - 280 nm dots the increase of $H_{K,eff}$ can also fully be explained from the reduced dimensions. The same increase should then be expected for the 60-80 nm dots. Since this is not the case, the intrinsic anisotropy of the multilayer itself must have been reduced. The most probable cause is the fact that these dots have partially been etched (see Figure 5.8). This observation has two consequences for the intrinsic perpendicular magnetic anisotropy. Firstly, the multilayer structure may be damaged. Most likely, a few bilayers in the upper part of the multilayer stack have been intermixed, which has destroyed the origin of the perpendicular anisotropy in these multilayers, i.e. interface anisotropy. Secondly, from Chapter 4 it is known that the lower part of as deposited $Co_{50}Ni_{50}$/Pt multilayers has lower perpendicular anisotropy than the upper part. Since the dot height has been reduced from 30 nm to approximately 15 nm and the dot has a pyramidal shape instead of a disk shape, the average perpendicular anisotropy will have been decreased. Concluding, it is likely that the origin of the smaller H_c of the SD dots is the reduction of intrinsic anisotropy.

5.4.3 Rotational hysteresis loss of single and multi domain dots

Measurements of the rotational hysteresis loss are a useful tool for a more detailed analysis of the mode of magnetization reversal in small particles [5.8]. In general these measurements are done for single domain particles only. Here the rotational hysteresis loss of both single and multi domain dot samples has been studied. For the 280 (I) nm (MD) and 80 nm (SD) dots the rotational hysteresis loss W_r as function of applied field is shown in Figure 5.12.

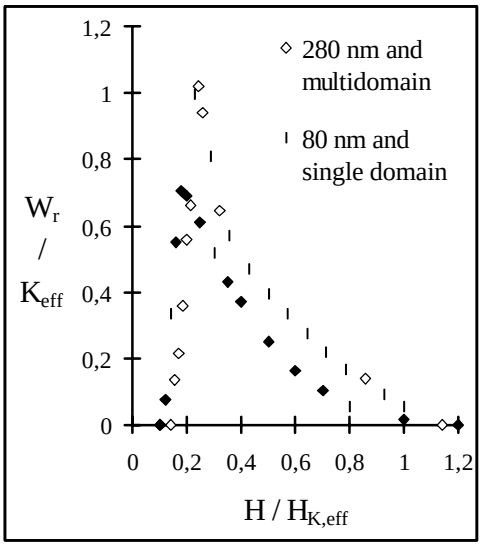

Figure 5.12: *Rotational hysteresis loss for 280 (I)/570 and 80/200 nm $Co_{50}Ni_{50}$/Pt multilayer dots.*

In both cases the W_r curve is similar to that measured and calculated for aligned single domain elongated ferromagnetic particles [5.9-10]. W_r peaks around H_c and vanishes around $H_{K,eff}$. Unlike the W_r curve for the as deposited $Co_{50}Ni_{50}$/Pt multilayer in Figure 4.13, no demagnetizing effects are present. The calculated rotational hysteresis loss integral (R_H) is around 1.2 for both samples, which indicates some sort of incoherent rotation as the mechanism for magnetization reversal [5.8]. Apparently W_r does not depend on the size and demagnetized domain state of the dots, which means that the rotational hysteresis loss can not be used to discriminate between MD and SD dots.

5.4.4 Origin of observed switching field distribution for multidomain dots

For the single domain dots the observed switching field distribution ΔH_{SF} may be explained by a simple non-uniformity of dot size over the sample area. For the multi domain dots this explanation does not apply. Interestingly, when the hysteresis curves of the multi domain dot samples are scaled to coercivity and saturation magnetization, the relative ΔH_{SF} appears to be similar for all samples (see Figure 5.13).

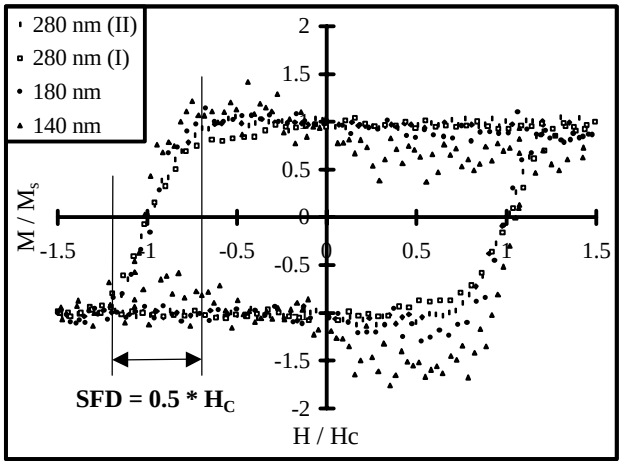

Figure 5.13: *Scaled VSM hysteresis curves of the four submicron multidomain $Co_{50}Ni_{50}$/Pt multilayer dot-samples. The switching field distribution is indicated in the graph.*

In a discussion about the origin of the observed ΔH_{SF} of multi domain dots at least three effects should be taken into account. Firstly, magnetostatic interactions may contribute to the ΔH_{SF}. Secondly, since the switching field is proportional to $H_{K,\,eff}$, the effective anisotropy field distribution $\Delta H_{K,\,eff}$ should be known. Thirdly, the sample homogeneity should be checked. With respect to these three items, the following remarks can be made:

- Since the ΔH_{SF} seems independent on dot size and therefore also on dot spacing, magnetostatic interactions can be excluded and are irrelevant for this discussion.
- In principle, $\Delta H_{K,\,eff}$ can be estimated from a measurement of the rotational hysteresis loss. Figure 5.12 indicates that $\Delta H_{K,\,eff}$ of the 280 (I) nm dots is at most 140 kA/m (20% of $H_{K,\,eff}$). Assuming a fixed ratio between switching field and effective anisotropy field, such a $\Delta H_{K,\,eff}$ may cause a ΔH_{SF} of 20%, which is much too low to explain the observed ΔH_{SF}.
- The ΔH_{SF} of a 60x80 μm^2 area of the 280 (I) nm dot sample has been determined by polar Kerr microscopy with an advanced setup in the laboratory of Prof. J. Ferré, Université Paris-Sud, Orsay, France (see also [5.1]). Figure 5.14 shows four zoomed images during the magnetization reversal. From the full area, the hysteresis curve has been reconstructed and showed to coincide with the macroscopic hysteresis curve (see Figure 5.15).

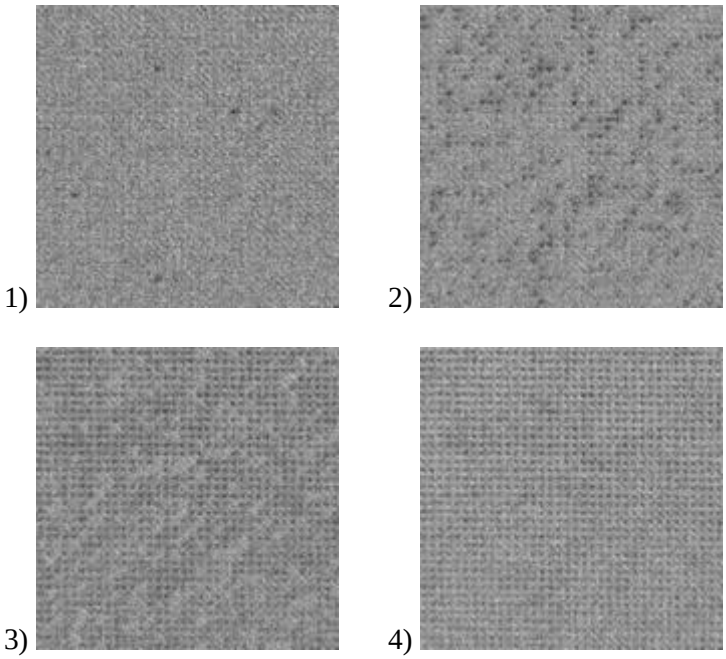

Figure 5.14: *Polar Kerr microscopy images of the remanent state of 280 (I)/570 nm $Co_{50}Ni_{50}$/Pt multilayer dots for an applied field of: 1) 102 kA/m; 2) 145 kA/m; 3) 189 kA/m; and 4) 247 kA/m.*

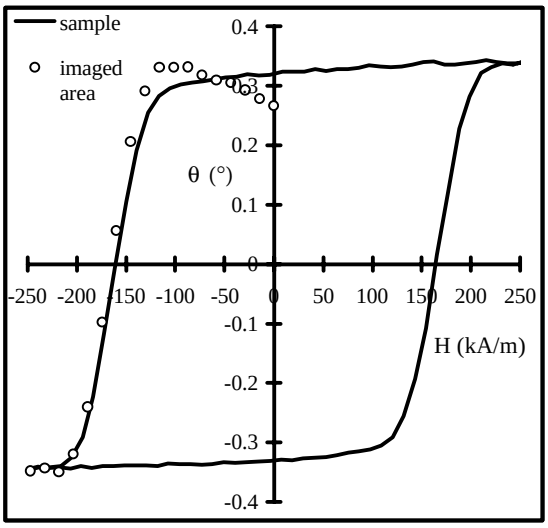

Figure 5.15: *Hysteresis curve reconstructed from polar Kerr microscopy observations of a 60x80 μm^2 area of the 280 (I)/570 nm $Co_{50}Ni_{50}$/Pt multilayer dot sample.*

These observations seem to confirm that both the values of the switching field and its distribution may rather depend on effects like dot edge roughness than on intrinsic magnetic properties. An interesting challenge would be the observation of the position of the start of magnetization switching in multi domain dots to confirm the relation with dot edge. In fact, for this purpose defect-free micron-sized dots would be more suitable because of the larger dot size.

5.4.5 Activation volume and thermal stability of single domain dots

The thermal stability of the 70 nm single domain dots has been investigated. In order to obtain an accurate value for the activation volume and relaxation time, both the hysteresis and the thermally activated switching at room temperature have been measured by a Polar Kerr Magnetometer/Spectrometer (see [5.11]). Moreover, for the time dependent measurements the standard measurement procedure was adapted at two important points. Firstly, the data in the first 30 s was stored in the buffers of the lock-in amplifier to allow measurement on a short time scale. Secondly, software controlled feedback of the applied field provided a field stability better than 0.5 kA/m. Figure 5.16 shows the measured Kerr rotation as function of wavelength.

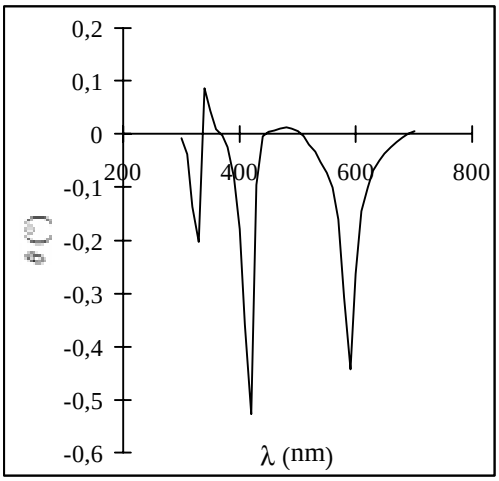

Figure 5.16: *Polar Kerr rotation as function of wavelength for 70 nm $Co_{50}Ni_{50}$/Pt multilayer dots prepared on Si/SiO_2 substrate.*

The spectrum shows strong maxima associated with interference effects in the oxidized silicon substrate. All measurements have been carried out at one of these maxima, i.e. λ = 590 nm, to benefit from the high Kerr rotation at this wavelength. Figure 5.17 shows the measurements of hysteresis and magnetic viscosity.

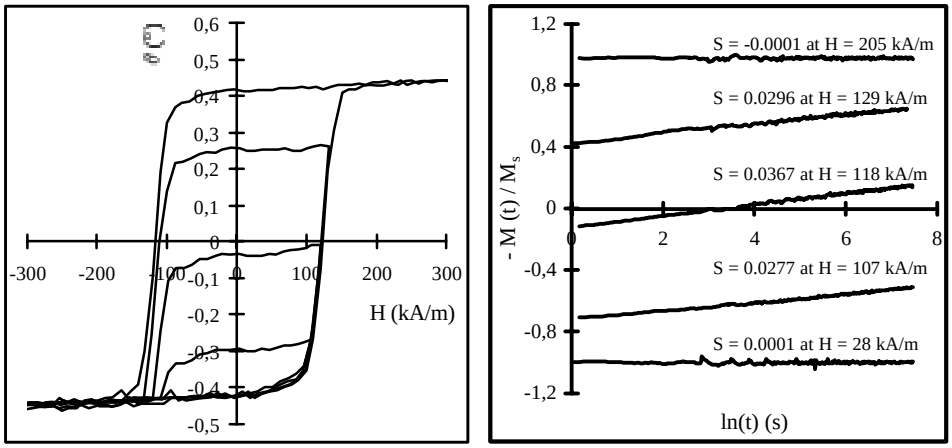

Figure 5.17: *Hysteresis and magnetic viscosity curves of single domain 70 nm $Co_{50}Ni_{50}$/Pt multilayer dots (measured with Polar Kerr Magnetometry at 570 nm).*

Subsequently, with Equation 2.22 the activation volume at H_C has been calculated and equals $(8 \pm 1) \times 10^{-18}$ cm^3 which is about six times smaller than the dot volume. Perhaps this volume might be related to a volume of reduced magnetic anisotropy caused by etching damage induced in the patterning process. Since both the switching field distribution and the magnetic viscosity are roughly symmetric around H_C the activation volume can be assumed to be independent on the applied field. The worst relaxation time τ_{min} present in the sample corresponds to dots with H_C = 80 kA/m. Then, with Equation 2.21**,** τ_{min} is calculated to be 3.8×10^3 year. This value seems sufficient for storage. However, with statistic rules it can be calculated that in a 50 Gbit hard disk consisting of this type of dots already within 2.5 s a dot will have been switched by thermal activation. Since the relaxation time is a steep function of the coercivity, a 50% increase in coercivity would solve the problem of thermally activated switching. It can be expected that by avoiding the etching damage of the 70 nm dots this can easily be achieved.

5.5 Conclusions

In this chapter the magnetization reversal in submicron and micron-sized $Co_{50}Ni_{50}$/Pt multilayer dots is described. It was checked that the patterning process does not deteriorate the magnetic properties of the multilayers. Instead, an improvement of the perpendicular magnetic anisotropy was found.

The magnetization reversal of $Co_{50}Ni_{50}$/Pt multilayer dots is strongly dependent on dot size. In fact, over the studied range of sizes, i.e. 60 nm – 215 μm, three main types of reversal can be distinghuished.

For dots larger than 20 μm the reversal is dominated by small structural defects in the as deposited multilayer. These dots have a broad nucleation field distribution and domains are formed during reversal.

Dots with a size between 140 nm and 20 μm are actually multi domain as well, but no domains are formed during the perpendicular (easy-axis) reversal. The general results obtained on these samples are to a high extent in agreement with the results of Jamet *et al.* on micron-sized Au/Co/Au dots [5.1].
Finally, dots smaller than 140 nm can not be demagnetized and appear as single domain dots. Their mode of reversal is incoherent rotation.
Finally, it can be concluded that with the preparation of 70 nm $Co_{50}Ni_{50}$/Pt multilayer dots (200 nm center-to-center spacing) a prototype of patterned storage medium has been realised. This 16 Gbit/in^2 medium consists of truly single domain dots with large uniaxial magnetic anisotropy. The thermal stability is not sufficient for long-term stability, but by an optimization of the patterning process this can be enormously improved without the need for another material. Due to the lack of magnetostatic interactions between dots and the presence of a strong intrinsic perpendicular magnetic anisotropy, this patterned medium has superior storage properties compared to single-element (Co or Ni) patterned media reported so far [5.12-14].

References

[5.1] J.P. Jamet, S. Lemerle, P. Meyer, J. Ferré, B. Bartenlian, N. Bardou, C. Chappert, P. Veillet, F. Rousseaux, D. Decanini, and H. Launois, *'Dynamics of the magnetization reversal in Au/Co/Au micrometer-size dot arrays'*, Phys. Rev. B **57** (1998) 14320-14331.

[5.2] H.J.G. Draaisma and W.J.M. de Jonge, *'Magnetization curves of Pd/Co multilayers with perpendicular anisotropy'*, J. Appl. Phys. **62** (1987) 3318-3322.

[5.3] W.B. Zeper, H.W. van Kesteren, B.A.J. Jacobs, J.H.M. Spruit, and P.F. Carcia, *'Hysteresis, microstructure, and magneto-optical recording in Co/Pt and Co/Pd multilayers'*, J. Appl. Phys. **70** (1991) 2264-2271.

[5.4] Q. Meng, *'Magneto-optical recording media CoNi/Pt and Co/Pt multilayers'*, Ph.D. thesis, Universiteit Twente, The Netherlands (1996).

[5.5] A. Kirilyuk, J. Ferré, V. Grolier, J.P. Jamet, and D. Renard, *'Magnetization reversal in ultrathin ferromagnetic films with perpendicular anisotropy'*, J. Magn. Magn. Mater. **171** (1997) 45-63.

[5.6] S. Chikazumi, *'Physics of magnetism'*, John Wiley Inc. (1964) 21.

[5.7] A.A. Kusov, S.S. Jaswal and Z.S. Shan, *'Shape anisotropy of magnetic multilayers'*, Phys. Rev. B 46 (1992) 3123-3124.

[5.8] G. Bottoni, D. Candolfo, A.. Cecchetti, and F. Masoli, *'Analysis of the magnetization switching using the rotational hysteresis integral'*, J. Magn. Magn. Mater. **193** (1999) 329-331.

[5.9] I.S. Jacobs and F.E. Luborsky, *'Magnetic anisotropy and rotational hysteresis in elongated fine-particle magnets'*, J. Appl. Phys. **28** (1957) 467-473.

[5.10] S. Shtrikman and D. Treves, *'The coercive force and rotational hysteresis of elongated ferromagnetic particles'*, J. De Phys. et Radium **20** (1959) 286-289.

[5.11] W.P. van Drent, *'CoNi/Pt multilayers for magneto-optical recording'*, Ph.D. thesis, Universiteit Twente, The Netherlands (1995).

[5.12] G. Meier, M. Kleiber, D. Grundler, D. Heitmann, and R. Wiesendanger, *'Vertical polarization of quantum magnets in high density arrays of nickel dots with small height-to-diameter ratio'*, Appl. Phys. Lett. **72** (1998) 2168-2170.

[5.13] B. Cui, W. Wu, L. Kong, X. Sun, and S.Y. Chou, *'Perpendicular quantized magnetic disks with 45 Gbits on a 4x4 cm^2 area'*, J. Appl. Phys. **85** (1999) 5534-5536.

[5.14] T.A. Savas, M. Farhoud, H.I. Smith, M. Hwang, and C.A. Ross, *'Properties of large-area nanomagnet arrays with 100 nm period made by interferometric lithography'*, J. Appl. Phys. **85** (1999) 6160-6162.

Chapter 6

Discussion, conclusions and recommendations

In this concluding chapter the experimental results on the magnetic properties of the submicron $Co_{50}Ni_{50}$/Pt multilayer dots, presented in Chapter 5, will be compared to the predictions made in Chapter 2. Considerations of the role of experimental factors should give an improved understanding of the discrepancies between experiment and theory. Suggestions for the further development of patterned media recording are discussed as well.

6.1 $Co_{50}Ni_{50}$/Pt multilayer dots: experiments vs. theory

In recent years an increasing number of studies on the magnetic properties of lithographically prepared submicron and nano-sized dots have been published. Many of these studies used Co, Ni or NiFe as magnetic material [6.1-7 + references]. In this work $Co_{50}Ni_{50}$/Pt multilayers with a large intrinsic perpendicular magnetic anisotropy and strong intergranular exchange coupling have been used [6.8,9]. The magnetic properties have been investigated using several macroscopic characterization techniques as vibrating sample - and torque magnetometry. With respect to the combination of the size of the patterned dots, choice of material and the extensive characterization, no comparable study is found in literature. Here, the results on several measured magnetic properties will be discussed and, where possible, be compared with the predictions made in Chapter 2:

- ***Critical dot diameter***

In Chapter 2 the critical dot diameter was defined as the dot diameter at which the single domain state has lower energy than the two domain state. Both analytical and numerical calculations predicted that the transition for $Co_{50}Ni_{50}$/Pt multilayer dots would occur at approximately 70 nm. The experimental results presented in Chapter 5 showed that dots smaller than approximately 120 nm can not be demagnetized. Though more experimental work is necessary for firm conclusions, this indicates that the experimentally determined transition occurs at much larger dot diameters. Two explanations may be given for the quite large gap between the calculated and measured values. Firstly, the calculations have been carried out with a model where the multilayer is approximated by homogeneous material. Since the individual layers in the multilayer are only 6 Å (i.e. an order of magnitude smaller

than the wall width), this seems rather fair. Nevertheless, calculations based on a true multilayer structure would be more accurate. Unfortunately, the micromagnetic simulation package could not be adapted for modeling the multilayer structure. Secondly, the demagnetization experiments have been done in uniform DC fields of a vibrating sample magnetometer. Apparently, under this condition, a domain wall could not be nucleated for dots smaller than 120 nm. If the demagnetization experiments would be carried out in non-uniform AC fields, such as the strayfield of a write-head, the transition may perhaps be found at (much) smaller diameters. Micromagnetic simulations with non-uniform fields may also reveal the significance of this effect.

- ***Switching field***

The analytical calculations presented in Chapter 2 predicted a switching field of at least 500 kA/m for $Co_{50}Ni_{50}$/Pt multilayer dots. The highest switching field observed in the experiments is 300 kA/m. Again the error made by the simplified modelling of the multilayer is expected to be quite small and seems to be insufficient to explain the difference between calculated and experimental value. A more reasonable explanation may be found in local deteriorations of magnetic anisotropy together with shape effects. Micromagnetic calculations of the switching field, also presented in Chapter 2, confirmed that a non-perfect dot shape can considerably reduce the switching field. Both inferior growth of the first bilayers (as discussed in Chapter 4) and etching damage in the outer 5 nm thick shell of the dot (as discussed in Chapter 3) may act as additional nucleation sites and allow switching at even lower fields. Both the growth of a (thin) Pt underlayer and the development of an optimized patterning process which reduces the etching damage, may be fruitfull to considerably increase the switching field and close the gap between experimental and calculated values.

- ***Activation volume***

The activation volume measured for 70 nm $Co_{50}Ni_{50}$/Pt multilayer dots is approximately $8 \cdot 10^{-18}$ cm^3, which is six times smaller than the dot volume ($V_{dot} \approx 4.8 \cdot 10^{-17}$ cm^3). As mentioned in Chapter 2, the activation volume does not have to have a simple relation with any physical volume, which gives its concept a rather abstract character. Because the preparation of these dots is well controlled and the dots have a high degree of uniformity, it is tempting to establish at least a qualitative relation between activation volume and the dot's microstructure. In this respect, the same structural features as described above in the discussion of the switching field may play a role. A controlled variation of these features may confirm this suggestion.
On the other hand, the activation volume can be compared to a characteristic magnetic volume, i.e. the volume of coherent rotation. With Equation (2.16) this volume is estimated to be $6 \cdot 10^{-18}$ cm^3 for $Co_{50}Ni_{50}$/Pt multilayers (in the case of a

sphere). Indeed, this values agrees very well with the value of the activation volume. It would be a challenge to study this relation for other materials as well.

- ***Switching field distribution***

The switching field distribution (SFD) of the $Co_{50}Ni_{50}$/Pt multilayer dots is typically around 100 kA/m. Partial hysteresis curves show that the SFD is an intrinsic property of the dots and that it is not determined by magnetostatic interactions or time dependent phenomena. Also the distribution in effective anisotropy field seems insufficient to explain the measured SFD. It has to be concluded that some sort of statistical distribution of nucleation sites is present. Unfortunately, its origin is hard to reveal. The control of the SFD may be one of the most crucial achievements to obtain a suitable recording medium.

6.2 An outlook on patterned medium recording

In the previous chapter it was shown that in this work a prototype patterned medium based on $Co_{50}Ni_{50}$/Pt multilayers has been realised. Nevertheless, the road towards application of this type of medium in a storage device is still long. Many practical problems concerning system design, patterning technology and control of magnetic properties have to be overcome. In this section the latter two issues will be addressed.

6.2.1 Patterning technology

In the present work laser interference lithography (LIL) was selected as the most suitable patterning technology for studies on submicron magnetic dots. With a relatively simple process, dot densities up to 16 Gbit/in^2 have been achieved. Patterned medium recording is 'scheduled' for bit densities larger than a few hundred Gbit/in^2. A cheap technology with the capability of patterning large area periodic structures with sub-10 nm sizes and sub-50 nm distances is not yet readily available. At the present rate of the increase of bit density in hard disks of 60-100 %, such a (mature) patterning technology will be necessary for 200 Gbit/in^2 laboratory demonstrations in 3-5 years! Mass fabrication will have to follow a few years later. For this purpose, nano-imprint technology [6.10] is a good candidate but, since it is a contact technology, may have too large mask costs. Another interesting candidate is technology based on selforganizing colloids of magnetic nanocrystals, which consist of nanosized particles encapsulated in polymer [6.11]. The limitations of this technique still need to be explored. In case no cheap manufacturing process can be found for patterned media, it may be doubted whether they will ever be commercialized. Another possibility is that they will appear on the market in specialty products as the μSPAM introduced in Chapter 1. For prototyping of and material studies on patterned media LIL can still play an important role. The advantages of simplicity, flexibility and area of exposure are

unbeatable. As alternative for studies of close-packed nano-sized dots focussed-ion-beam technology is the method of choice.

6.2.2 Magnetic material

The motivation of the choice to use $Co_{50}Ni_{50}$/Pt multilayers as magnetic material for the patterned medium, was that these multilayers have both a large uniaxial (perpendicular) magnetic anisotropy and a strong intergranular exchange coupling. Moreover, the extensive knowledge gathered on their structural and magnetic properties, reported in Chapter 4, allowed quantitative studies on the magnetic properties of the prepared dots. Already in Chapter 2 some other candidate materials were mentioned: i.e. bariumferrite, Co/Fe $L1_0$ alloys and amorphous TbFeCo. Let us now consider the material requirements for a future device of 1 cm^2 having a storage capacity of 50 Gbit (=320 Gbit/in^2). The period of the 2D array should then be 45 nm. The first requirement will be the thermal stability of this medium. Table 6.1 shows the element size at which the device is still thermally stable for the four different materials.

Table 6.1: *The size of a cubic element at which, in a 50 Gbit patterned medium of several materials with uniaxial magnetic anisotropy, thermal relaxation of at least one bit occurs within 10 years (with Equation 2.20 and Table 2.1).*

Material	**l_{sp} (nm)**
$BaFe_{12}O_{19}$	21
FePt ($L1_0$ phase)	9
TbFeCo	31
$Co_{50}Ni_{50}$/Pt (multilayer)	18

For all materials the element size is considerably smaller than the element period. The degree of magnetostatic interactions will be another criterium for the choice of material. Rough calculations show that for all materials the interaction fields between the elements are of the order of several tens of kA/m at most.
The switching fields of the nanosized elements will be an order of magnitude higher than those in present media. Therefore, it is inevitable that recording on patterned media will be thermally assisted. Similar to magneto-optic recording, the switching field can be sufficiently lowered by heating the medium with a laser spot. In contrast to magneto-optic recording, the actual writing will be done by a nanosized write-device (instead of an external permanent- of electro-magnet) to allow the switching of individual elements. Such a writing scheme means that the switching field distribution at the writing temperature is probably the most critical issue. The tolerances of this parameter will be defined in the design of the recording system. At this moment, a quantitative estimation of this effect can not be given.

Finally, when considering the use of other materials in studies on patterned media, attention has to be paid to some aspects. Firstly, the amorphous TbFeCo alloy has a uniaxial magnetic anisotropy but, due to its amorphous nature, may also be very inhomogeneous. Secondly, bariumferrite and Co/Fe alloys with $L1_0$ phase can be prepared with a uniaxial magnetic anisotropy but often have a weak intergranular exchange coupling. The high deposition temperatures needed for the crystallization often induces a magnetic decoupling of the grains. The consequence of such an effect on the magnetic properties of a patterned medium was very recently shown in a study on nanosized CoCrPt dots with perpendicular anisotropy [6.10]. The switching field distribution of this medium, as observed by Magnetic Force Microscopy, is around 160 kA/m, which is twice as large than that in the $Co_{50}Ni_{50}$/Pt patterned media with similar coercivity ($H_C \approx 120$ kA/m) presented in this work. The authors of the paper mentioned that the weak intergranular exchange coupling is the reason for this behaviour.

References

[6.1] J.F. Smyth, S. Schultz, D.R. Fredkin, D.P. Kern, S.A. Rishton, H. Schmid, M. Cali, and T.R. Koehler, *'Hysteresis in lithographic arrays of permalloy particles: experiment and theory (invited)'*, J. Appl. Phys. **69** (1991) 5262-5266.

[6.2] R.M.H. New, R.F.W. Pease, and R.L. White, *'Physical and magnetic properties of submicron lithographically patterned magnetic islands'*, J. Vac. Sci. Technol. B **13** (1995) 1089-1094.

[6.3] M. Hehn, K. Ounadjela, J.P. Bucher, F. Rousseaux, D. Decanini, B. Bartenlian, and C. Chappert, *'Nanoscale magnetic domains in mesoscopic magnets'*, Science **272** (1996) 1782-1785.

[6.4] R. O'Barr, M. Lederman, S. Schultz, W. Xu, A. Scherer, and R.J. Tonucci, *'Preparation and quantitative magnetic studies of single-domain nickel cylinders'*, J. Appl. Phys. **79** (1996) 5303-5305.

[6.5] C. Miramond, C. Fermon, F. Rousseaux, D. Decanini, and F. Carcenac, *'Permalloy cylinderical submicron size dot arrays'*, J. Magn. Magn. Mat. **165** (1997) 500-503.

[6.6] A. Fernandez, M.R. Gibbons, M.A. Wall, and C.J. Cerjan, *'Magnetic domain structure and magnetization reversal in submicron-scale Co dots'*, J. Magn. Magn. Mat. **190** (1998) 71-80.

[6.7] C.A. Ross, T.A. Savas, H.I. Smith, M. Hwang, and R. Chantrell, *'Modelling of hysteresis loops of arrays of 100 nm period nanomagnets'*, IEEE Trans. Magn. in press.

[6.8] M.A.M. Haast, J.R. Schuurhuis, L. Abelmann, J.C. Lodder, and Th.J.A. Popma, *'Reversal mechanism of submicron patterned CoNi/Pt multilayer dots'*, IEEE Trans. Magn. **34** (1998) 1006-1008.

[6.9] M.A.M. Haast, I.R. Heskamp, L. Abelmann, J.C. Lodder, and Th.J.A. Popma, *'Magnetic characterization of large area arrays of single and multi domain CoNi/Pt multilayer dots'*, J. Magn. Magn. Mat. **193** (1999) 511-514.

[6.10] W. Wu, B. Cui, X.Y. Sun, W. Zhang, L. Zhuang, L. Kong, and S.Y. Chou, *'Large area high density quantized magnetic disks fabricated using nanoimprint lithography'*, J. Vac. Sci. Technol. B **16** (1998) 3825-3829.

[6.11] S. Sun, and C.B. Murray, *'Synthesis of monodisperse cobalt nanocrystals and their assembly into magnetic superlattices (invited)'*, J. Appl. Phys. **85** (1999) 4325-4330.

[6.12] C. Haginoya, S. Heike, M. Ishibashi, K. Nakamura, K. Koike, T. Yoshimura, J. Yamamoto, and Y. Hirayama, *'Magnetic nanoparticle array with perpendicular crystal magnetic anisotropy'*, J. Appl. Phys. **85** (1999) 8327-8331.

Summary

This thesis describes the results of a research project in the field of high bit-density data-storage media. More specifically, the material aspects of the novel recording technique using patterned media have been studied. The aim of the work was the design, realization and characterization of such a patterned medium.
Chapter 1 provides a general introduction to the field of data storage. The incredible progress in bit density of today's data storage devices is highlighted. Moreover, an outlook to future developments is given. It is shown that patterned media, due to their discrete and single domain nature, have superior recording properties and allow much higher bit densities than conventional hard disk media.
In Chapter 2 the material requirements for a prototype patterned medium are given. A proper patterned medium should consist of magnetic dots which have a strong intergranular exchange coupling, large uniaxial magnetic anisotropy and low switching field distribution. Using these guidelines several candidate materials are proposed: bariumferrite, Co or Fe based alloys with $L1_0$ phase, amorphous rare earth – transition metal alloys and Co based multilayers. All four materials have a large intrinsic uniaxial magnetic anisotropy, which guarantees a sufficiently large switching field and a long-term thermal stability. Moreover, the dots of the patterned medium can be shaped in such a way that magnetostatic interactions are suppressed. In this respect, single-element Co, Ni or Fe patterned media are disadvantageous because they suffer from too large magnetostatic interactions in a densely packed 2D dot-array and therefore will limit the ultimate bit density. With respect to the amorphous alloys some caution is required, because the origin of their magnetic anisotropy is not undisputed. In addition to these qualitative considerations, the single- to two-domain transition and the switching field of $Co_{50}Ni_{50}$/Pt multilayer dots have been predicted by analytical and micromagnetic calculations: $d_{crit} \approx 70$ nm and $H_{sw} \geq 500$ kA/m. However, it is also shown that the latter is strongly dependent on dot shape and can be considerably smaller.
In Chapter 3 the patterning technology for our studies on submicron patterned magnetic thin films is motivated and discussed. A review of existing submicron patterning technologies shows that laser interference lithography uniquely combines simplicity, large areas and sub 100 nm dimensions. With the present process sub-100 nm resist structures at a period of 200 nm can be prepared. However, at these dimensions the process latitude is limited. With a higher contrast resist in combination with an antireflective coating considerable improvement is achieved. Although further progress may be limited by instabilities of the present exposure setup, lasers with smaller wavelength and improved (substrate) stability allows the succesfull patterning of dot sizes smaller than 50 nm with our technique.
In Chapter 4 an extensive study into the relation between deposition conditions, microstructure and magnetic anisotropy of sputtered $Co_{50}Ni_{50}$/Pt multilayers is presented. The degree of texture, as determined with X-Ray Diffraction, appeared to be strongly dependent on the total layer geometry and deposition pressure. At

low deposition pressure the multilayers have a low atomic roughness and a strong preferred (111) texture, while at high deposition pressure the multilayers have a large atomic roughness and an additional (200) texture is present. Moreover, if deposited without underlayer, the first several nm's of the multilayer stack have a lack of texturing, even at low deposition pressure.

The magnetic anisotropy consists of interface, shape and magneto-elastic anisotropy. The magneto-elastic anisotropy contributes to the perpendicular direction, but is only 10-20% of the shape anisotropy. Therefore, interface anisotropy is the most significant contribution to the effective perpendicular magnetic anisotropy. Thin multilayers have a lower average interface anisotropy because of the 'initial layer effects'. Besides, due to an increase in interfacial mixing by high-energy bombardment, the interface anistropy decreases towards lower deposition pressure. On the other hand, due to the increase of atomic roughness, the effective area and herewith the effective interface anisotropy decreases towards higher deposition pressure. Therefore, in order to optimize perpendicular magnetic anisotropy, the multilayers should be as thick as possible and be deposited at an intermediate pressure.

Finally, based on these results and the constraints of the patterning process, the deposition conditions of the $Co_{50}Ni_{50}$/Pt multilayers for the research on patterned media were selected. This multilayer has 26 bilayers of $Co_{50}Ni_{50}$ (6 Å) / Pt (6 Å) and is deposited at 12 μbar. It has a large perpendicular magnetic anisotropy ($H_{K,eff}$ = $(4.7\pm0.2)\cdot10^2$ kA/m) and a strong intergranular exchange coupling. Therefore, the basic requirements for a patterned storage medium have been fullfilled.

In Chapter 5 the magnetization reversal in submicron and micron-sized $Co_{50}Ni_{50}$/Pt multilayer dots is described. It was checked that the patterning process (deposition-resist spinning and patterning-ion beam etching) does not deteriorate the magnetic properties of the multilayers. Instead, an improvement of the perpendicular magnetic anisotropy was found.

The magnetization reversal of $Co_{50}Ni_{50}$/Pt multilayer dots is strongly dependent on dot size (i.e. diameter). In fact, over the studied range of sizes, i.e. 60 nm – 215 μm, three main types of reversal can be distinguished. For dots larger than 20 μm the reversal is dominated by small structural defects in the as deposited multilayer. These dots have a broad nucleation field distribution and domains are formed during reversal. Dots with a size between 140 nm and 20 μm are actually multi domain as well, but no domains are formed during the perpendicular (easy-axis) reversal. Finally, dots smaller than 140 nm can not be demagnetized and appear as single domain dots. Their mode of reversal is incoherent rotation.

The most important conclusion of Chapter 5 is that with the preparation of 70 nm $Co_{50}Ni_{50}$/Pt multilayer dots over a large area (order of cm^2 and 200 nm center-to-center spacing) a prototype of patterned storage medium has been realized. This 16 $Gbit/in^2$ medium consists of truly single domain dots with large uniaxial magnetic anisotropy. The thermal stability is not sufficient for long-term stability, but by an optimization of the patterning process this can be enormously improved without the need for another material. Due to the lack of magnetostatic interactions

between dots and the presence of a strong intrinsic perpendicular magnetic anisotropy, this patterned medium has superior storage properties compared to single-element (Co or Ni) patterned media reported in literature so far.
In Chapter 6 the experimental values of properties such as critical dot diameter and switching field, as presented in Chapter 5, are compared with the (theoretical) predictions made in Chapter 2. In particular, the switching field seems to be extremely sensitive to effects of shape, etching damage and/or quality of layer growth. This leads to a switching field distribution, which is hard to control. More in general, Chapter 6 shows that in this relatively new field of research many challenges are still present. This applies both for the development of the application of magnetic dots as patterned media and for the improvement of present models of the magnetization reversal of single domain particles.

Samenvatting

Dit proefschrift beschrijft de resultaten van een onderzoeksproject in het vakgebied van hoge bitdichtheid data-opslag media. Meer in het bijzonder, de materiaal aspecten van een nieuwe registratie techniek op basis van gestructureerde media is bestudeerd. Het doel van het werk was het ontwerp, de realisatie en karakterisering van zo'n gestructureerd medium.

Hoofdstuk 1 geeft een algemene inleiding tot het vakgebied van data opslag. De ongelooflijke vooruitgang in bitdichtheid van hedendaagse data opslag systemen wordt toegelicht. Verder wordt een vooruitblik op toekomstige ontwikkelingen gegeven. Er wordt beschreven dat gestructureerde media, vanwege de geïsoleerde bits die bovendien 1-domein zijn, superieure registratie eigenschappen hebben en veel hogere bitdichtheden mogelijk maken dan conventionele harde schijf media.

In hoofdstuk 2 worden de materiaal eisen voor een prototype gestructureerd medium gegeven. Een gestructureerd medium moet bestaan uit magnetische pilaren die een sterke intergranulaire wisselwerking, hoge uniäxiale magnetische anisotropie en een lage omkeerveld-verdeling hebben. Aan de hand van deze richtlijnen worden enkele kandidaat materialen voorgesteld: bariumferriet, op Co of Fe gebaseerde legeringen met $L1_0$ fase, amorfe zeldzame aard – transitie metaal legeringen en op Co gebaseerde multilagen. Al deze vier materialen hebben een hoge intrinsieke magnetische anisotropie, die een voldoende hoog omkeerveld en een thermische stabiliteit over een lange termijn garanderen. Verder kunnen de eenheden van een gestructureerd medium op een dusdanige manier gevormd worden dat magnetostatische interacties onderdrukt worden. In dit opzicht zijn gestructureerde media van zuiver Co, Ni of Fe nadelig omdat zij last hebben van te grote magnetostatische interacties in een dichtgepakte tweedimensionale rij van pilaren en daarom de uiterst bereikbare bitdichtheid beperken. Met betrekking tot amorfe legeringen enige voorzichtigheid is vereist, omdat de oorsprong van hun magnetische ainsotropie niet onbetwist is. In aanvulling op deze kwalitatieve overwegingen is de 1-domein tot 2-domein overgang en het omkeerveld van $Co_{50}Ni_{50}$/Pt multilaag pilaren voorspeld door middel van analytische en micromagnetische berekeningen: $d_{crit} \approx 70$ nm en $H_{sw} \geq 500$ kA/m. Echter, er wordt ook aangetoond dat de laatste sterk afhankelijk van de pilaar vorm is en aanzienlijk kleiner kan zijn.

In hoofdstuk 3 wordt de structurering technologie voor onze studies over submicron gestructureerde magnetische dunne lagen gemotiveerd en bediscussieerd. Uit een overzicht van bestaande submicron structurering technieken blijkt dat laser interferentie lithografie uniek eenvoudigheid, grote oppervlakken en sub-100 nm afmetingen combineert. Met het huidige procédé worden sub-100 nm fotolak structuren met een periode van 200 nm gemaakt. Echter, bij deze afmetingen is de marge van het procédé beperkt. Met hogere contrast fotolakken in combinatie met een antireflectie laag wordt een aanzienlijke verbetering bewerkstelligd. Hoewel verdere vooruitgang beperkt kan worden door

instabiliteiten van de huidige belichtingsopstelling, maken lasers met een kleinere golflengte en een verbeterde (substraat) stabiliteit de succesvolle structurering van een pilaar grootte kleiner dan 50 nm mogelijk met onze techniek.
In hoofdstuk 4 wordt een uitgebreide studie naar de relatie tussen depositie omstandigheden, microstructuur en magnetische anisotropie van gesputterde $Co_{50}Ni_{50}$/Pt multilagen gepresenteerd. De mate van textuur, zoals bepaald met X-Ray Diffractie, blijkt sterk afhankelijk te zijn van de totale laag geometrie en depositie druk. Bij lage depositie druk hebben de multilagen een lage atomaire ruwheid en een sterke voorkeur voor de (111) textuur, terwijl bij hoge depositie druk de multilagen een hoge atomaire ruwheid hebben en een bijkomstige (200) textuur aanwezig is. Verder, indien gedeponeerd zonder onderlaag, hebben de eerste nm's van de multilaag stapeling een gebrek aan een duidelijke textuur, zelfs bij lage depositie druk.
De magnetische anisotropie bestaat uit grenslaag, vorm en magneto-elastische anisotropie. De magneto-elastische anisotropie draagt bij aan de loodrechte richting, maar is slechts 10-20% van de vorm anisotropie. Daarom, is de grenslaag anisotropie de meest belangrijke bijdrage aan de effectieve loodrechte magnetische anisotropie. Dunne multilagen hebben een lagere gemiddelde grenslaag anisotropie vanwege de 'initiële laag effecten'. Bovendien, door een toename van menging in de grenslaag ten gevolge van hoge-energie bombardement, neemt de grenslaag anisotropie af bij lagere depositie drukken. Aan de andere kant, ten gevolge van een toename van atomaire ruwheid, neemt het effectieve oppervlak en hiermede de effectieve grenslaag anisotropie af bij hogere depositie drukken. Daarom, voor een optimalisatie van de loodrechte magnetische anisotropie, zouden de multilagen zo dik als mogelijk moeten zijn en worden gedeponeerd bij een tussenliggende druk.
Tenslotte, gebaseerd op deze resultaten en de beperkingen van het structuring procédé, zijn de depositie omstandigheden van de $Co_{50}Ni_{50}$/Pt multilagen voor het onderzoek naar gestructureerde media geselecteerd. Deze multilaag heeft 26 dubbellagen van $Co_{50}Ni_{50}$ (6 Å) / Pt (6 Å) en wordt gedeponeerd bij 12 μbar. Hij heeft een hoge loodrechte magnetische anisotropie ($H_{K,eff} = (4.7\pm0.2)\cdot10^2$ kA/m) en een sterke intergranulaire wisselwerking. Daarom wordt aan de principiële eisen voor een gestructureerd opslag medium voldaan.
In hoofdstuk 5 wordt het magnetisatie omkeergedrag in submicron en micron $Co_{50}Ni_{50}$/Pt multilaag pilaren beschreven. Er is gecontroleerd of het structurering procédé (depositie-fotolak aanbrengen en structureren-ionenbundel etsen) verslechtert niet de magnetische eigenschappen van de multilagen. Integendeel, een verbetering van de loodrechte magnetische anisotropie is gevonden.
Het magnetisatie omkeergedrag van $Co_{50}Ni_{50}$/Pt multilaag pilaren is sterk afhankelijk van de pilaar grootte (lees: diameter). In feite kunnen over het bestudeerde bereik van grootten, i.e. 60 nm – 215 μm, drie typen van omkeergedrag onderscheiden worden. Voor pilaren groter dan 20 μm wordt het omkeergedrag gedomineerd door kleine oneffenheden in de multilaag zoals deze gedeponeerd is. Deze pilaren hebben een brede nucleatie veld verdeling en tijdens het omkeren van de magnetisatie worden domeinen gevormd. Pilaren met een

grootte tussen 140 nm en 20 μm zijn eigenlijk ook multi-domein, maar tijdens de loodrechte (langs de gemakkelijke as) omkering worden geen domeinen gevormd. Tenslotte, pilaren kleiner dan 140 nm kunnen niet gedemagnetiseerd worden en lijken 1-domein pilaren te zijn. De omkering vindt plaats door incoherente rotatie.
De meest belangrijke conclusie van hoofdstuk 5 is dat met de bereiding van 70 nm $Co_{50}Ni_{50}$/Pt multilaag pilaren over een groot oppervlak (orde van cm^2 en 200 nm hart-tot-hart afstand) een prototype van een gestructureerd opslag medium is gerealiseerd. Dit 16 Gbit/in^2 medium bestaat uit echte 1-domein pilaren met een hoge uniäxiale magnetische anisotropie. De thermische stabiliteit is niet voldoende voor stabiliteit over een lange termijn maar door het optimaliseren van het structurering procédé kan dit enorm verbeterd worden zonder de behoefte aan een ander materiaal. Door het ontbreken van magnetostatische interacties tussen de pilaren en de aanwezigheid van een sterke intrinsieke loodrechte magnetische anisotropie, heeft dit gestructureerd medium superieure opslag eigenschappen vergeleken met enkele-element (Co of Ni) gestructureerde media gerapporteerd in de literatuur tot op heden.
In hoofdstuk 6 worden de experimentele waarden van eigenschappen zoals kritische pilaar diameter en omkeerveld, zoals gepresenteerd in hoofdstuk 5, vergeleken met de (theoretische) voorspellingen gemaakt in hoofdstuk 2. In het bijzonder, het omkeerveld lijkt extreem gevoelig voor effecten van vorm, ets schade en/of kwaliteit van de laag groei. Dit leidt tot een omkeerveld verdeling die moeilijk te controleren is. Meer in het algemeen, hoofdstuk 6 maakt duidelijk dat in dit relatief nieuwe onderzoeksgebied nog veel uitdagingen aanwezig zijn. Dit geldt zowel voor de ontwikkeling van de toepassing als gestructureerde media als voor de verbetering van de huidige modellen van het magnetisatie omkeergedrag van 1-domein deeltjes.

Acknowledgements

I had the pleasure to do my Ph.D. project in a true multidisciplinary environment with many people contributing to my research. Here I would like to express my thanks to them:

Prof.dr. Th.J.A. Popma for being my promoter.

Cock Lodder for his daily supervision, our many discussions and his successful efforts to create perfect boundary conditions for my research.

The members of the committee for valuable comments and suggestions on my thesis.

The users committee of STW project ‘Magneto-optical multilayer structures’ for the annual discussions.

Iwan Heskamp for the input of his cleanroom and Labview skills.

Takehito Shimatsu for teaching me part of his vast knowledge of magnetic material science and technology.

Leon Abelmann for our many discussions about the work related to patterned media.

Ron Schuurhuis, Bas Sotthewes and Arnout van den Bos for their contributions to the work related to patterned media.

The Light Waveguide Device group for sharing their Laser Interference Lithography technology with us. In particular, I would like to acknowledge Gert Veldhuis for introducing us to the technology and Henk van Wolferen for later technical assistance.

Poul de Haan, Thijs Bolhuis and Martin Siekman for all kind of assistance in the ISTG lab.

The MESA+ staff, in particular Johnny Sanderink, Bert Otter and Mark Smithers for their numerous SEM work.

Andrei Kirilyuk from the University of Nijmegen for our collaboration on the characterization of CoNi/Pt interfaces.

Prof. J. Ferré from the University of Paris-Sud, Orsay, France for his hospitality to do some experiments on his advanced polar Kerr microscope.

Steffen Porthun for making a beautiful MFM image.

Klaus Ramstöck for making his micromagnetic simulation package available for modeling of dots and his efforts for improving its flexibility; I also would like to acknowledge Sindhu Kumar for taking part in the simulations itself.

Martin Bijker for his ideas which initiated the work on CoNi/Pt multilayers.

Abdellah Lisfi for several, mostly extensive, fundamental discussions concerning magnetic characterization.

Karin Verbist from the University of Antwerpen, Belgium for HRTEM images.

The technical teams in the ELTN workshops.

All, not explicitly mentioned, (former) group members who made my work at the Information Storage Technology Group pleasant and fruitfull.

Ajuus / Houdoe!

Marc

About the author

The author was born on August 12, 1971 in Rijsbergen. In 1989 he graduated from the Mencia de Mendoza Lyceum in Breda (‘ongedeeld VWO’) and started the study Applied Physics at the Eindhoven University of Technology. In the framework of this study a three-month practical training at the group of Prof. R. d’Agostinho of the University of Bari, Italy was carried out on the subject of low-temperature PECVD of siliconnitride. Moreover, the author was during his study assistant at the practicum ‘physical transport phenomena’. In 1995 he graduated in the group of Prof. M. de Voigt, where he worked on an in-situ nuclear measurement system for chemical reactions on catalysts. Subsequently he started a Ph.D. project in the Information Storage Technology Group at the MESA Research Institute, which is concluded with this thesis.

List of publications

Scientific journals

'Nanofabricage van een discreet medium voor magnetische recording met zeer hoge bitdichtheid'
J.R. Schuurhuis, M.A.M. Haast, L. Abelmann, G.J. Veldhuis and J.C. Lodder
NEVAC Blad **35** (3) (1997) 55-63.

'Submicron patterned CoNi/Pt multilayers for ultra high density recording'
M.A.M. Haast, I.R. Heskamp, L. Abelmann, G.J. Veldhuis, J.C. Lodder and Th.J.A. Popma
Proceedings of the CMO conference 1997 (1997) 51-53.

'Magnetic and magneto-optic effects in Barium Ferrite films grown by pulsed laser deposition'
A. Lisfi, J.C. Lodder, P. de Haan, M.A.M. Haast and F.J.G. Roesthuis
Proceedings of the Magneto-Optical Recording International Symposium 97, Journal of the Magnetic Society Japan **22** (S2) (1998) 159-162.

'Probing structure and magnetism of CoNi – Pt interfaces by non-linear magneto-optics'
A. Kirilyuk, Th. Rasing, M.A.M. Haast and J.C. Lodder
Applied Physics Letters **72** (18) (1998) 2331-2333.

'Reversal mechanism of submicron patterned CoNi/Pt multilayer dots'
M.A.M. Haast, J.R. Schuurhuis, L. Abelmann, J.C. Lodder and Th.J.A. Popma
IEEE Transactions on Magnetics **34** (4) (1998) 1006-1008.

'Comparing the resolution of magnetic force microscopes using the CAMST reference sample'
L. Abelmann, S. Porthun, M. Haast, C. Lodder, A. Moser, M.E. Best, P.J.A. van Schendel, B. Stiefel, H.J. Hug, G.P. Heydon, A. Farley, S.R. Hoon, T. Pfaffelhuber, R. Proksch and K. Babcock
Journal of Magnetism and Magnetic Materials **190** (1998) 135-147.

'Homogeneity and stability issues in patterned media for discrete magnetic recording'
M.A.M. Haast, I.R. Heskamp, L. Abelmann, J.C. Lodder and Th.J.A. Popma
Proceedings of the CMO conference 1998 (1998) 68-73.

'Magnetic characterization of large area arrays of single and multi domain CoNi/Pt multilayer dots'
M.A.M. Haast, I.R. Heskamp, L. Abelmann, J.C. Lodder and Th.J.A. Popma
Journal of Magnetism and Magnetic Materials **193** (1999) 511-514.

International Conferences (first author only)

'Magnetic anisotropy and microstructure of CoNi/Pt multilayers'
M.A.M. Haast, T. Shimatsu, J.C. Lodder and Th.J.A. Popma
NATO Advanced Study Institute 'Frontiers in magnetism at reduced dimensions' (poster)
Crimea, Ukraine, May 25 – June 3 1997.

'Submicron patterned CoNi/Pt multilayers'
M.A.M. Haast, J.R. Schuurhuis, L. Abelmann, G.J. Veldhuis, J.C. Lodder and Th.J.A. Popma
17th European Conference On Surface Science (oral)
Enschede, The Netherlands, September 16-19 1997.

'Magnetic properties of 60 nm dots prepared with laser interference lithography'
M.A.M. Haast, J.R. Schuurhuis, L. Abelmann, J.C. Lodder and Th.J.A. Popma
7th Joint MMM-Intermag Conference (oral)
San Francisco, USA, January 5-9 1998.

'Magnetic characterization of arrays of submicron CoNi/Pt multilayer dots'
M.A.M. Haast, I.R. Heskamp, L. Abelmann, J.C. Lodder and Th.J.A. Popma
Magnetic Recording Media conference (poster)
Maastricht, The Netherlands, August 31 – September 2 1998.

'Nanoscale patterned magnetic thin films designed for ultra high density magnetic recording'
M.A.M. Haast, I.R. Heskamp, L. Abelmann, J.C. Lodder and Th.J.A. Popma
Micro and Nano Engineering conference (oral)
Leuven, Belgium, September 22-24 1998.

'Nucleation and thermal stability in a CoNi/Pt patterned medium'
M.A.M. Haast, I.R. Heskamp, L. Abelmann, J.C. Lodder and Th.J.A. Popma
Spring meeting of the Materials Research Society (oral)
San Francisco, USA, April 5-9 1999.